Search for the Cabibbo-Supressed D^+ Meson Decays $D^+ \rightarrow \pi^+\pi^0$ and $D^+ \rightarrow K^+\pi^0$

DISSERTATION

Presented in Partial Fulfillment of the Requirements for

the Degree Doctor of Philosophy in the

Graduate School of The Ohio State University

By

Dirk Hufnagel

* * * * *

The Ohio State University

2005

Dissertation Committee:

Klaus Honscheid, Adviser

Richard Kass

Stephen Pinsky

Thomas Humanic

Approved by

Adviser

Graduate Program in Physics

ABSTRACT

As a graduate student at The Ohio State University I was in the unusual position to contribute to all aspects of a modern particle physics collider experiment. Following an introduction to the Standard Model of Particle Physics I will describe the detector and Data Acquisition system of the CLEO3 experiment, which I worked on as a graduate student. After that I will switch experiments and describe the BaBar Monte Carlo simulation system, which I have been heavily involved with over the last few years. The last part of the document will present a data analysis using 124.3 fb^{-1} of data from the BaBar detector. The analysis is a measurement of the branching fractions for the singly Cabibbo-suppressed decay mode BF($D^+ \rightarrow \pi^+\pi^0$) $= (1.21 \pm 0.10(stat.) \pm 0.08(sys.) \pm 0.08(pdg)) \times 10^{-3}$ and for the doubly Cabibbo-suppressed decay mode BF($D^+ \rightarrow K^+\pi^0$)$= (2.11 \pm 0.43(stat.) \pm 0.15(sys.) \pm 0.16(pdg)) \times 10^{-4}$, where the first error is statistical, the second is systematic and the last is due to the D absolute branching fraction scale.

ACKNOWLEDGMENTS

First and foremost I want to thank my family, especially my parents, for their support and encouragement. I am sure they were beginning to doubt that I would ever reach the finish line. I especially want to thank my mother for the care packages she sent me. All the different kinds of chocolate were highly appreciated by me and my colleagues here at Ohio State. I am sure these care package will be most sorely missed once I leave.

There are so many others to thank for, most importantly my adviser Klaus Honscheid. I am very grateful for all the opportunities he gave me to work on interesting and challenging projects, be it the CLEO3 DAQ system or the BaBar MC production. In hindsight he probably wishes that I had found this work a little less interesting and had concentrated more on finishing my dissertation.

I want to thank my teachers from the math club who awakened my interest in math and science at an early age. I also want to thank my teachers at the Carl-Friedrich-Gauss-Gymnasium who deepened that interest. I especially want to thank my Physics teacher, Dr. Weiss-Motz, who with his unique teaching style and enthusiasm lured me away from the abstractness and dryness of mathematics and introduced me to the wonders of experimental physics.

Professor Schubert and Professor Spaan introduced me to particle physics during my time at the Technical University in Dresden and also helped me to get into contact with my current adviser, which lead to my coming to Ohio State. They set me on the path to what I am doing today.

There are numerous people at OSU who helped me with physics or computing questions or simply made my time here more enjoyable. Richard Kass was always willing to discuss some physics or statistics problem. I learned a lot from Andreas Wolf and Hubert Schwarthoff about C++ programming and we had many interesting discussions about computing problems both at OSU and later at Cornell. Being in the same office with my fellow graduate students Chul Gwon, Eric Eckhart and Terry Hart was always fun. Chul, Eric and Terry have since moved on to greener pastures, but new graduate students joined the group. Don Burdette, James Morris and Joseph Regensburger are always willing to engage in discussions on just about any topic.

I also want to thank all the people at Cornell that made the two years I spent there for the commissioning of the CLEO3 detector a blast. I already mentioned Andreas Wolf and Hubert Schwarthoff, additional thanks go to my office mates Tim Wilksen, Todd Pedlar and Jana Thayer.

After our group joined BaBar I got involved in the BaBar Monte Carlo production system and I want to thank everyone that helped me with this, but especially Concezio Bozzi, Stephen Gowdy and Frederic Blanc.

Last but not least I want to than everyone that helped get this data analysis done, especially Thomas Allmendinger. Without him this wouldn't have been possible.

VITA

August 13, 1974 .... Born - Prenzlau, Germany

September 1989-June 1993 .. Spezialschule “C.F.Gauss”, Frankfurt/O., Germany

October 1994-June 1997 ..... Technische Universitaet Dresden, Germany

September 1997 - .... The Ohio State University, Columbus, OH

FIELD OF STUDY

Major Field: Physics

Studies in Experimental Particle Physics: Professor Klaus Honscheid

TABLE OF CONTENTS

LIST OF TABLES

LIST OF FIGURES

CHAPTER 1

Standard Model

1.1 Introduction to Elementary Particle Physics

One of the most fundamental questions one can ask is “What is matter made of ?” The commonly accepted answer from science to that question has changed over time. While the philosophical concept of atoms has been around since the old Greeks (atomos is Greek for indivisible), the modern theory of atoms as the building blocks of matter isn't quite that old. The theory was worked out during the 19th century and at the end of it, atoms were indeed thought of as tiny, indivisible particles all matter is made of.

At the turn of the 20th century new experiments proved this view to be, if not completely incorrect, at least incomplete. The world is indeed made up from atoms, but these atoms are not indivisible particles. The discovery of electrons and their interpretation as smaller parts of an atom by Thomson in 1897 and Rutherford's scattering experiment in 1909 established the modern concept of an atom as a small positively charged core surrounded by negatively charged electrons.

Somewhere in that time frame one has to put the birth of elementary particle physics. Elementary particle physics tries to answer the question I asked in the first sentence “What is matter made of ?” at the smallest scale. It involves the study of subatomic particles (smaller than atom), their properties and interactions.

1.2 Introduction to Standard Model

In the early 60s, the known subatomic particles were split into two categories. On one hand were the leptons, the electron and the muon and their corresponding anti-particles and neutrinos. On the other hand were the hadrons, divided into two general categories, baryons like protons or neutrons and mesons like pions and kaons. But beyond this distinction between baryons and mesons, there was no underlying classification scheme that explained the structure of all known hadrons. The situation was very similar to what had happened about a century earlier in chemistry before the introduction of the Periodic Table, when lots of elements had been identified but the underlying structure was unknown.

In 1964, in an attempt to bring order to this zoo of elementary particles, Gell-Man and Zweig independently proposed the quark model. According to this model, hadrons themselves are not elementary particles, but made up from smaller constituents called quarks. The original quark model contained only three quarks, the up quark, the down quark and the strange quark and the corresponding anti-quarks.

It wasn’t until the discovery of another quark called charm in 1974 [1] that the quark model became universally accepted. The fifth quark, called bottom, was discovered in 1977 [2] and the long predicted sixth quark, the top quark, was finally detected at Fermilab in 1995 [3].

The Standard Model of Particle Physics describes these fundamental particles, quarks and leptons, their properties and interactions.

1.3 Fundamental Particles and Forces

I already mentioned the fundamental particles, the quarks and leptons, in the last section. Both quarks and leptons can be divided into three families, with two particles in each family. Table 1.1 shows the three families of leptons. Each family contains a charged lepton (electron, muon or tau) and a neutral lepton (electron, muon or tau neutrino).

Family	Flavor	Mass (MeV/c^2)	Electric Charge	Weak Isospin
I	ν_e	$< 3 \times 10^{-6}$	0	$+1/2$
	e	0.51	-1	$-1/2$
II	ν_μ	< 0.19	0	$+1/2$
	μ	105.66	-1	$-1/2$
III	ν_τ	< 18.2	0	$+1/2$
	τ	$1776.99^{+0.29}_{-0.26}$	-1	$-1/2$

Table 1.1: Properties of leptons [6]. Upper limits on mass given for all neutrinos. Error on mass of e and μ accurate past 5 significant figures.

Table 1.2 shows the three families of quarks. Each family contains one quark with an electric charge of $+2/3$ and another quark with an electric charge of $-1/3$.

All interactions between these fundamental particles can be described in terms of four fundamental forces: gravity, electromagnetic, weak and strong forces. Gravity and electromagnetism are long range forces and observable in the macroscopic world, weak and strong forces have a very short range. Table 1.3 lists the four fundamental forces and their properties.

The Standard Model of Particle Physics only includes three of the four fundamental forces. Although we have a good theoretical understanding of gravity

Family	Flavor	Mass (GeV)	Electric Charge	Weak Isospin
I	*u*p	$0.0015 - 0.0045$	$+2/3$	$+1/3$
	*d*own	$0.004 - 0.008$	$-1/3$	$-1/2$
II	*c*harm	$1.15 - 1.35$	$+2/3$	$+1/3$
	*s*trange	$0.080 - 0.130$	$-1/3$	$-1/2$
III	*t*op	174.3 ± 5.1	$+2/3$	$+1/3$
	*b*ottom	$4.1 - 4.4$	$-1/3$	$-1/2$

Table 1.2: Properties of quarks [6]. Mass ranges given for all quarks except t.

Force	Strong	Electromagnetic	Weak	Gravity
Gauge Boson	gluons (g)	photon (γ)	$W^{\pm}$, Z^0	graviton
Charge	color	electric	weak isospin	mass
Strength*	10	10^{-2}	10^{-13}	10^{-41}
Mass (GeV)	0	0	80.42, 91.19	0
Spin	1	1	1	2
Range (m)	$< 10^{-15}$	∞	$10^{-18} \sim \frac{\hbar}{M_W c}$	∞

Table 1.3: The Fundamental Forces. *Note that the strength of the forces could differ depending on the physical properties of the particles as well as their relative distances. The values here are rough estimates [5].

on macroscopic scales, nobody has yet managed to give a satisfactory theoretical explanation of gravity on subatomic scales ("Quantum Gravity").

According to the Standard Model, the fundamental particles interact through the exchange of force-carrying gauge bosons. Bosons are particle with integer spins. In contrast to this there are the fermions with half-integer spins. Quarks and leptons are both fermions with spin 1/2. The gauge bosons for all four fundamental forces are also listed in Table 1.3. They all have spin 1, except for the graviton, which is the proposed, but not yet detected, gauge boson for gravity.

1.3.1 Gravity

As seen in Table 1.3, the strength of the gravitational force is considerable less then the strength of the other forces. Nevertheless, in the macroscopic world gravity is the most visible force. We experience it every day as the Earth's gravity is acting on our bodies. The electromagnetic force has a long range too and is stronger then gravity, but it acts on charge and charge exists as positive and negative charge. Most objects in the macroscopic world are charge neutral, while mass is always accumulative.

At subatomic scales the overall effect of gravity is negligible compared to the other forces. This fact also explains why it is so hard to devise a theory of gravity at very small scales.

1.3.2 Electromagnetic force

The electromagnetic force is acting on electrically charged particles and is propagated by the exchange of photons. The theory describing it is called Quantum Electrodynamics (QED). Figure 1.1 shows the most basic QED process, we call a figure like this a "Feynman diagram". Solid lines represent particles, in this case an electrically charged particle, for instance an electron. The curvy lines represent the gauge bosons, in this case a photon. Each intersection of solid and curvy line is called a "vertex" and for each vertex we can define a "coupling constant" which determines the strength of the interaction. The coupling constant for QED is called the fine-structure constant α.

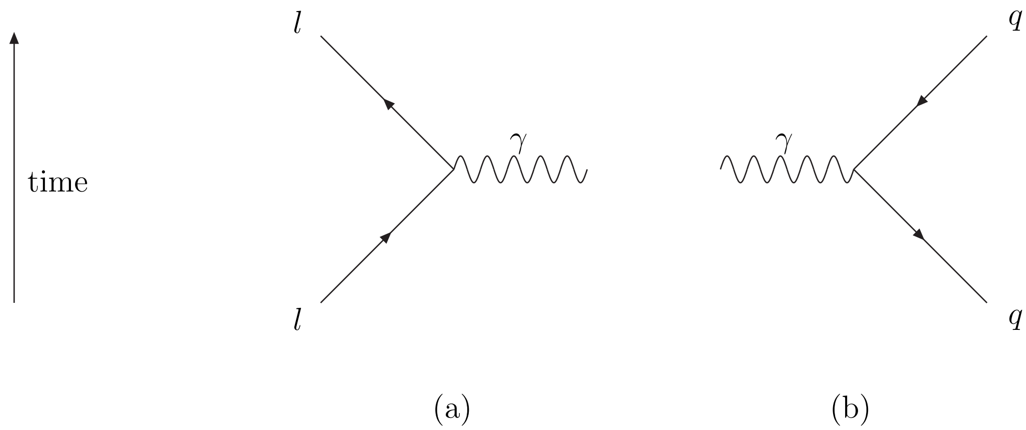

Figure 1.1: Elementary electromagnetic interactions. The diagrams can also be rotated so that the photon travels along the time-axis.

1.3.3 Strong force

The strong force is acting on quarks and is propagated by the exchange of gluons. The strong force couples to a "strong charge" which is called color (has nothing to do with the usual color in the optical sense). The color charge can either be "red", "green" or "blue" (R, G, B). Negative color charges ($\bar{R}$, $\bar{G}$, $\bar{B}$) are also possible. The gluon itself also has color, which makes interactions of gluons with other gluons possible.

In nature we have observed only colorless objects. This also means that isolated quarks have not been observed. The reason for this is that quarks and anti-quarks are confined to bound states. If one tries to separate them, the strong force doesn't drop off with distance. Instead of separating them, we eventually reach the energy threshold for production of quark-antiquark pairs and produce new bound states.

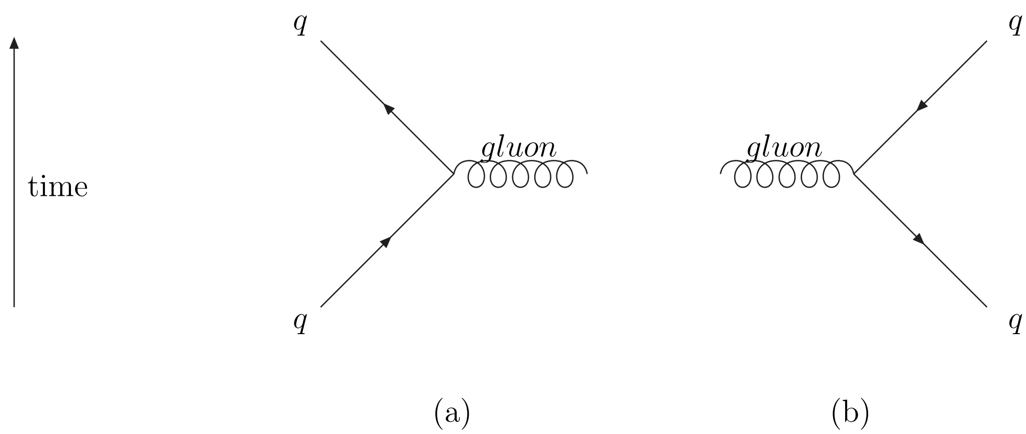

Figure 1.2: Elementary strong interactions. The diagrams can also be rotated so that the gluon travels along the time-axis.

The requirement for a net color charge of zero puts restrictions on what bound states of quarks and anti-quarks are allowed. One possibility is to combine one quark with a positive color charge with an anti-quark of the opposite negative color charge ($R\bar{R}$, $G\bar{G}$ or $B\bar{B}$). Such a bound state of quark and anti-quark is called a meson. Another option is to combine three quarks or anti-quarks with each of the quark or anti-quark having a different color (RGB or $\bar{R}\bar{G}\bar{B}$). A bound state of three quarks is called a baryon.

The theory describing strong interactions is called Quantum Chromodynamics (QCD). Figure 1.2 shows the most basic QCD process.

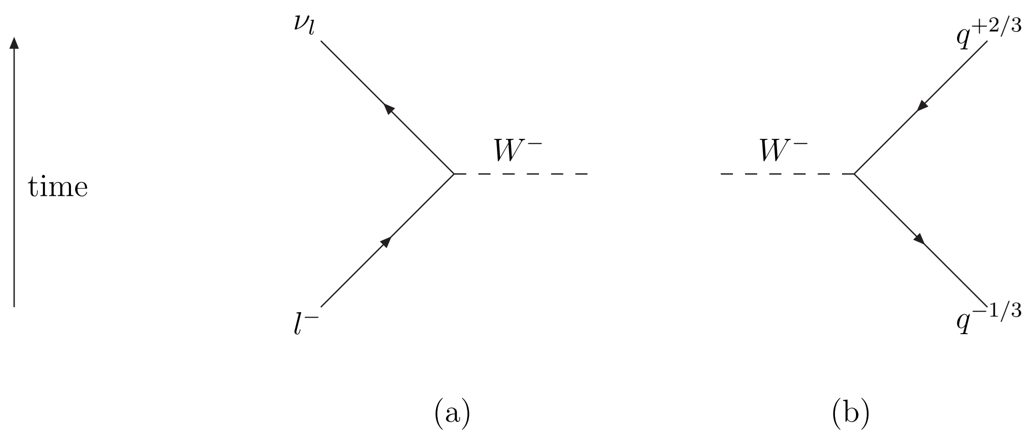

Figure 1.3: Elementary weak interactions. The diagrams can also be rotated so that the W boson travels along the time-axis.

1.3.4 Weak force

The electromagnetic force only acts on electrically charged particles and the strong force only acts on quarks and gluons. The weak force is the only force that acts on all the fundamental particles and is the only force that acts on neutrinos. There are both charged (mediated by $W^{\pm}$) and neutral (mediated by Z^0) weak interactions. The $W^{\pm}$ and Z^0 gauge bosons can also interact with each other and the $W^{\pm}$ also couple to photons (since they have an electric charge).

Another major difference between strong and electromagnetic interactions on one side and weak interactions on the other side is that only weak interaction can change a particle of one type into a particle of another type. Examples would be a transitions from a u quark to a d quark or from an electron to an electron neutrino.

Figure 1.3 shows two diagrams in which transitions from one particle type to another occur. In diagram (a) a charged lepton is changed into a neutrino. In diagram (b) the type of quark (the *flavor*) changes in the interaction.

1.4 CKM Matrix

Coming back to Figure 1.3, an interesting difference between interactions of type (a) and (b) is that in (a) the charged lepton and the neutrino have to be in the same lepton family, while in (b) the two quarks can be in different families.

The general idea to explain why the weak interaction can change the quark flavor between families is to assume that the weak force doesn't couple to the normal quark mass eigenstates

$$\begin{pmatrix} u \\ d \end{pmatrix} \begin{pmatrix} c \\ s \end{pmatrix} \begin{pmatrix} t \\ b \end{pmatrix} \tag{1.1}$$

but instead couples to different weak eigenstates

$$\begin{pmatrix} u \\ d' \end{pmatrix} \begin{pmatrix} c \\ s' \end{pmatrix} \begin{pmatrix} t \\ b' \end{pmatrix} \tag{1.2}$$

with *d'*, *s'* and *b'* as linear combinations of d, s and b. The transformation equations between the *d'*, *s'* and *b'* and the physical d, s and b quarks can be written in a matrix form

$$\begin{pmatrix} d' \\ s' \\ b' \end{pmatrix} = \begin{pmatrix} V_{ud} & V_{us} & V_{ub} \\ V_{cd} & V_{cs} & V_{cb} \\ V_{td} & V_{ts} & V_{tb} \end{pmatrix} \begin{pmatrix} d \\ s \\ b \end{pmatrix} \tag{1.3}$$

This matrix is called Cabibbo-Kobayashi-Maskawa matrix or CKM matrix after Cabibbo who in 1963 first proposed this solution for the ability of weak interaction to change flavor between quark families and Kobayashi and Maskawa who in 1973 extended Cabibbo's theory to three quark generations.

If the CKM matrix would be the unit matrix, then the weak eigenstates would be identical to the mass eigenstates and no flavor change across family boundaries would be possible. From experiments we know that it is not the unit matrix, although it comes pretty close. The 90% confidence limits on the magnitudes of the matrix elements are [6]

$$\begin{pmatrix} 0.9739-0.9751 & 0.221-0.227 & 0.0029-0.0045 \\ 0.221-0.227 & 0.9730-0.9744 & 0.039-0.044 \\ 0.0048-0.014 & 0.037-0.043 & 0.9990-0.9992 \end{pmatrix} \tag{1.4}$$

As you can see, transitions between quarks in one family are favored (diagonal elements), while transitions from one family to another (off-diagonal elements) are suppressed. Particle decays that go through such a quark transition between families are called Cabibbo-suppressed.

CHAPTER 2

Experimental Particle Physics

As I already explained in the previous chapter, particle physics is the study of the properties and interactions of subatomic particles. Almost all of the myriad of possible subatomic particles are unstable with lifetimes from next to nothing to close to 15 minutes for the neutron as the longest lived unstable hadron. Table 2.1 lists the lifetimes of various leptons and hadrons. Of the three charged leptons only the electron is stable and the only stable hadron is the proton. There are searches for proton decays but previous experiments have set lower limits on the lifetime of the proton that are multiple orders of magnitude larger then the age of the universe.

Particle	Lifetime in seconds
μ	2.2×10^{-6}
τ	2.9×10^{-13}
$\pi^{\pm}$	2.6×10^{-8}
ρ	0.4×10^{-23}
n	886

Table 2.1: Lifetimes of various leptons and hadrons [6].

Neutrinos are massless and stable particles in the Standard Model description. But in recent years there has been mounting experimental evidence that show neutrinos to have a non-zero mass. If confirmed, it means that the Standard Model description of neutrinos needs to be expanded. For most experiments not explicitly trying to study neutrinos this uncertainty can safely be ignored since the neutrino interaction cross sections are very small compared to those of other particles.

2.1 Producing subatomic particles

Very soon after the Big Bang, the universe was very "hot" with high energy densities. In that environment, subatomic particles were constantly being produced. One process that produced them was pair production, the spontaneous creation of a particle and it's anti-particle from a high energy photon. Unstable particles produced through this process would decay very quickly, but as long as the universe was hot enough, new pairs would be created. As the universe expanded and cooled, pair production would become impossible, first for the heavier particles until finally the universe had cooled down enough to make even pair production of an e^+e^- pair impossible. The only remaining subatomic particles from that era are stable particles like electrons, protons and neutrinos plus energy in the form of photons.

In the current universe, one can produce unstable subatomic particles in the collisions of other subatomic particles (or any other matter like for instance atomic nuclei). Collisions with high enough kinetic energies can result in interactions that generate all kinds of subatomic particles. The produced unstable particles will either decay directly or through a chain of other unstable particles until only stable particles and maybe some extra energy (photons) are left.

These collisions occur naturally, but we can also produce them in the lab. This leads to two classes of experiments, one where we study naturally occurring collisions and another where we create the collisions ourself.

2.2 Cosmic Ray experiment

Apart from producing high momentum particles in the lab, we can also find them in nature. On Earth these particles loose their energy and momentum quickly since they interact with matter. But out in the vacuum of space they can travel for a very long time. We call these particles cosmic rays. Most cosmic rays are protons, with some atomic nuclei and electrons. The exact origins of cosmic rays are uncertain. They can come from any kind of astrophysical process that can accelerate matter to high momenta. Examples are supernovas and objects that can generate very high electromagnetic field strengths.

Cosmic rays hitting the Earth's atmosphere are basically equivalent to a gigantic particle physics experiment with the Earth as the target. We just have to provide the detector, which leads directly to the main problem with this kind of experiment. The interactions mostly happen in the upper atmosphere, which forces us to either observe them from far away or to move the detector closer to the interactions (balloon, airplane or satellite). Both methods have their limitations. Another problem is that the rates aren't very high compared to what we can achieve with lab experiments.

One of the advantages is that the energy distribution of cosmic rays goes up to energies that are not achievable in the lab with current technology. If one is interested to do experiments at these energy scales, one has no choice but to use cosmic rays.

2.3 Collider experiment

If we want to produce collisions of matter with high kinetic energies, we need an experimental setup to accelerate matter. Since electrons and protons have an electric charge, they can easily be accelerated in an electric field. This gives us electrons or protons with high kinetic energies, now we need to collide them with something. That could be some solid material at rest, in which case we call this a fixed target experiment. Another option is to collide two high-momentum particles with each other, we call this a collider experiment.

At this point I want to describe in short terms the working principles of a collider experiment. I am personally familiar with two collider experiments, CLEO and BaBar. As a graduate student I was able to contribute to both the CLEO and BaBar experiments. I worked directly or indirectly on almost all aspects of a collider experiment. In this section I only want to give a general overview, the rest of this document will follow this outline and give more details in the following chapters.

The activities needed to run a collider experiments can be divided into two general categories, first the collection of data from the experiment and secondly whatever is needed to interpret that data.

2.3.1 Collecting data

At the most basic level, to run a collider experiment we need

- machine to accelerate particles and collide them

- detector to observe particles produced in collisions

I won't say anything here about the particle accelerator. CESR, a machine that accelerates and collides electrons and positrons, is described in detail in Chapter 3.

Detectors, even though they can vary significantly in size, construction and what properties they are designed to measure, all operate on the principle that particles moving through matter interact and change that matter. Every detector has an active detector material, which is supposed to interact with the particles passing through (for instance a gas being ionized by charged particles). The changes in the active detector material caused by these interactions have to be measured and converted into electrical signals. Frontend electronics digitizes these electrical signals and makes them available for readout.

As a graduate student I worked on the commissioning of the CLEO3 detector, which was used to study e^+e^- collisions at CESR. Chapter 3 contains a detailed description of the CLEO3 detector and it's various components and subdetectors.

After the particles passed through the detector, the information about the interactions of the particles with the detector is now available in digital form in the frontend electronics. It has to be readout, which is the job of the Data Acquisition system (DAQ system). In addition to transferring the data from the frontend electronics, processing and storing it, the DAQ system also provides control over both the data readout chain and the detector itself. The CLEO3 Data Acquisition system, which I spent a lot of time writing software code for, is explained in Chapter 4.

2.3.2 Interpreting Data

Once the DAQ system writes complete records of all the information collected by the detector for each collision and the particles produced in the collision to permanent storage, these records (also called events) can be analyzed. At this point the information in the events are of a form that makes using them directly for data analysis, if not impossible, at least extremely difficult and time consuming. For this reason, the data is processed further before it is used in data analyses. During this processing step we use the information about a particles interactions with the detector and try to reconstruct the original particle and it's properties. This processing cycle is called reconstruction.

The reconstruction doesn't modify the original data in the event. It just adds information about particles that could be in the event in the form of lists filled with particle candidates.

These lists are what is used for the data analyses. Lets assume we are interested in the decay of the charmed meson $D^+ \to K^-\pi^+\pi^+$. This decay is not a rare decay, about 9% of all D^+ will decay through this decay channel. This makes it relatively simple to find in the data. For each data event we look at the lists of kaon and pion candidates filled during the reconstruction stage and combine the four-vectors of one K^- and two π^+. The resulting four vector sum is then stored. After applying additional cuts (which I won't go into at this point), we calculate a D^+ candidate mass from every stored four-vector and plot these masses in a histogram, as shown in Figure 2.1.

Since the mass of the D^+ is 1.869 GeV [6], we would expect some kind of peak at this value and indeed, there is a nice Gaussian peak centered at around 1.87 GeV.

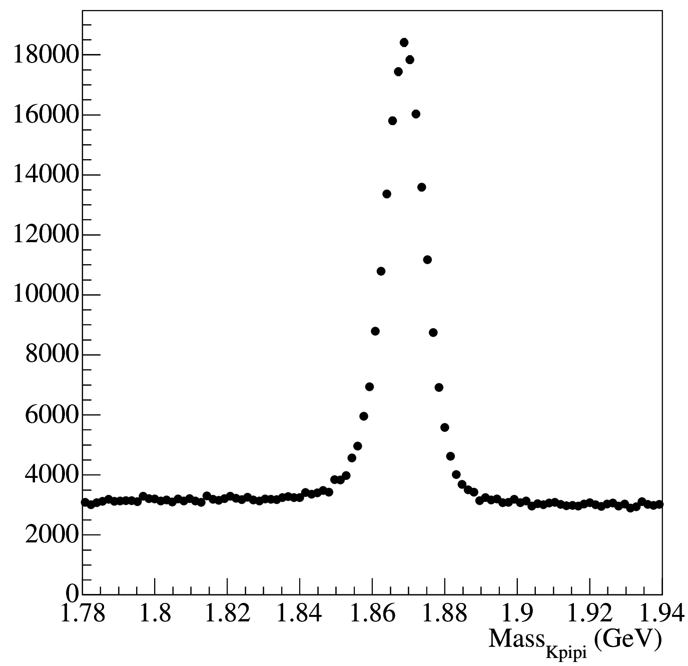

Figure 2.1: Four vector combination of a kaon and two pions

But there also is background, which represents just random $K^-\pi^+\pi^+$ combinations that have nothing to do with a D^+. The purpose behind the cuts I mentioned earlier is to reduce the number of background events. In a perfect world we would apply only cuts that would remove background events and leave all signal events intact. In the real world there is always a trade-off, all cuts will cut out a certain percentage of both background and signal events. We "just" have to find the cuts that remove many more background than signal events.

Often we cannot use data to to find these cuts. It could introduce a bias into the analysis and some decays are so rare that without knowing what to look for we would never see anything in data. Instead of using data to select the best cuts, we can use a simulated data sample. In addition to finding the best cuts, simulated events can also be used to find out how many signal events the cuts will remove. Another reason why simulated events might be needed is that a detector, by design, can never detect all particles produced in the collision. To stay with our $D^+ \to K^-\pi^+\pi^+$ example, some of the K^- or π^+ might leave the detector in a direction where they don't pass through any active detector elements. Some might also interact with other, non active, detector elements. As a result, the detector has a less then 100% efficiency, even before any analysis cuts are applied. We can use simulated events to account for this efficiency loss.

Even though I spent a lot of work on the CLEO3 detector and DAQ system, I did my analysis using BaBar data instead if CLEO data. Our research group left the CLEO collaboration in 2002 and joined the BaBar experiment. At BaBar I worked with the simulation group and also worked on a data analysis. I will say more about the BaBar simulation in Chapter 5 and an analysis based on the BaBar data is presented in Chapters 6 to 10.

2.4 Role of statistics

One thing I should add at this point is that particle physics is driven by statistics. What I mean by that is that given a single unstable subatomic particle, we basically have no way of knowing what it will decay to. Any possible outcome that is not explicitly forbidden (for instance by conservation of energy) can and will occur. We can assign probabilities, the π^0 for instance decays at about 99% to a pair of photons and at about 1% to an electron, a positron and a photon (plus some other very small probability modes like for instance two electrons and two positrons). But for any given π^0 we can't predict which of the decay channels it will decay to. The way we measure these probabilities is to look at a large number of π^0 decays and count how many of them are decays into 2 photons and how many are decays into an electron, a positron and a photon.

This has two consequences. The first is that any measurement we do is limited by the number of events we have available. The smaller the number of events, the larger the statistical error on our measurement. The other consequence is that for a very rare decay channel (with a very low probability of occurring) we need a large number of events to have a chance of observing this decay channel at all.

Apart from the maximum collision energy, which determines what kind of particles can be produced in the collision, another very important consideration for a particle physics experiment is the number of events that can be recorded in a given time. More recorded events mean smaller statistical errors in the measurements.

Since absolute run times cannot be extended forever (funding issues, technology becomes obsolete etc.), we try to maximize the number of recorded events within the overall lifetime of the experiment.

There are a few different options to achieve this, let me mention three basic ones, two technical and one procedural. The first and most obvious is to increase the collision rate, I will say more about this in Chapter 3.

After every collision we have to record the status of the detector. This takes time during which the detector is not available to record any other collision. Minimizing this time, called dead time, is critical for a high event rate.

These first two options are not independent of each other. The dead time is a function of the design of the detector readout electronics and is pretty much fixed. That means as one increases the rate of collisions, the same absolute dead time for each event results in a higher and higher relative dead time until the event rate is totally dominated by readout dead time. Accelerator upgrades that increase the collision rate significantly would result in a big increase of the relative dead time unless the readout electronics is also redone.

A procedural option is to run 24 hours a day, 7 days a week. Since producing the collisions with the accelerator and taking data with the detector cannot go on unsupervised, this means shift operation for both, just like for an assembly line. This is a service work usually handled by the physicists that are part of the experiment. I myself have been taking shifts for both the CLEO and BaBar experiments.

CHAPTER 3

CESR and CLEO

Following the more generic description of a particle physics experiment at the end of the last chapter, I now want to go into much more details describing a particular collider experiment.

For a collider experiment we need a particle accelerator that can accelerate particles to high kinetic energies and we need a detector that can observe what happens when we collide these high momentum particles with other matter. One type of particle that can easily be obtained and accelerated in the lab is the electron. We can produce free electrons as easily as heating a piece of metal. If the electrons are placed into an electric field we have the building blocks of a particle accelerator that produces high momentum electrons. For these electrons to reach high momenta, all of this has to be done in a vacuum to avoid collisions with air molecules. Positrons have to be produced in collisions, for an e^+e^- collider the usual way to do this is to collide high momentum electrons with a target. In matter these positrons would almost immediately annihilate with electrons, but since we work in a vacuum, this doesn't happen. The following paragraphs about accelerating electrons are equally valid for positrons, in fact, they apply to any kind of charged particle.

The maximum kinetic energy we can accelerate the electrons to is limited by the electric field strength and by the distance over which the electrons remain in the field. To achieve higher kinetic energies one can increase the strength of the electric field. This is being done, but there are technical limitations one runs into at some point. Current particle accelerators use RF cavities (devices through which power is coupled to the beam) with field gradients of about 7 MV/m. Another option is to accelerate the electrons over a longer distance. One accelerator that uses this approach of accelerating electrons over a long straight distance is the Stanford Linear Accelerator (SLAC). It consists of a straight (linear) 2 mile long vacuum tube in which electrons or positrons are accelerated up to energies of 50 GeV. In previous experiments these electrons or positrons were used directly to hit fixed targets. Nowadays the linear accelerator at SLAC is just the first stage of a larger accelerator for BaBar, one of the collider experiment I have been working on. An upcoming experiment that will also use this linear approach is the planned International Linear Collider (ILC), although instead of hitting a fixed target they will accelerate electrons from one side and positrons from the other side and collide them in the center. Depending on the final design, RF cavities with field gradients between 20 and 40 MV/m will be needed for the ILC.

Increasing the linear distance over which to accelerate the electrons is only one way to increase the time they spend in the electric field. One can also use the fact that moving charged particles experience a force perpendicular to the magnetic field lines. Instead of building a straight beam pipe (just another name for a vacuum tube) in which to accelerate the electrons, we can build a circular beam pipe and use magnets to bend the electron trajectories to follow the beam pipe. We call this kind of particle accelerator a synchrotron.

It's now easy to get longer distances over which to accelerate the electrons. In certain parts of the ring the electrons travel through an electric field that accelerates them. The more often the electrons traverse the ring (number of revolutions), the more often they pass through the accelerating electric field. During every revolution the electrons gain kinetic energy when they pass through the electric field. If that would be all there is we could reach any kinetic energy we wanted, but there are reasons that prevent this. The strength of the magnetic field needed to bend the electron trajectory to a certain radius of curvature depends on the momentum of the electron. As the electrons gain kinetic energy, the magnetic fields have to be adjusted accordingly. At some energy one reaches a point where the magnets just cannot generate fields strong enough to keep the beam within the beam pipe. Another problem is that charged particles under acceleration emit photons. The electrons in the synchrotron are under quasi-constant lateral acceleration by the magnets to keep the beam within the beam pipe. Therefore the beam constantly looses energy through the emission of photons (synchrotron radiation). The energy lost to synchrotron radiation is proportional to the fourth power of the particle energy and is inverse proportional to the square of the radius of the path. The energy of the electrons is predetermined by the collisions center of mass energy we want to achieve. But in a larger ring with a bigger radius the electrons will lose less energy due to synchrotron radiation than in a ring with a smaller radius. The maximum kinetic energy for the electrons is reached when the energy lost due to the synchrotron radiation equals the energy gained by the electric field (assuming the magnets are strong enough to keep a beam of that energy within the beam pipe).

The output of the synchrotron is pulsed, we inject electrons, accelerate them up to the desired energy and use them. Then we repeat that process. But the synchrotron is not a collider, even though it can accelerate both electrons and positrons, it cannot do so at the same time. If we want to collide them, we need to store them when they leave the synchrotron. For this we use a storage ring, which is basically just a special form of a synchrotron. We still accelerate the electrons with electric fields, but instead of trying to increase their kinetic energy we just offset energy losses due to synchrotron radiation. Once we have electrons and positrons circling in the storage ring or rings, we can use them to do experiments. If electrons and positrons use the same ring (since they have opposite charge they will circle in opposite directions), we can collide them directly by adjusting the beam trajectories within the ring. If the electrons and positrons are in separate storage rings, we need a system that allows the two beams to pass through each other.

As an example of a modern particle physics experiment I will discuss the CLEO detector and the CESR e^+e^- storage ring. Both CLEO and CESR have been in in operation since 1979, although both have seen multiple upgrades and changes over their lifetime.

3.1 CESR

The Cornell Electron Storage Ring is an e^+e^- collider machine located on the campus of Cornell University in Ithaca, NY. It's a symmetric collider (electron and positron beams have the same energy) which operates at center of mass energies between 3 and 12 GeV. The low energy running capability has only been available since 2003 and is essential for the new CLEO-c research program that I will not discuss in this thesis. For the CLEO III experiment the collider operated at center of mass energies around 10 GeV.

CESR has three main components, as shown in Figure 3.1, a linear accelerator (LINAC), a synchrotron which handles most of the energy transfer to the electrons and positrons and a storage ring which sustains the electrons and positrons over extended periods of time.

The first part of the LINAC is the 'Electron Gun'. It basically is a heated filament which gives off electrons. These electrons are objected to an electric field and accelerated to 150 keV. The rest of the LINAC is a 30 meter long linear accelerator that accelerates the electrons up to 300 MeV before dumping them into the Synchrotron in a counter clockwise direction. To produce positrons a tungsten target is inserted into the linear accelerator part of the LINAC, about halfway down the beam line. 150 MeV electrons collide with the tungsten target and positrons are produced in these collisions. These positrons are accelerated through the remainder of the LINAC to 150 MeV and inserted into the Synchrotron in a clockwise direction.

The synchrotron completes the job of accelerating the electrons or positrons up to the energies we later want to collide them with. Similar to the LINAC, which can only either produce electrons or positrons, the Synchrotron can either accelerate electrons or positrons. It receives electrons or positrons at a few hundred MeV and brings them up to about 5 GeV. This corresponds to an acceleration from about 63% of the speed of light ($c = 299792458\frac{m}{s}$) to more than 99.9% of the speed of light. Accelerating the electrons or positrons to 5 GeV only takes about 4000

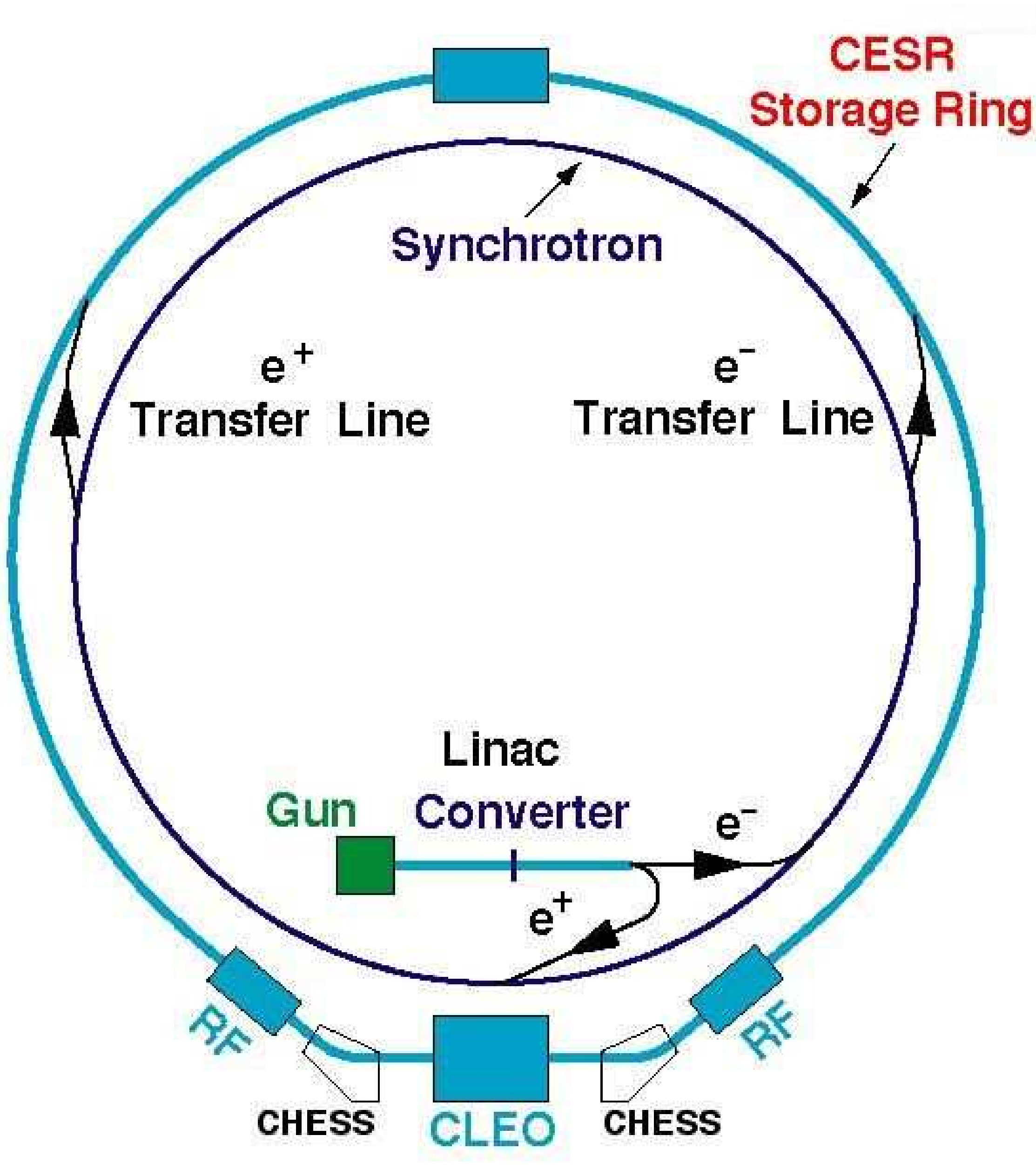

Figure 3.1: The Cornell Electron Storage Ring

revolutions in the Synchrotron or about 0.01 seconds. Once they reach 5 GeV, they are transfered to the storage ring. Again, same as for the Synchrotron, the positrons are injected clockwise and the electrons are injected counter-clockwise. This cycle is repeated 60 times a second for about 10 minutes for electrons and another 10 minutes for positrons.

The storage ring doesn't increase the electron's and positron's kinetic energy any further, but we still have to deal with energy losses due to synchrotron radiation. In Figure 3.1 you can see two blocks marked RF on each side of the CLEO detector. These are 500MHz RF cavities (two on each side) that replenish the lost energy. RF cavities are the devices through which power is coupled to the beam (the synchrotron also uses RF cavities). They generate the electric fields needed to accelerate the particle beam. Even though CESR is short for Cornell Electron Storage Ring, it's not really a perfect circle. The beam instead travels in straight lines between the poles of bending magnets arranged in 192 3-meter long sections [7]. The circumference of CESR is 768 meter.

Since the electron and positron have opposite charge, the same electric field can be used to accelerate them as long as they go in different directions. To prevent unwanted collisions between electrons and positrons, magnets are used to shape the particle trajectories so that the electron and positrons constantly 'zig-zag' around each other. The trajectories are chosen so that collisions can only occur in the center of the CLEO detector.

The particle beams are not continuous, but trains of closely spaced bunches. These bunches don't collide head on, but rather with a small crossing angle. During

CLEO3 data taking CESR operated with 9 bunch trains that contained 6 bunches per train and the bunches collided with a 2.7 mrad crossing angle.

Since the collisions occur between a particle (electron) and it's own anti-particle (positron), in the collision the electron and positron both get annihilated and converted to energy. Out of that energy other particles (quarks and leptons) are pair produced.

The number of collisions produced depends on a quantity called luminosity. Luminosity, or more precisely instantaneous luminosity, can be described as a rate of interactions per unit of cross section for a given process and is defined by

$$\mathcal{L} = fn\frac{N_{e^+}N_{e^-}}{A} \tag{3.1}$$

with f being the revolution frequency, n the number of bunches, N_{e^+} and N_{e^-} the number of electrons and positrons in each bunch and A the cross sectional area of the beams.

More useful for the data analysis is the integrated luminosity, which is the instantaneous luminosity integrated over a period of time

$$\mathcal{L}_{integrated} = \int \mathcal{L} dt \tag{3.2}$$

If I know the cross section σ of an interaction I can multiple it with the integrated luminosity to get the number of events of this type. For example, the cross section for the interaction $e^+e^- \rightarrow \tau^+\tau^-$ is about 0.92 nb (1 barn $\equiv 10^{-28}m^2$). A data sample with an integrated luminosity of 1.0 fb^{-1} will have

$$N_{\tau^+\tau^-} = \mathcal{L} \times \sigma_{\tau^+\tau^-} = 1.0fb^{-1} \times 0.92nb = 9.2 \times 10^5 \tag{3.3}$$

$\tau^+\tau^-$ pairs in it.

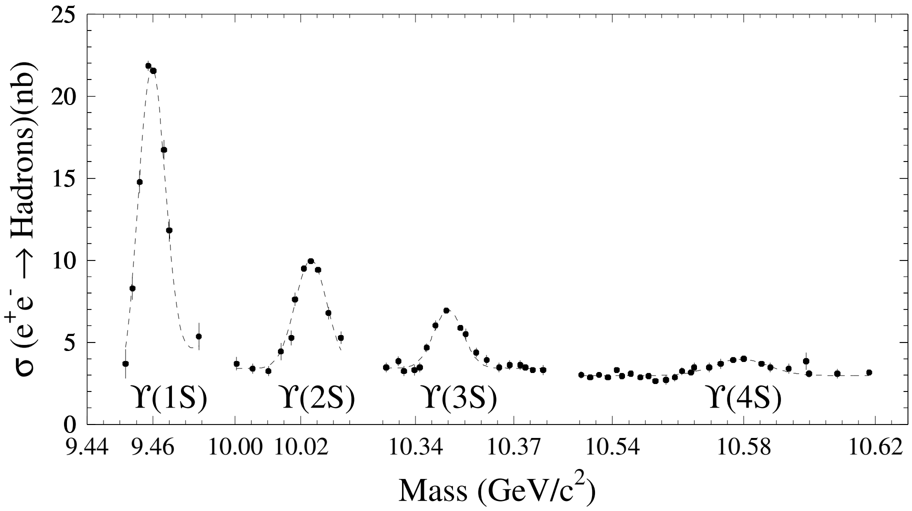

Figure 3.2: Hadronic cross section as function of center-of-mass energy [8] [9] [10].

3.2 CLEO3

The CLEO3 detector was commissioned in 1999 and collected data until the year 2003. Most of the data was collected at a center of mass energy of 10.58 GeV, which is the rest mass of the $\Upsilon(4\mathrm{S})$ resonance, an exited bound state of a b quark and a $\bar{b}$ anti-quark which just has enough mass to decay into two B mesons (mesons with a bottom quark or anti-quark)

$$e^+e^- \rightarrow \Upsilon(4S) \rightarrow B\bar{B} \tag{3.4}$$

Figure 3.2 shows the direct hadronic cross section vs. center of mass energy of the e^+e^- collision. The direct hadronic cross section is the cross section for the the pair production of quark pairs.

$$e^+e^- \rightarrow virtual\ photon\ or\ Z^0 \rightarrow q\bar{q} \tag{3.5}$$

All Υ resonances are $b\bar{b}$ bound states, but only the Υ(4S) is massive enough to decay to a pair of B mesons. Also visible in the plot is that the resonances sit on top of a smaller hadronic background, called "continuum". Events in the continuum background come from pair production of light $q\bar{q}$ pairs ($u\bar{u}$,$d\bar{d}$,$s\bar{s}$,$c\bar{c}$).

While most of the data was collected at 10.58 GeV directly on the Υ(4S) resonance, a sizable fraction of data was collected about 60 MeV below the Υ(4S) resonance. This off resonance continuum data is used to understand and remove the continuum background from B meson decay studies.

The CLEO3 detector has been modified recently and the current CLEO detector version, CLEO-c, is taking data at a much lower energies, where charm mesons are produced at threshold.

The CLEO3 detector was a multipurpose detector designed to study heavy quark physics, in particular bottom and charm quarks. It allows us to measure the properties of the particles produced in e^+e^- collisions, like for instance the already mentioned B mesons, charm mesons (mesons that contain a charm quark or anti-quark), baryons, τ pairs and others. Most of the particles produced directly in the collision decay before they have a chance to leave the beam pipe and enter the detector. In these cases what reaches the detector are not the particles produced directly in the collision, but particles much farther down the decay chain.

The CLEO3 detector is optimized for the detection of photons and long-lived charged particles like electrons, muons, pions, kaons and protons. Long-lived neutral particles like K_S's and Λ's which decay within the detector can be detected through their charged daughter particles. Other long-lived neutral particles like neutrons, K_L's and neutrinos cannot be detected with a high efficiency.

Since CESR is a symmetric e^+e^- collider, the center of mass frame of the event will be the same as the lab frame of the detector. Therefore the design of the detector is also symmetric. CLEO3 is using a cylindrical geometry with the beam pipe as the axis of the cylinder. By making the detector long enough and using detector elements in the forward and backward direction (called endcaps) we still get good solid angle coverage out of this geometry. The solid angle coverage is different for the various detector elements, but overall we cover about 95 % of the total solid angle with detector elements.

Most e^+e^- collider experiments (or any collider experiment for that matter) have chosen such a cylindrical geometry. Where it is possible, a spherical geometry is still used within the overall cylindrical shape of the detector. For instance, the CLEO3 electromagnetic calorimeter uses crystals. Ignoring the crystals in the endcap, the overall shape of the calorimeter is a hollow cylinder, but the crystals themselves are oriented in a way so that every crystal points to the interaction region. Both the general cylindrical shape and the orientation of the crystals can be seen in Figure 3.3, which shows the CLEO3 detector.

The CLEO3 detector consists of a combination of various subdetectors, each one responsible for gathering a different set of information about the event. The subsystem closest to the beam pipe is the Silicon Vertex Detector. It gives high precision information on the trajectories of charged particles that pass through it. Next comes the drift chamber, which also gives information on charged particle trajectories. In addition, the drift chamber provides information on energy loss due to ionization, which helps to identify the type of charged particle. Outside the drift chamber we have the Ring Image Cherenkov Detector (RICH), which measures the velocity

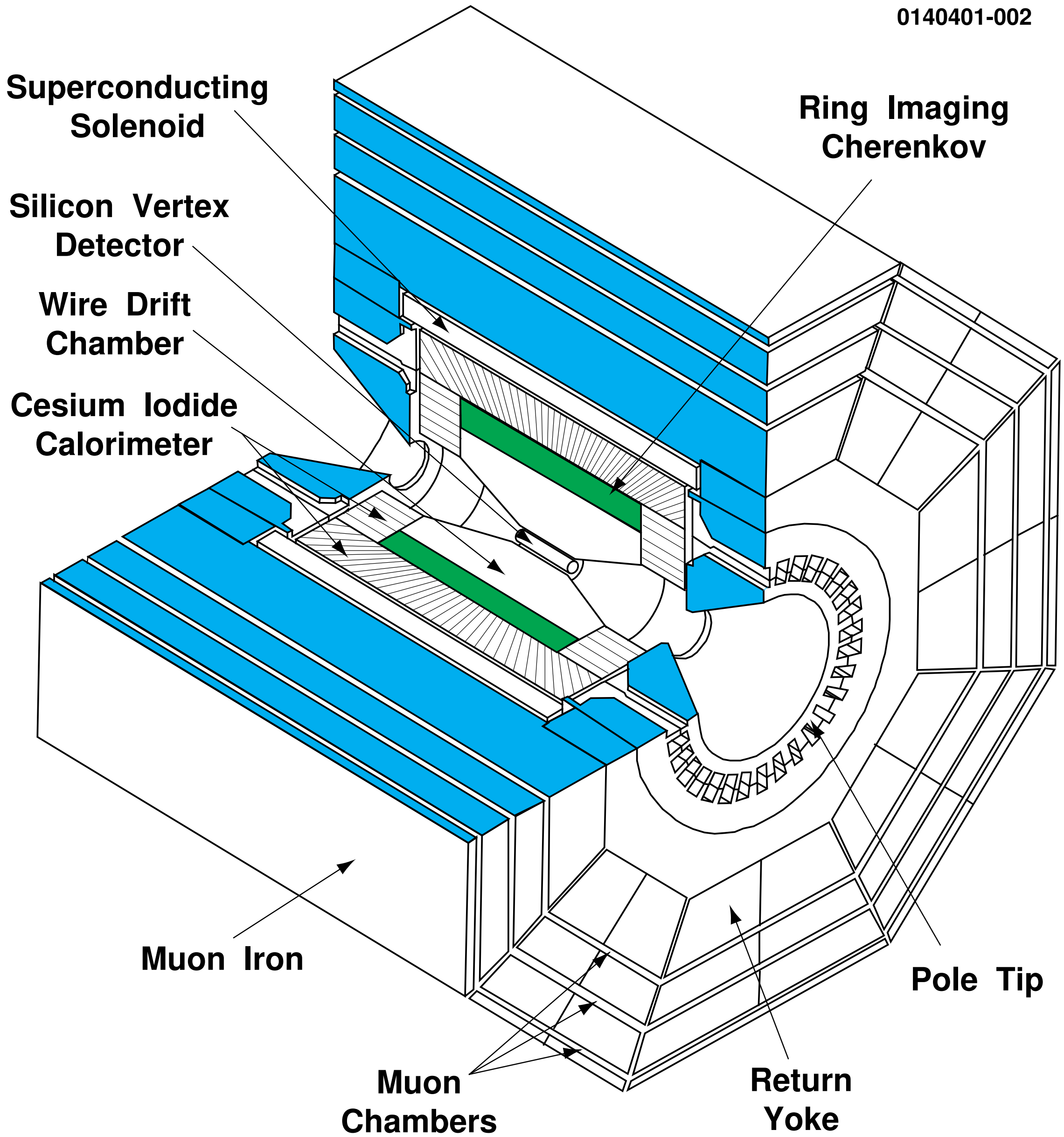

Figure 3.3: Cut-away view of the CLEO3 detector

of high momentum charged particles passing through. Just beyond the RICH is the CsI calorimeter. It measures energy deposited by particles passing through it. Electrons, positrons and photons deposit all their energy in the calorimeter, other particles deposit less (in some cases almost nothing). All the subsystems described so far are within a solenoid coil that produces a uniform magnetic field along the beam direction. Outside the solenoid there is a lot of iron to return the flux of the magnetic field and sandwiched between the iron plates are muon chambers, detectors to detect muons.

Following is a description of all the subdetectors. In the most basic sense all these different detectors work the same way. The particles we want to gather information about interact with the material of the detector and what we measure is the nature and the degree of these interactions. Our ultimate goal is to identify the particles and measure their properties. To identify a particle, we have to know its charge and invariant mass. The charge can be determined from the sign of the curvature of the particle trajectory in a magnetic field. The mass cannot be determined directly, but there are various other measurable quantities which depend on a particles mass and which can be used to derive the mass. For instance, if we can measure the momentum and the speed of a particle independently, we can calculate it's mass.

3.2.1 Superconducting Solenoid

While not directly a subdetector, the superconducting solenoid is a major part of the CLEO3 detector. Charged particles follow a curved trajectory in a magnetic field and measuring that curvature allows us to calculate the particles momentum.

The solenoid is made from aluminum-stabilized superconducting cables which have to be cooled by liquid helium. These cables carry a current of 3300 Amperes and produce a 1.5T magnetic field parallel to the beam and uniform over all the detector elements except the muon chambers. Just outside the solenoid there is lots of iron, which acts as a return for the magnetic field flux, as structural support for the whole detector and also as a filter for the muon chambers.

3.2.2 Silicon Vertex Detector

The purpose of the Silicon Vertex Detector (SVX) is to determine charged particle trajectories. As the name already suggests, the active element in the detector is silicon. Silicon is a semiconductor and charged particles interacting with it cause the creation of electron-hole pairs. If there is an electrical field applied to the silicon detector elements, the electron-hole pairs will drift along the electric fields lines until they reach the edge of the material and can be readout as a charge pulse. The CLEO3 SVX uses double-sided microstrip detectors. Each wafer is $53.2 \times 27 \times 0.3$ mm big and contains silicon sensors consisting of 512 strips on each side. The strip spacing is 50 μm for the side that measures the r-ϕ direction and 100 μm for the side that measures the z direction. Combining the two measurements gives us a point in space, a location for the charged particle with a resolution of 11 μm in the r-ϕ direction and 24 μm in the z direction [11].

This gives us a single position measurement. To get a trajectory we need multiple data points. That's why the SVX is made up from multiple layers. As the charged particle moves outward from the interaction point, it passes through each layer.

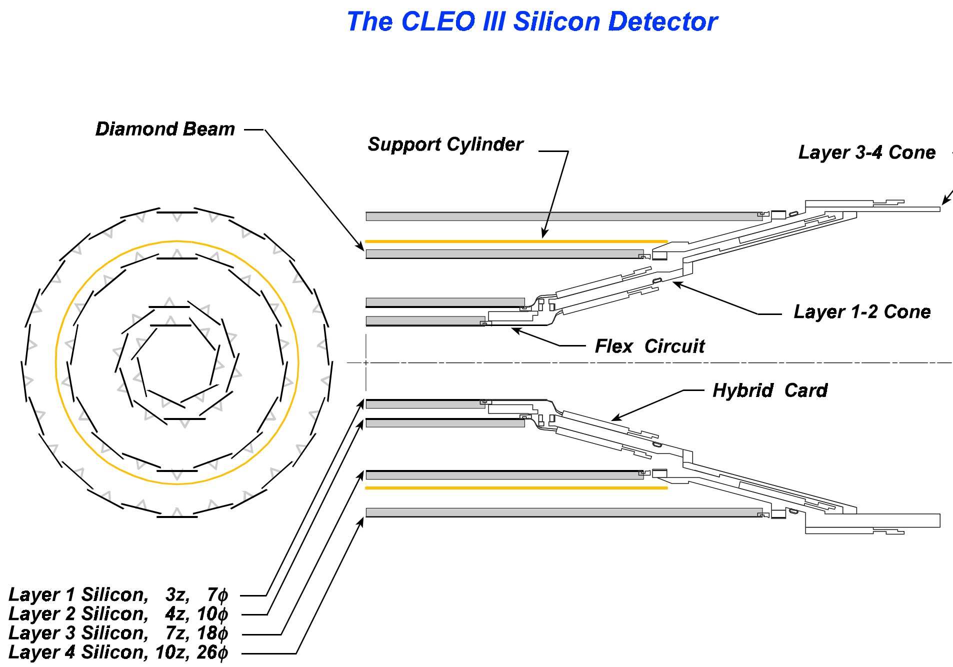

Figure 3.4: View of the SVX down the beam line, next to a side view

Figure 3.4 shows a schematic view of the SVX detector, both down the beam line and from the side. The different layers are clearly visible. Each layer consists of a number of ladders oriented parallel to the beam pipe. Each ladder itself is composed from multiple wafers attached end to end.

Overall the SVX covers 93% of the total solid angle. What is also visible in Figure 3.4 is that the layers have different length. Table 3.1 lists the individual lengths and other important quantities for each layer.

Altogether there are 61 ladders and 447 silicon wafers in the Silicon Vertex Detector.

Layer	# Ladders	# Wafers/Ladder	Length (cm)	Radius (cm)
1	7	3	16.0	2.50
2	10	4	21.3	3.76
3	18	7	37.3	7.00
4	26	10	53.3	10.10

Table 3.1: Characteristics of the various layers of the SVX [11].

3.2.3 Drift Chamber

As with the SVX, the primary purpose of the Drift Chamber (DR) is to determine the trajectory of charged particles. In the DR, the active detector element is a gas. CLEO3 is using a gas mixture of helium (60%) and propane (40%). A charged particle passing through this gas mixture will cause ionization. To measure the location of the ionization we need an electrical field, which is provided by a multitude of wires, of which some are grounded and some are at high voltage. The basic setup of the CLEO3 DR is three field wires surrounding a sense wire. The sense wire is held at a voltage of +2000 Volts relative to the field wires. The free electrons produced by the ionization will travel toward the sense wire. Since they are moving through an electric field, they will be accelerated and at some point have gained enough kinetic energy to ionize more gas molecules. Due to the $\frac{1}{r}$ dependence of the electric field and the therefore very high field strengths close to the wire, this results in an "avalanche" of electrons reaching the sense wire and causing a current flow. By measuring the drift time (time it takes for the electrons to drift to the wire) we can calculate how distant the ionization occurred from the wire.

The CLEO3 Drift Chamber has 47 cylindrical layers. Each layer is made up from multiple cells each with three field wires and one sense wire as mentioned above. The sense wires have a diameter of 20 μm and are made of gold-plated tungsten. The field wires are 110 μm in diameter and made of gold-plated aluminum. The inner 16 layers are axial layers and have their wires strung parallel to the beam pipe. This allows to measure positions in the r-ϕ direction, but not in the z direction. For that reason the outer 31 layers are stereo layers with wires strung at angles from 21 to 28 mrad with respect to the beam axis. All layers together have 9796 sense wires, 1696 axial wires and 8100 stereo wires. In the end we achieve a spatial resolution of 110 μm in the r-ϕ direction and 1.2 mm in the z direction.

Usually a charged particle will pass through the DR and ionize gas molecules in multiple locations. Together with the position information from the SVX we can fit a trajectory to these position measurements. Because both the SVX and the DR are within a 1.5 Tesla magnetic field, charged particles will move along a circular path, whose radius of curvature only depends on the strength of the magnetic field and the momentum of the particle perpendicular to the magnetic field lines. By fitting the trajectory and determining it's radius of curvature, we can determine the transverse momentum of the charged particle using this equation

$$p_t = e \cdot B \cdot r \cdot Q \tag{3.6}$$

where p_t is the transverse momentum in GeV, B is the magnetic field strength in Tesla, r is the radius of curvature in meters, $e = 0.3$ and Q is the charge of the particle in units of electron charge.

Another information we can immediately gather from the way the trajectory is curved is the charge of the particle. Positively charged particles will bend in one direction, negatively charged particles will bend in the other direction.

But apart from measuring positions, we can do more with the DR. As a charged particle moves through the DR, it looses energy. Each ionization of a gas molecule causes it to loose energy. Charged particles with the same momentum but different masses will loose energy at different rates. Figure 3.5 shows the rate of energy loss, $\frac{dE}{dx}$, against the momentum for various particle types.

We can use this to identify the type of particle. As seen in the figure, at higher momenta this becomes more and more difficult as the $\frac{dE}{dx}$ distributions for pions, kaons and protons overlap.

3.2.4 Ring Image Cherenkov Detector

The CLEO3 Ring Image Cherenkov Detector (RICH) is located just outside the Drift Chamber. It's primary purpose is to get additional information to separate different types of charged particles, in particular at high momenta (where the particle identification using $\frac{dE}{dx}$ has problems).

The RICH operates based on the Cherenkov effect, which is the fact that charged particles passing through a material faster than the speed of light in that material result in a cone of photons being emitted at an angle θ_C. The angle θ_C is defined as

$$\cos\theta_C = \frac{1}{n\beta} \tag{3.7}$$

with n the refractive index of the material the charged particle passes through and β the velocity of said particle divided by the speed of light in vacuum. That means if we are able to measure the angle of the light cone, we can determine the velocity

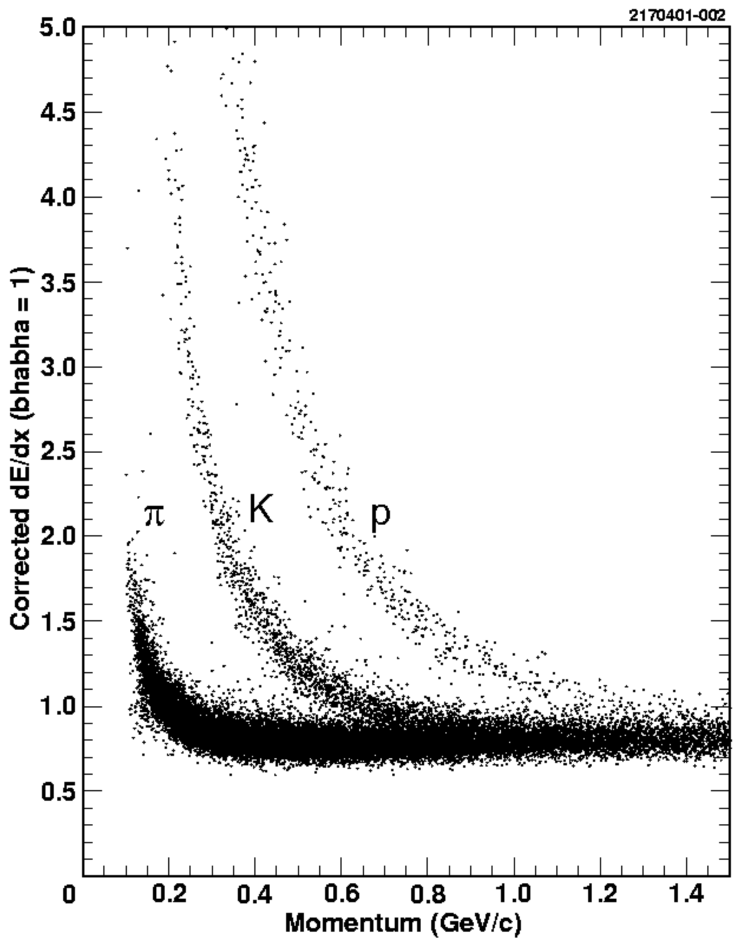

Figure 3.5: $\frac{dE}{dx}$ vs. momentum for pions, kaons and protons

of the particle. Together with the momentum we got from the measurement of the radius of curvature of the track in the DR and SVX, we can determine the mass of the particle and thus identify what type of particle it is.

If you look at the equation for θ_C, you notice that if $\beta < \frac{1}{n}$, the cosine becomes larger than 1, which doesn't make any sense mathematically. What this means physically is that if the velocity of a particle is too low, there won't be any light cone and we won't be able to measure the speed of the particle.

The CLEO3 RICH has three parts, as shown in Figure 3.6 [12]. First the charged particle passes through the radiator, a material with a very high refraction index. In the CLEO3 RICH the radiator is a 1cm thick layer of Lithium Fluoride (LiF). Photons are generated in the radiator and pass through a 15.6 cm thick expansion volume filled with N_2 gas at atmospheric pressure. The purpose of the expansion volume is to give the photons some room to separate to form a ring. At the end of the expansion volume we detect the photons with multi wire proportional chambers (MWPC) filled with a mixture of gaseous Triethylamine (TEA) and methane (CH_4). The TEA is photosensitive and the photons passing through it cause it to emit photoelectrons, which start to drift along the electric field lines toward 20 μm diameter Au-W anode wires. Close to the wires we get avalanche multiplication, the same effect that happens in the drift chamber. But we don't read out the charge pulse from the wires directly, but instead an induced charge in 8.0 x 7.5 mm cathode pads, of which there are 230400.

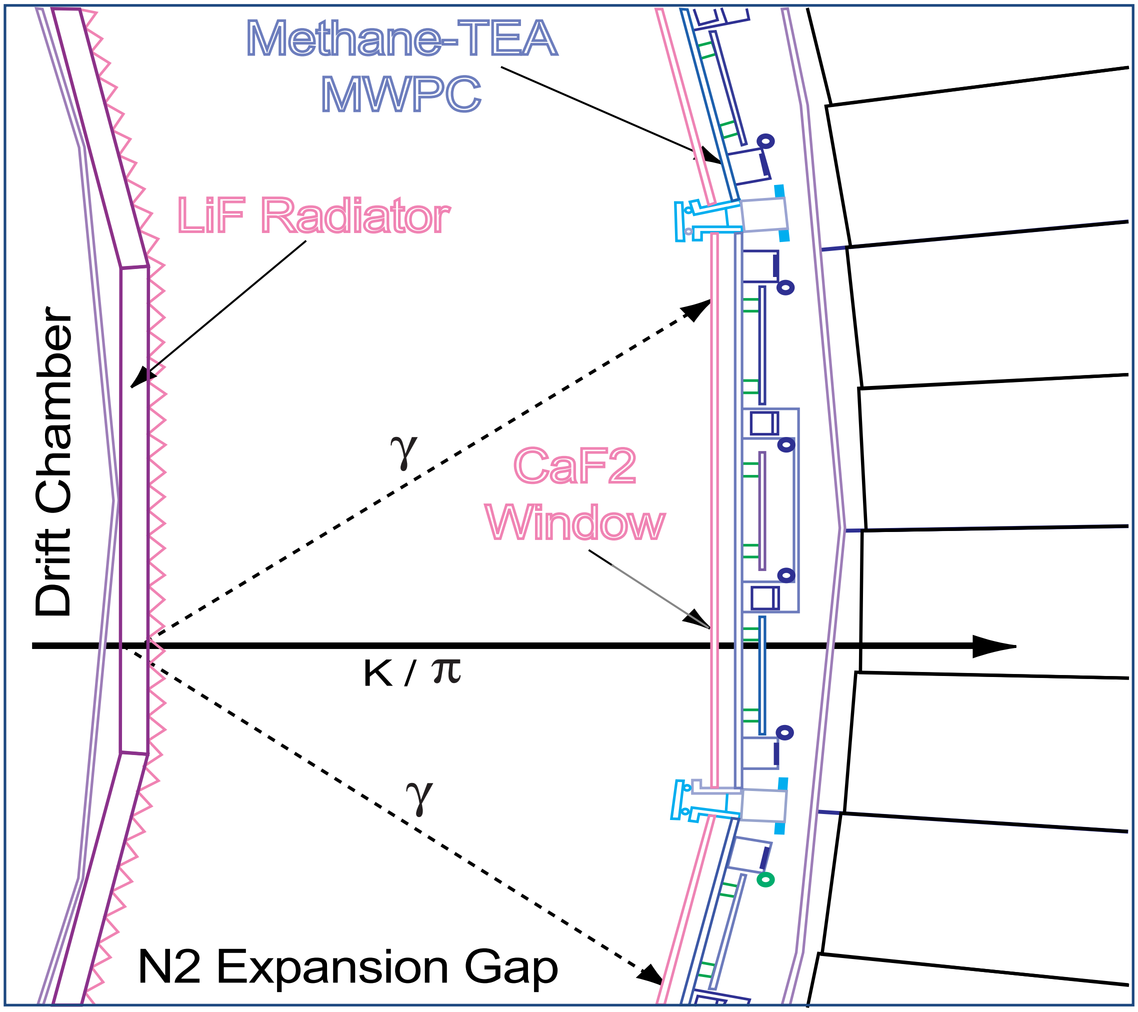

Figure 3.6: Schematic of the RICH detector

3.2.5 CsI Crystal Calorimeter

A calorimeter is a device that measures energy. In CLEO3 we use an electromagnetic calorimeter made from Cesium Iodide (CsI) crystals. There are two sections, the barrel with 6144 crystals and the two endcaps, one in the forward direction and the other in the backward direction, with 820 crystals each. The crystals in the barrel section are all aligned to point to the interaction point, the crystals in the endcaps are parallel to the beam. The barrel crystals cover polar angles $> 32°$, the endcaps cover between $15°$ and $36°$. Altogether the calorimeter covers 95% of the solid angle.

Cesium Iodide (CsI) is a scintillating crystal that produces light when particles pass through it. When a charged particle enters the CsI, it reacts electromagnetically with the atoms in the crystal and produces light (bremsstrahlung). Photons (either entering the calorimeter from the outside or bremsstrahlung generated within the calorimeter) can pair produce to e^+e^- pairs which again interact with the crystal and emit more bremsstrahlung. Thus a cascade of bremsstrahlung and pair production is set into motion that only ends when the photons have too little energy left to create e^+e^- pairs. We end up with a shower of light. All the produced light is read out at the end of each crystal by four photo-diodes. Photons and electrons will loose all their energy in the calorimeter (their trajectories end here). Heavier charged particles (like muons or charged hadrons) will only leave a fraction of their energy in the calorimeter since they are not as effected by bremsstrahlung as electrons.

A particle can also interact strongly with the nuclei of the atoms in the CsI crystals, producing a hadronic shower. Hadronic showers can occur everywhere in the detector, with any kind of material, be it another detector element or support structure. Examples are the wires in the drift chamber or the support structure that holds the silicons vertex detector in place. For the most part the hadronic showers are undesired and we try to avoid them as much as possible by using very light material for the detector construction and also as little of it as possible. But strong interactions with the calorimeter crystals, the resulting hadronic showers and electromagnetic reaction of the charged tracks in the hadronic showers with the crystals is the only way for CLEO3 to detect neutral hadrons like neutrons and K_L's.

Most showers don't stay contained to just a single crystal. They spread out over multiple crystals. The combination of crystals that belong to a shower is called a cluster. The cluster is used to reconstruct the total energy loss in the calorimeter and the direction of the incoming particle. The performance of the detector (energy and angular resolution) depends on the amount of material between the interaction point and the calorimeter since material that blocks the calorimeter degrades the energy resolution. The central barrel region, which covers about 71% of the total solid angle, has the best performance with an energy resolution of 1.5% at 5 GeV and 3.8% at 100 MeV and an angular resolution of 3 mrad at 5 GeV and 11 mrad at 100 MeV. The resolution in the end-cap regions is about 20% worse.

3.2.6 Muon Chambers

The muon chambers are detector elements embedded in the iron of the magnetic field flux return. The iron isn't solid but layered, with muon chambers between the layers. The muon chambers themselves are proportional counters within plastic tubes using a mixture of 60% helium and 40% propane. They are used to measure the position of a particle, similar to the drift chamber. But different than the drift chamber, we are not measuring drift times. A charged track passes through the gas, ionizes it, electrons drift toward the single wire within the tube since it's at +2500 V, the charge is read out. Each tube has a resolutions of 2.4 cm. The tubes only give us information about the position in r-ϕ, to also get a position measurement in z, there are 8 cm copper strips that are placed perpendicular to the tubes. Their spatial resolution is 2.8 - 5.5 cm.

From the operating principle it's clear that any type of charged particle can leave a signal in this type of detector. So why do we call them muon chambers? All strongly interacting charged particles will interact with the Fe nuclei in the return iron. A small fraction might make it through the first layer or layers, but eventually they all will be stopped. That leaves the charged leptons. The τ lifetime is so short that virtually all of them decay before reaching the muon chambers. The electron's and muon's lifetimes are long enough that they should both reach the muon chambers. As mentioned in Subsection 3.2.5, electrons will loose all their energy in the calorimeter due to bremsstrahlung. The energy lost due to bremsstrahlung is inverse proportional to the square of the rest mass of a particle and because of the much higher mass of the muon, it is much less effected by bremsstrahlung than the electron. Muons only loose a small fraction of their energy in the calorimeter. So the conclusion is that if we detect a charged particle in the proportional counters behind the iron layer or layers, there is a very high probability that it's a muon. That's why we call this detector a muon chamber.

CHAPTER 4

CLEO III Data Acquisition System

When I joined the Ohio State CLEO group in 1997, the CLEO experiment was finishing data taking with the CLEO II detector. Design and construction of the CLEO III detector was ongoing in parallel and the Ohio State was heavily involved in it. Our group was, among other things, working on the CLEO III Data Acquisition System.

The Data Data Acquisition System is responsible to manage the flow of the data from the detector up to the point where we write it to a storage medium. It is an integrated system which has three components with different functions. Data Readout handles the flow of the data, from collecting data from all the subdetectors to writing it to storage. The other two parts play supporting roles to make sure the Data Readout works correctly. RunControl handles starting and stopping the collection of data. SlowControl monitors and controls the detector. It also monitors the data flow through the Data Readout system and checks the quality of the data.

Figure 4.1 shows a schematic overview of the complete CLEO3 DAQ system.

In Figure 4.1 there is no mention of RunControl, it is included as part of the SlowControl system. Even though RunControl and SlowControl have different

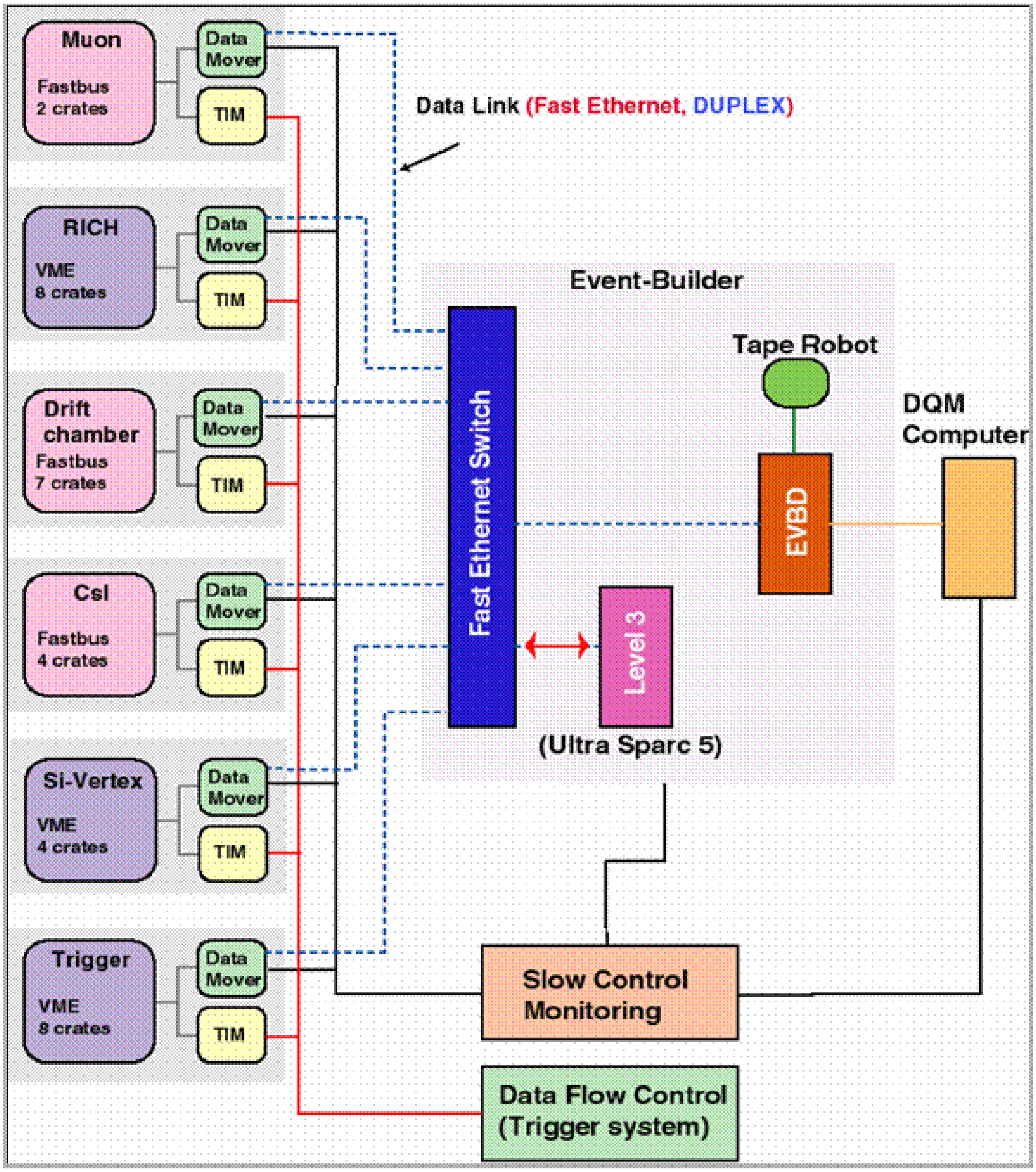

Figure 4.1: Overview of CLEO3 DAQ system

purposes, their implementation makes it hard to say exactly where one ends and the other begins.

I personally started to work on the CLEO III Data Acquisition System in 1998 and continued working on it until 2002. Between 1999 and 2001 I spend two years at Cornell University working exclusively on the commissioning of the CLEO3 detector. I worked primarily, but not exclusively, on the SlowControl system.

4.1 Trigger

The crossing rate of the e^+e^- beams at CESR is 72 MHz. Taking all the sub-detectors together the CLEO3 detector has about half a million readout channels. Reading out the detector every time would generate enormous volumes of data in a very short time. Fortunately, most of the interactions are not very interesting from a physics point of view. Interesting physics happens much more rarely than at 72 MHz. Table 4.1 [13] shows

Process	σ_{total} (nb)
$e^+e^- \to e^+e^-$	72
$e^+e^- \to \gamma\gamma$	6.2
$e^+e^- \to \mu^+\mu^-$	0.92
$e^+e^- \to \tau^+\tau^-$	0.92
$e^+e^- \to q\overline{q}$	3.5
$e^+e^- \to B\overline{B}$	1.0
$e^+e^- \to e^+e^-X$	2-25
Total	> 86

Table 4.1: Typical cross-sections for physics events at $E_{cm} = 10.58$ GeV.

the cross sections for some typical e^+e^- interactions at a center-of-mass energy of 10.58 GeV. The numbers assume an active detector region of both barrel and endcap. At a typical CESR instantaneous luminosity of 1.28×10^{33} cm^{-2}s^{-1} these cross sections result in rate of interesting physics events of about 110 Hz.

To decide if an event is interesting enough to be readout, we use a system called Trigger. A trigger is basically a very fast decision maker. It looks at a subset of the detector information and based on these information it makes a fast decision if the event should be readout or not.

The CLEO3 Level1 trigger has a maximum output event rate of 1 kHz. A trigger decision is made every 42 ns based on shower numbers and topology information from the calorimeter and track count and topology information from the drift chamber. If a positive trigger decision is made, the event readout process is started (further details below). The trigger is designed as a pipelined trigger. This means that the trigger processing is broken up into several short steps, allowing multiple events to be processed in parallel in different steps.

The Level1 trigger itself is deadtime-less until a successful trigger occurs. A small dead-time ($\sim 2\mu$s) is then incurred for data conversion (digitization and transfer of detector signals to frontend data crates).

The flow of the data is controlled by a simple design. We only allow the L1 trigger to accept new events if sufficient buffer space is available to store this new event. In the CLEO3 design that means the data boards in the frontend data crates need to have enough free buffer space to store the new event. I will explain this in more detail in Subsection 4.3.

4.2 Data Readout

The output of the Data Readout system are complete records of collisions or events. An event contains all the information about all detector signals resulting from the interactions of particles produced in a single collision. Each event is self-contained and independent of all other events.

The readout chain consists of multiple stages. The first stage are the frontend data crates which digitize and sparsify (reduce in size to save bandwidth) the signals coming from the various detector components. The separate event fragments are transfered to an Event-Builder that assembles them into the final event. The readout chain ends when the event is written to storage.

4.3 Frontend Data Crates and Data Flow Control

After a positive trigger decision is made, the detector signals are readout, digitized and transfered to the frontend data crates. The frontend readout electronics for the CLEO3 detector use either VME [15] or Fastbus [14]. As you can see in Figure 4.1, the CsI Calorimeter, the Muon Chambers and the Drift Chamber use Fastbus, while the other subdetectors use VME. Each data crate, both VME and Fastbus, needs a dedicated CPU that control the crate and handles the data readout. For the VME crates we used commercially available Motorola VME PowerPC boards. For the Fastbus crates we had a problem since none of the commercially available crate controllers fulfilled all our requirements. We could have designed and build our own Fastbus crate controller, but that would have meant having two different CPU types and programming/debugging environments for the data crates. Instead we designed a VME-Fastbus interface that allowed us to use the same type of Motorola VME PowerPC boards as Fastbus crate controller that we already used in the VME data crates. We called this interface FRITZ [16]. This simplifies the Data Readout considerably since we only have to use one operating system and software development package for the crate controllers. For the readout and monitoring software it means that VME crates and Fastbus crates will more or less be handled in an identical fashion.

If you look at Figure 4.1 again, you can see that in each data crate, there are two components highlighted, the TIM and the Data-Mover.

TIM stands for "Trigger Interface Module". It acts as an interface between the trigger and the data crates. After the Level1 trigger has made a decision that the detector should be readout, it stops data-taking, ie. doesn't accept any further events, and sends a Level1 trigger signal, *L1*, to the TIM board in all the frontend data crates. The *L1* signal is then distributed over the crates backplane to all the data boards in the crate. The data boards activate a *Board_Busy* signal and start data conversion. The TIM module forms a logical OR of the *Board_Busy* signals and sends the resulting *Busy* signal back to the trigger. Once all the signal readout and conversion is done, the data boards release their individual *Board_Busy*. When the last data board has released *Board_Busy*, the TIM will deactivate it's *Busy* signal, thus indicating that the data crate is ready to accept the next event. To keep track of the number of event fragments stored in the data crate, a counter in the TIM is increased when the *Busy* signal is cleared. A non-zero value of this counter triggers the Data-Mover to move the event fragment from the data board buffer to the Data-Movers internal memory. Each transfered event fragment decrements the event counter in the TIM. All data boards in CLEO hold up to 7 event fragment. If the TIM event fragment counter reaches 7, the *Busy* signal remains asserted until event fragments are transfered to the Data-Mover and the TIM event counter falls below 7 again.

In CLEO3 the Data-Mover is a process running on the same Motorola VME PowerPC board that acts as a crate controller. The PowerPC board provides internal memory to buffer the event fragments transfered from the frontend data crates. This buffer is necessary to smooth out trigger bursts and data transmission delays. The PowerPC board also provides processing power to handle additional data sparsification (data processing to reduce it in size, reducing bandwidth requirements). The exact amount of processing power required varies from detector component to detector component. The Motorola VME PowerPC boards support VxWorks, a major real-time operating system, making the software development easier by allowing the use of commercially available software. They also have integrated Fast Ethernet interfaces, providing the data transfer path to the Event-Builder (described in the next section) and at the same time the control channel to monitor and control the frontend data crates.

4.3.1 Event-Builder and Level3

The next step in the data path is to move the data out of the Data-Mover into the Event-Builder. The Event-Builder needs to combine all the input data streams with the event fragments from the individual data crates and build full events. All the data crates are connected through Fast Ethernet links to a network switch that is also connected to the Event-Builder. Initially this connection was also realized with a Fast Ethernet link but to allow for more bandwidth, it was later replaced with a Gigabit Ethernet connection.

The Event-Builder itself is a software process running on a SUN UltraSparc computer with multiple CPUs. Another processes that also runs on SUN UltraSparc machines and directly effect the Data Readout is a software trigger called Level3.

The Level3 software trigger has to analyze all the events that are sent to the Event-Builder. For performance reasons it only looks at a subset of the available information in the event, namely the data from the CsI calorimeter, the Silicon Vertex Detector and the Trigger. If an event has sufficient energy deposits in the calorimeter or if the event has a track in the silicon that matches an appropriate hit in the trigger, the event is saved. These are the only two criteria that determine if an event is accepted by the Level3 trigger.

If an event is accepted by the Level3 trigger, it is then written by the Event-Builder to permanent storage. To smooth out fluctuations in the data taking rate and assure a constant write rate to tape, the events are first written to a large data store based on disk drives. In a later stage, independent from data taking, they are written to tape and archived.

4.4 SlowControl and RunControl

The SlowControl systems main purpose is to control and monitor the detector and the Data Readout. These two functions go hand in hand since without knowing the current state of the system, effective control is impossible. RunControl controls when we collect data, it starts and stops data taking. It is tightly integrated into the SlowControl system. Before we can start data taking, the detector and the components of the Data Readout system have to configured properly. During data collection, the SlowControl system is constantly monitoring detector and Data Readout conditions and can stop data taking if something goes wrong.

Another reason for monitoring the detector is to prevent damage to the machine. The various detector subsystems and their support infrastructure (power supplies, cooling systems etc.) are complex pieces of equipment that only work reliably and correctly under a certain set of conditions. If one or more of these conditions isn't set, for instance a supply voltage is wrong or a temperature is too low or too high, the subsystem cannot work as intended. This can cause data to become unusable for physics analyses. In a worst case scenario, even actual damage to the detector is possible. If actual damage can occur there is usually hardware protection in place because we don't want to rely on a human decision when seconds could make a difference. But notification of an operator is still necessary. In other cases, where there is no danger of damage but the collected data could be bad, a decision has to be made by an operator if the problem requires data taking to be stopped. Every downtime decreases the total integrated luminosity, so we really only want to stop data taking if it is absolutely necessary. The detector monitoring has to provide enough information for the operator to make that decision.

I will say more about the RunControl implementation later. Here I just want to discuss why we need a RunControl system in the first place. We want to collect as much integrated luminosity as possible. If that is the case, wouldn't it be best to collect data continuously, without any interruptions? That would mean we start data taking and never stop until the machine or detector has to be turned off.

For various reasons this is impractical. First there is the fact that the electron and positron beams degrade over time (interactions of beam with gas, collisions at the interaction point and elsewhere), which lowers the beam currents and hence the instantaneous luminosity. After some time it is better for the overall integrated luminosity to "refill" the beams then to keep running, even if data taking has to be stopped during the "refill". The BaBar and Belle e^+e^- collider experiments have overcome this problem by a method called "trickle injection". Trickle injection means that the beams are constantly refilled just enough to keep the beam current almost constant over time.

But even with trickle injection, there is a maximum time for continuous data collection after which it becomes difficult to handle the data just because of it's size. This is driven by the specifics of the computer software and hardware systems that handle the data.

Because of these issues, data taking is split into periods of time. Each of these time periods we call a run.

4.4.1 Hardware and Operating Systems

Altogether the DAQ system along with the various detector control systems, software trigger and online monitoring consists of around 100 computers. By computer I mean anything that has a cpu and memory and can run programs, this can be anything from a big Unix server down to an embedded controller.

Table 4.4.1 shows a list of the different hardware platforms, the operating systems used on each platform and what functionality they provide.

Hardware	Operating System	Function
Motorola VME PowerPC	VxWorks	Data board readout, Hardware controlling
SUN UltraSparc	Solaris	Event building, Central SlowControl Database, Event Display
Intel PC	MS Windows	Hardware controlling, GUIs

Table 4.2: The CLEO III Online computing platforms and their functions

All computers that are used in the DAQ system are part of the SlowControl system. If nothing else, the SlowControl system has to monitor that a computer used in the DAQ system is working properly. Only a subset of machines is used for the Data Readout.

4.4.2 Message Passing Protocols

Monitoring and controlling such a complex system requires connecting many processes running on different computers and exchanging messages between them. The most basic part of such a system is a common software layer or *communication layer* which provides the framework on top of which we can build hardware independent software modules (programs or libraries) that can handle the message transfer between the participating nodes.

One popular solution is the "BSD socket" library, since it's implemented on all UNIX systems (and most non-UNIX systems). All our hardware platforms from Table 4.4.1 come with "BSD socket" libraries. The downside is that it lacks a standardized message format and run-time setup of connections. A socket based system would have required lots of hard-wired configuration information such as IP addresses and port numbers and we would have had to define our own messaging protocol. To avoid these problems, we choose a CORBA based solution instead. See Appendix B for a description of CORBA.

After evaluating different CORBA implementations, we choose a solution from Visigenic Corp, now owned by Inprise (formerly Borland). It was available for both Solaris and Microsoft Windows, but not for VxWorks. In close collaboration with Visigenic, the CLEO3 DAQ group at OSU ported this CORBA implementation - Visibroker - to VxWorks for the Motorola PowerPC 604 platform.

CORBA is used mostly for SlowControl and RunControl and for interfacing the Data Readout to the SlowControl system. For the data transfer in the Data Readout system we use "BSD socket" for performance reasons.

4.4.3 General design

The SlowControl system can be split in three major parts. There are local components, central components and there are GUIs (Graphical User Interfaces).

Local SlowControl components are processes that run on a certain computer and provide functionality directly related to this computer. Every VxWorks PowerPC crate controller runs processes that are local SlowControl components. In contrast with this are the central SlowControl components, like for instance the ConfigManager, AlarmManager or Interlock server (all described in more detail below). The main functionality of central SlowControl components is not tied to the computer they are running on. Instead, the have connections to a large number of other SlowControl components, both local and central ones. These connections can go both way, the central component can provide needed information like configuration data or program code or it can send instruction for the other component to process.

At the end of the day, we want a human operator to control the DAQ system and through it the detector and data collection. For this purpose a set of GUIs is provided. One major design criteria is that even though the interface that allows the human operator to control the detector is provided by the GUIs, the actual detector operation is independent of the GUIs. All detector status information needs to be stored in the processes the GUIs connect to, allowing us to restart GUIs without effecting detector operation. At this point having local and central SlowControl components helps a lot since by having the GUIs only connect to the central SlowControl components, we limit the complexity of the system. There are exceptions to that rule and we have GUIs that connect directly to local components, but these GUIs are only used for monitoring and cannot effect detector operation.

In the next few subsections I will discuss some of the major components of the SlowControl system and what functionality they provide.

4.4.4 ConfigurationManager

The Configuration Manager is a central SlowControl component that surveys the state of all involved software components and insures the integrity of the system. For instance, if one of the frontend crates is not configured properly, it prevents us from data taking. Same for the necessary processes on the Solaris machines, like for instance the Event-Builder or Level3. The Configuration Manager is controlled by the Configuration Manager GUI (see picture in the Subsection 4.4.8), which defines what components are part of the current system configuration. While for data-taking we pretty much need all components in the system configuration, for some test scenarios only a subset is needed.

When we load a new configuration into the ConfigurationManager, it makes sure to initialize all the components with the correct constants and software versions, it will start necessary software and in general bring the SlowControl system into a state ready for data taking.

4.4.5 Interlocks

The Interlock system provides a simple way to allow components to take action based on condition changes of other components. A system where each component would have to interface to all the other components whose condition it depends on would be very complex and wouldn't scale very well since the complexity of the system would grow faster then the number of components. With the interlock system each component only connects to the Interlock server. In the Interlock server we define software interlocks that are basically just binary flag with two states, set or broken. An interlock can have multiple sources which are combined with a logical AND. That means that all sources have to have their interlock set for the global interlock to be set. Any component in the system can listen to any interlock and be notified about status changes. For an example how the Interlock system works see the description of the RunController in the next subsection.

4.4.6 RunController

The RunController is the main process that controls data taking and I will spend a little bit more time explaining it. I will explain in detail what happens during a

“BeginRun” run state transitions, which is the run state transitions initiated by the RunController to start a new run.

A “BeginRun” run state transitions is not instantaneous for most components. Calibration constants might have to be loaded, various programs might have to be run. In the end, a component can take from a few seconds up to almost a minute for it’s run state transition. Given that all the components in the system have to complete their run state transition before data taking can start, going through all components in sequence and waiting for their run state transitions to finish before going on to the next component is impractical because it would take a very long time. This is time that we could use to take data and increase the integrated luminosity. So instead of switching the components run state in sequence, we switch their run states in parallel. When the RunController begins a “BeginRun” run state transition, he sends a CORBA call to all components telling them to start their “BeginRun” run state transition. The CORBA call returns immediately, making sure we don’t get delayed. But since it returns immediately, we also don’t get any feedback on the status of the transition in the component. So how are we going to coordinate all the components run state transitions? We still need to know when the last component has finished it’s run state transition so that we can start data taking.

The solutions to this problem is the Interlock system and more specific the RunControl interlock. Each component that has run states and run state transitions (some monitoring components work independent of run states) is a source of the RunControl interlock. At the same time the trigger is listening to the RunControl interlock. If it’s broken, the trigger is disabled. The first thing a component does when it receives a “BeginRun” command, is to break the RunControl Interlock, making sure the trigger can't be enabled. Only after the last component has reset it's RunControl interlock and thus also reset the global RunControl interlock, can the trigger be enabled and data taking can start.

4.4.7 AlarmManager

The Alarm Manager acts as a central switchboard for all the components in the system where they can post messages. The primary purpose is to provide a single location where the system operator can view messages from all the components. The severity of these messages can vary, from simple information messages up to critical alarms. All the messages are also stored in a database.

The AlarmManager is a source of the RunControl interlock, which allows it to stop data taking by breaking the RunControl interlock when it receives a critical alarm from a component.

4.4.8 GUIs

The GUIs provide the interface between the DAQ system and a human operator. For various reasons, among them (relatively) easy coding, platform independence and support of CORBA, we choose Java as the platform to write these GUIs. Since one of the reason for choosing Java is its platform independence, we then choose for cost reasons to run the GUIs on commodity Windows PCs.

All the GUIs run in a common framework that provides a GUI base class and common functions for all GUIs. We call this a SessionManager. Within the SessionManager we can start any of the GUIs used for the DAQ system. In normal operation we use multiple Windows PCs, each one running a SessionManager with a certain set of GUIs. Figure 4.2 shows the SessionManager running on the main console in the CLEO control room.

There are GUIs shown here for systems I didn't explain, but you can also see the ConfigurationManagerGUI, the InterlockGUI and the RunControllerGUI.

4.5 Summary

The CLEO III DAQ system was commissioned together with the CLEO3 detector in 1999 and has been in operation ever since. It it still in use today, although in a slightly modified version, with the CLEO-c detector, a modified detector based on the CLEO3 detector that is designed to collect data at charm production threshold.

Working on the CLEO III DAQ system was an often challenging, but also satisfactory experience. I learned a lot about software development during my time on CLEO.

In 2002 our research group left the CLEO collaboration and joined BaBar, a competing e^+e^- experiment. The rest of this document will describe work I did after joining the BaBar collaboration.

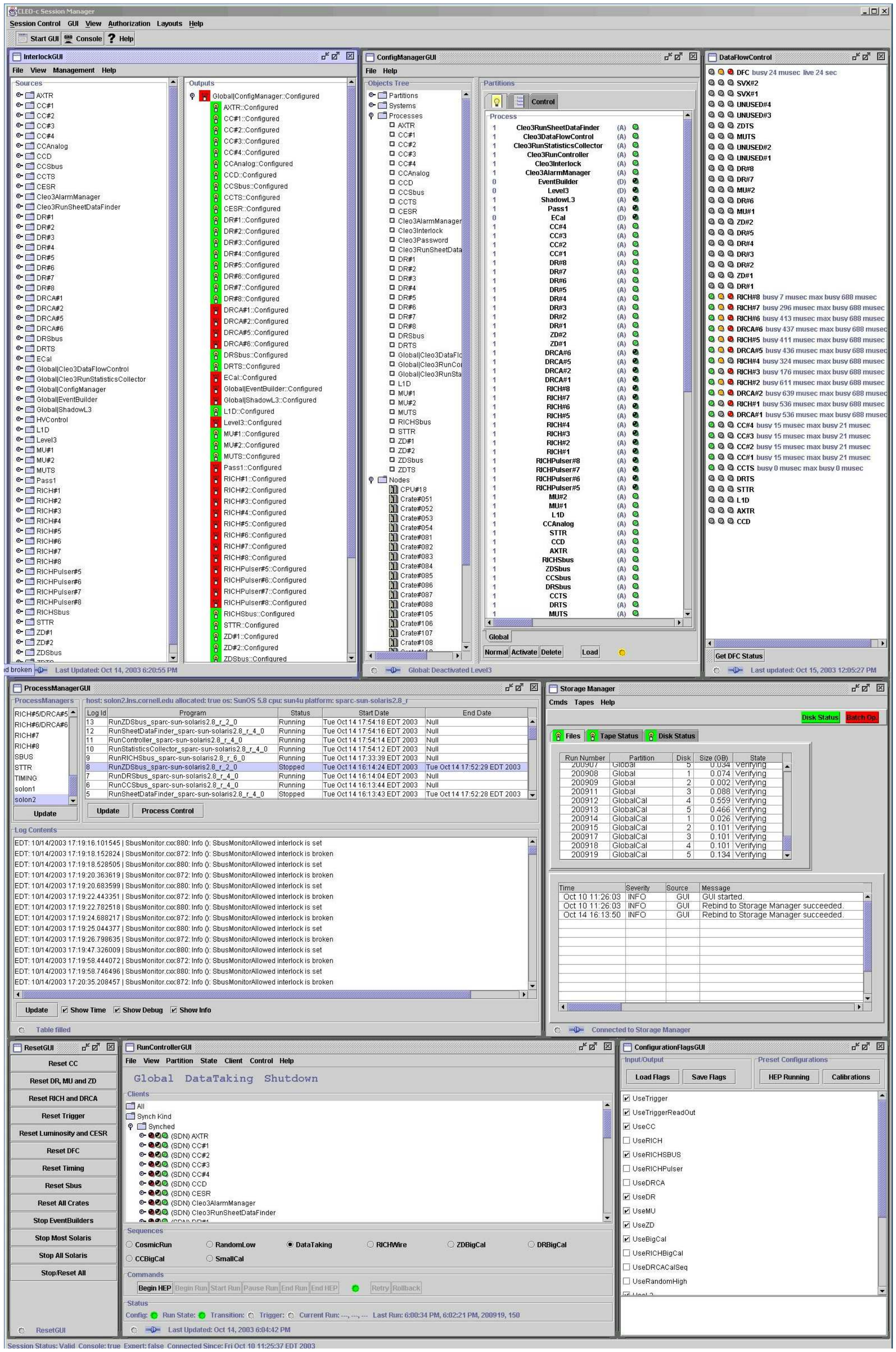

Figure 4.2: Main control SessionManager

CHAPTER 5

BaBar Monte Carlo Simulation

When our group joined the BaBar experiment in 2002, I started to work on designing and building a computer farm for BaBar Monte Carlo (MC) production. This farm became operational in December of 2002 and has since produced a total of about 500 Million MC events. I have been maintaining this computer farm until now. In addition I became the BaBar SP coordinator (SP stands for "Simulation Production") in November of 2004. Some of my duties due to this positions are described below in Section 5.6.

For these reasons I have a special interest in Monte Carlo simulation at BaBar and in this chapter I am going to describe in general why we need simulated events for particle physics experiments, some of the issues with the simulation and also provide some details about the Monte Carlo simulation at BaBar.

5.1 Why do we need Monte Carlo ?

As explained in Subsection 2.3.2, there are three reasons why we need simulated events. They are

- to understand the detector acceptance

- to find cuts that reject more background than signal events
- to understand how many signal events these cuts remove

There is not much to be said about the first item. The detector acceptance depends on the exact detector geometry (can't detect something that never moves through the detector), but also on the efficiency of the detector to give us a usable signal for a particle that does move through the detector.

The other two points are directly related to our ability to do a data analysis. Lets assume we use the recorded data to measure the branching fraction for a process

$$A \to BC \tag{5.1}$$

First we have to find out how many events in our data sample contain particle A, then we have to determine in how many events with particle A present did particle A decay into particle B and C. Searching for these events is in principle very easy, we just need to find selection criteria that are fulfilled for the events we want to keep and are not fulfilled for any other. To determine these selection criteria, we use simulated events. We produce simulated events of the specific mode we are interested in, from now on called signal mode. But we also simulate events of all other modes. Then we 'just' have to find a good set of selection criteria. Good in this sense means that most signal mode events will pass these criteria and most other, non-signal events (background events) won't pass these criteria.

5.2 Short introduction to BaBar

BaBar is in many aspects very similar to CLEO3. At both experiments we study e^+e^- collisions, at BaBar these collisions occur at the PEP-II collider at SLAC. Most of the data is taken on the $\Upsilon(4S)$ resonance at a center-of-mass energy of 10.58 GeV, same as for CLEO3. One big difference is that PEP-II uses asymmetric beams. Instead of colliding e^+ and e^- beams with energies of 5.29 GeV each, at BaBar 3.1 GeV positrons and 9 GeV electrons collide inside the BaBar detector. This makes the construction of both the accelerator and the detector more complicated, but it has advantages for the study of B meson decays. Since we take data on the $\Upsilon(4S)$ resonance, which is just above production threshold for $B\bar{B}$, the B mesons are produced almost at rest. That means they won't move much before decaying, making the separation of the decay vertex of the B meson from the interaction point very difficult. The B mesons will only be at rest in the center-of-mass frame of the collision. Using asymmetric beams, the center-of-mass frame of the collision and the lab frame in which the detector is in are not identical anymore. Even though the B mesons are almost at rest in the center-of-mass frame, in the lab frame they are moving. This results in a bigger, easier to detect, separation between B mesons decay vertex and interaction point.

For a more detailed discussion of the BaBar detector and it's various subsystems, see [21]. Even though the detector hardware and the software used to run the detector is different from what is used at CLEO, the same principles still apply. The physics of e^+e^- collisions is the same at both machines and at the end of the day we still want to collect information from the detector to determine and measure this physics.

5.3 Simulated Events

The goal is to have the simulated events match data events as closely as possible. To achieve this the simulation tries to follow the way an actual data event is produced as closely as possible. This starts with the collision and the particles produced in it, then follows these particles through the detector. The particles interact with the detector, leave signals that are readout and digitized.

The simulation can be divided into four stages.

5.3.1 Generation of physics events

First is the generator which is just the physics of e^+e^- collisions. It takes as input what type of event we want to produce and a list of allowed decay modes. We could for instance configure the generator to only produce a muon pair in the collision, even though in the real experiment this combination is produced in only a small fraction of all collisions.

The generator output is a set of four-vectors for the final state of the collisions and subsequent decays near the e^+e^- interaction point.

Generators are for the most part independent of the type of experiment since they just rely on the physics of the e^+e^- collisions. Our understanding of that physics is evolving, which means that generators have to evolve too. In the end, the simulation can only be as good as our understanding of what is happening at the collision and the subsequent particle decay.

The next stage takes the four-vectors produced by the generator and applies the particulars of the detector, in our case the BaBar detector, to them.

5.3.2 Particle transport and hit scoring

The particles produced in the e^+e^- collision travel from the interaction point outward through the detector, interacting with it. Interactions can occur with active detector elements like hits on wires in the drift chamber or energy deposits in the calorimeter. Interactions can also also occur with inactive detector elements, like hitting support structure and causing hadronic showers. Finally, instable particle can also decay while still being inside the detector.

While this stage depends on the BaBar detector, it only depends on the physical composition of the detector, what kind of material is located where. The next stage will go one step farther and introduce a dependency on the readout electronics.

5.3.3 Detector response and background mixing

In this stage the physical interactions between particles and detectors are translated into realistic signals, similar to those collected from the actual detector readout electronics. To let the simulated data resemble real data more closely, real background events may be mixed in, at a very small fraction, with the simulated events. The official BaBar MC used for analyses contains mixed in background events.

After this stage the simulated events are just like events readout from the detector. The next stage is not strictly part of the simulation, but is run on both data and MC equally.

5.3.4 Reconstruction

I already talked a little about the reconstruction and why it is performed in Subsection 2.3.2. The raw data that is the output of the detector readout electronics or the output of the third stage of the simulation consists of hits on wires and energy deposits in crystals and is essentially unusable for physics analyses. Before it can be used, it needs to be processed. As an example, the hits in the drift chamber have to be fitted to tracks, the energy deposits in crystals have to be analyzed to figure out how many particles of what energy caused them and the signals from the other detector components have to be processed in similar ways. This step could be done offline, ie. after the data from the detector is recorded on permanent storage. CLEO is using this approach. In BaBar, we do this online, which means we process the data in real time, keeping up with the data collected by the detector.

Since the simulation mirrors data taking, we also run the reconstruction code on the simulated events before writing them to permanent storage.

5.4 How much MC do we need ?

Because of the statistical nature of the processes involved, we need at the very least the same number of simulated events then what we expect to be in the data, more is even better. For the signal decay modes this is usually not a problem since many of the most interesting modes are rare and therefore we don't expect many events in the data sample. But the background simulation causes a problem. Basically every event in the whole data sample that doesn't contain our signal mode decay is background, so for all intent and purpose we need to simulate at least as many background events as there are real data events.

With this in mind, once an analysis defines what signal modes they need to look at, they will determine how many signal events they expect in the data and then request at least a similar set of simulated signal event or better yet, a multiple of that. As for background MC, this is produced not specific for each analysis, but as a common MC set for all analysis to use. This common set of MC contains a mix of all possible decay modes (that we know about and can simulate) with the correct (as we know it) branching fractions. This also means that for some analyses, the background MC will contain signal events, making the name background MC incorrect. We will call this common MC set generic MC from now on.

5.4.1 How many resources do we need for MC ?

Looking at the resources (cpu time) required for event simulation makes clear why having a common set of generic MC events for all analyses is the only reasonable (and possible) approach. A simulated e^+e^- collision at the $\Upsilon(4S)$ resonance that produces a $b\bar{b}$ quark pair which then fragments into a pair of B mesons takes a few seconds to simulate. The current total data set collected at BaBar contains about 250 Million such $e^+e^- \to B\bar{B}$ events. Assuming 5 seconds for each event (which is an optimistic number, all except the fastest available PCs would need longer than that), one PC would have to spend a total time of close to 40 year to simulate all these events. And this is not even all the generic MC events we have to simulate, since the e^+e^- collision could also pair produce a $q\bar{q}$ quark pair with a lighter quark (u,d,s or c) or a l^+l^- lepton anti-lepton pair (electron, muon or tau). Obviously, we cannot wait 40 years for the simulated events. Simulation has to keep up with data taking to be useful for analyses. Fortunately, each event is independent from all other events. We can just split the required number of events into smaller subsets and distribute the simulation over multiple computers. If one computer needs 40 years to finish the task, 1000 computer will only need about 15 days.

5.4.2 Summary of BaBar MC needs

We want at least as many MC events of a specific decay mode as are to be found in real data. More would be even better, resulting in smaller statistical uncertainties for the analyses. On the other hand, MC simulation and especially the simulation of generic MC events needs a huge amount of resources, resources that are also needed for the operation of the detector, the handling of the huge data sets (both MC and data) and for data analyses. Since the study of B mesons is one of the primary physics goals of BaBar and therefore priority is given to analyses that study B meson decays, we produce three times the luminosity equivalent sample of generic B meson events. For the other generic events (lighter quark pairs, lepton pairs) we would really want to do the same, but we just don't have the resources to do so, especially since the added cross sections for production of u, d, s or c quark pairs is ~ 3.4 nb compared to a cross section of ~ 1.1 nb for b quark pair production. That means in any given set of real data, there are approximately three times as many light quark pairs as b quark pairs.

Table 5.1 lists the cross section for the production of generic uds (pair of u, d or s quark), ccbar (pair of c quarks) and BBbar (pair of b quarks fragmenting into B mesons). The number of events is based on these cross sections and a data sample of 220 fb^{-1}, which is approximately the whole current data sample collected in the first four run cycles. The new run cycle that started in April of 2005 is not included. Also in the table are $\tau^+\tau^-$ and $\mu^+\mu^-$ lepton pair production.

Type	Cross section in nb	# Events in data	# Simulated events needed
BBbar	1.1	242 Million	726 Million
ccbar	1.30	286 Million	286 Million
uds	2.09	460 Million	460 Million
tau	0.89	196 Million	196 Million
muon	1.15	253 Million	253 Million

Table 5.1: Number of generic events in 220 fb^{-1} of data and equivalent simulated events.

5.4.3 Detector dependence of MC

From the description of the four-stage simulation model in Section 5.3 it is clear that the simulation is heavily dependent on certain assumptions we make about the detector.

The second stage depends on the mechanical makeup of the detector, the precise location of all components and what materials they are made from. Every time the detector is mechanically disturbed, like when we open it up to work on a subdetector, the location of everything in the detector changes.

In the third stage, how we simulate the electric and electronic systems determines how the interactions by the particles passing through the detectors are translated into signals that represent output from the readout electronics.

The reconstruction code does basically the same thing as the third and second stage, just backward. It's taking the (in this case simulated) signals that come from the detector readout electronics and tries to go all the way back and determine the particles that produced these signals. Therefore the reconstruction depends on both the condition of the electric and electronic systems and the mechanical makeup of the detector.

What this all means is that we cannot simulate an event without picking a certain point in time for which that simulation is valid. Since the ultimate goal of the whole MC production effort is to provide simulated events that resemble data as best as possible, we have to produce MC events for a multitude of detector configurations to reach that goal.

Now, something always changes, especially the conditions of the electric and electronic systems. But from a management perspective it's not feasible to keep track of changing conditions on a very small time scale. What we do in BaBar is to create average conditions for each month and we store them in the 'Configurations and Conditions" database.

Then we produce simulated events for each of these monthly conditions. How much MC we produce for each month depends on how much data was collected during the month. Again, the MC events should resemble data as best as possible, therefore we try to have a mix of MC events with different monthly conditions that is in the same proportion as the mix of data collected during these months.

5.5 BaBar MC Production Cycles

BaBar has been running and taking data since 2000. Since Monte Carlo events are required for data analysis, it also has been producing them for at least this long.

But the software used by BaBar for data taking has not remained what it was when first data was collected in 2000. Specifically, the reconstruction code was improved as the understanding of the detector changed over time.

Data analysis relies on a consistent data sample. If there are major differences in the reconstruction code used for different data samples, we can no longer use these data samples together in a single analysis. Since we want to use as much data as possible in the analysis to keep the statistical uncertainties to a minimum but on the other hand also want to benefit from improvements in the reconstruction code, we have to rerun the reconstruction code over all the old data every time there is a major reconstruction code change.

In principle we could do the same for MC. But for MC it's not only the reconstruction code that changes. The code that generates the simulated events in the first place changes too. It's even worse, since the understanding of the physics that determines how we do the simulation also changes. New measurements change what we know about particles, new particles are discovered and theoretical models evolve. All of this has to be integrated into the simulation code. Another issue is that running the reconstruction code is one of the most time consuming parts of the whole event simulation chain. Even if we would reprocess the old MC and just rerun the reconstruction code, it wouldn't save us a huge amount of time compared to simulating complete new events. For all these reasons MC is not reprocessed, but we instead produce a complete new set of simulated events.

Every major change in the reconstruction software triggers a reprocessing cycle of the old data and a new MC production cycle. If one wants to use the new data or the reprocessed data for analysis, one also has to use the MC from the new MC production cycle. The old MC from the previous cycle can only be used for analysis of the old data (before reprocessing). The MC production cycles are called SP<number>. SP stands for "Simulation Production" and number is just a counter. In April of 2005 BaBar has started a new data taking period with a major new release of the data taking software that also contains a new version of the reconstruction code. In parallel BaBar is in the process of starting a new MC production cycle, SP8.

See Appendix C for a description of the last three SP cycles and a more detailed description of the production procedures in the current SP8 cycle.

5.6 Distributed MC production

All the BaBar MC events used in analyses are produced by a BaBar computing subgroup, the SP group. The head of this group is named SP coordinator. I have been holding this position since November of 2004. Basically I am responsible to get all Monte Carlo events BaBar needs produced, both the generic MC sample and also simulated events individual users need specifically for their analysis.

I am responsible to keep the Monte Carlo production running. That means I have to interact with the SP sites (more on this below), help them sort out problems, but also tell them what types of events and how many of them to simulate. I also interact with the users that do an analysis. They tell me what type of Monte Carlo they need and I make sure it is getting produced in a timely manner. Other duties are administrative, I have to interact with BaBar computing management, tell them what the status of SP is, what we can and cannot do.

At first MC events were exclusively been produced at SLAC. With an increasing amount of data and therefore a need for more and more MC events, the resource demands made it necessary to distribute the MC production effort over multiple sites. The last SP cycle exclusively produced at SLAC was SP3, all later cycles, starting with SP4, have been produced at SLAC and other sites. Over time, the amount of MC production at SLAC has continuously decreased, for SP6 it was less then 3% of all the produced MC events.

There are about 20 sites currently participating in the SP8 MC production. These sites can be very different. Some are university groups that maintain their own computer farms (similar to the computer farm here at OSU). Some are bigger computing centers which have a certain percentage of their resources allocated for BaBar.

CHAPTER 6

Theory, Motivation and Introduction for Analysis

The previous chapters discussed the detector, the detector operation and additional software like reconstruction and simulation. Now that we have the collected data and the output of the reconstruction code run over it on permanent storage, we want to analyze this data sample. We also have available a sample of simulated events and these events too have been processed with the reconstruction code.

In the following chapters I will describe work I did using the BaBar data sample (exact composition listed in Section 6.6). It involves the study of charmed mesons, in particular D^+ mesons which contain a c quark and a $\bar{d}$ anti-quark. As the lightest charmed mesons, the D mesons are a good system to study weak decays since there are no strong decays that would mask the weak decays. In the data analysis presented here I will search for two decay modes, $D^+ \to \pi^+\pi^0$ and $D^+ \to K^+\pi^0$. The π^+ meson is a bound state of a u quark and $\bar{d}$ anti-quark, the K^+ is a bound state of a u quark and $\bar{s}$ anti-quark and the π^0 is a linear combination of $u\bar{u}$ and $d\bar{d}$ bound states. The first mode is singly Cabibbo-suppressed (SCS), which just means it contains one Cabibbo-suppressed quark transitions (see Section 1.4). The second mode is doubly Cabibbo-suppressed (DCS), containing two Cabibbo-suppressed quark transitions.

6.1 Decay Diagrams

Since both $D^+ \to \pi^+\pi^0$ and $D^+ \to K^+\pi^0$ are weak decays that involve quark transitions, they are propagated through a W boson. Following are the dominant first order Feynman diagrams for $D^+ \to \pi^+\pi^0$ and $D^+ \to K^+\pi^0$. The Cabibbo-favored decay (CFD) $D^+ \to K^0\pi^+$ is also shown for comparison.

- $D^+ \to \pi^+\pi^0$

(a)

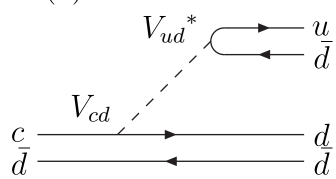

- $D^+ \to K^+\pi^0$

(b)

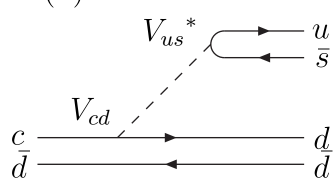

- $D^+ \to K^0\pi^+$

(c)

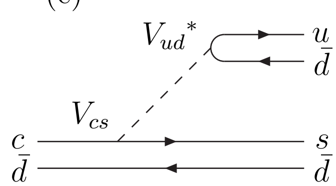

Each diagram can be associated with a decay *amplitude* A. The decay width Γ ($\Gamma = \frac{1}{\tau}$ where τ is the lifetime) of a given decay mode is proportional to the square of the decay amplitude or the square of the sum of decay amplitudes if multiple diagrams contribute to a decay. This is also where the CKM matrix elements come into play. For each quark transitions in the Feynman diagram, the corresponding matrix element factors into the amplitude. In diagram (a) for instance we have two weak vertexes, one with charm and down quarks and another with up and down quarks. For these vertexes the CKM matrix elements $V_{cd} = 0.221$ and $V_{ud} = 0.9739$ come into play, one of which is small, hence the Cabibbo-suppressed decay mode. For diagram (b) the two matrix elements are $V_{cd} = 0.221$ and $V_{us} = 0.221$, both of which are small, hence the doubly Cabibbo-suppressed decay mode. In the Cabibbo-favored decay shown in diagram (c) the matrix elements are $V_{cs} = 0.973$ and $V_{ud} = 0.9739$, both of which are almost equals to 1, hence no Cabibbo-suppression.

6.2 Effect on $D^0 - \bar{D}^0$ Mixing

Assuming the spectator model is correct, our search for $D^+ \to K^+\pi^0$ would be very important to $D^0 - \bar{D}^0$ mixing measurements. Such measurements use interference terms from the Cabibbo-favored decay (CFD) $D^0 \to \bar{D}^0 \to K^+\pi^-$ and the DCSD $D^0 \to K^+\pi^-$, whose only difference to the charged DCSD $D^+ \to K^+\pi^0$ is in the spectator $\bar{u}$ instead of $\bar{d}$. Since mixing doesn't apply for the D^+ decay, we would be able to measure the DSCD contribution in the D^+ decay and apply it the $D^0 - \bar{D}^0$ mixing study. In practice a problem arises because final state interactions (rescattering) play a significant role for D decays. Even though that means the predictions of the spectator model can be highly skewed, understanding of the DCSD decay modes can still help to improve the $D^0 - \bar{D}^0$ mixing measurements.

6.3 SU(3) Flavor Symmetry

From a historic perspective, the introduction of SU(3) Flavor symmetry (or $SU(3)_F$) coincides with the introduction of quarks [5]. $SU(3)_F$ considers the three lightest quarks, up, down and strange to be identical particles as far as the strong force is considered. Under this assumption, in strong interactions these three quarks should be interchangeable with each other. Experimental evidence shows this is only approximately correct. The reason for this "breaking" of the symmetry is the mass of the s quark, which is significantly larger than that of the up and down quark. It is still possible to extract useful physical predictions from this approximate symmetry, assuming the level of symmetry breaking is small and well understood. Current predictions based on $SU(3)_F$ are accurate to about 30 % [19].

The size of $SU(3)_F$ symmetry breaking is also of interest for $D^0 - \bar{D}^0$ mixing studies. The mass and width differences (x,y) in the CP-eigenstates of the D^0 are dependent on the $SU(3)_F$ symmetry breaking [20]. If x and y are experimentally found to be non-zero, a very good theoretical Standard Model prediction of x and z is necessary to introduce the possibility for new physics beyond the Standard Model. This is only possible if the size of the $SU(3)_F$ symmetry breaking is well known.

6.4 Decay Rates and Branching Fractions

When I say that in our analysis we are searching for the decays $D^+ \to \pi^+\pi^0$ and $D^+ \to K^+\pi^0$, what I really mean is that we want to determine the branching fractions of these two decay modes. The branching fraction for a mode i is defined as

$$BF(i) = \frac{N_{decays}(i)}{N_{decays}} \tag{6.1}$$

or in terms of the decay widths introduced in Section 6.1

$$BF(i) = \frac{\Gamma(i)}{\Gamma} \tag{6.2}$$

The current world average [6] for the branching fraction of $D^+ \to \pi^+\pi^0$ is

$$BF(D^+ \to \pi^+\pi^0) = (2.6 \pm 0.7) \times 10^{-3} \tag{6.3}$$

The $D^+ \to K^+\pi^0$ decay mode has not been observed yet and until last year not even an upper limit had been published. In 2004 CLEO published [27] a result for $D^+ \to \pi^+\pi^0$ that is significantly different from the world average and an upper limit for $D^+ \to K^+\pi^0$

$$BF(D^+ \to \pi^+\pi^0) = (1.31 \pm 0.17 \pm 0.09 \pm 0.09) \times 10^{-3} \tag{6.4}$$

$$BF(D^+ \to K^+\pi^0) < 4.2 \times 10^{-4} \text{ at } 90\ \%\ \text{CL} \tag{6.5}$$

In this analysis we will try to improve the $D^+ \to \pi^+\pi^0$ measurement and provide a first observation of $D^+ \to K^+\pi^0$.

6.5 Branching Fraction Measurement

The equation we use in our analysis to calculate branching fractions is :

$$BF(D^+ \to \pi^+\pi^0) = \frac{N(D^+ \to \pi^+\pi^0)}{N(D^+)} \tag{6.6}$$

To calculate this branching fraction, we would have to know the total number of D^+ mesons in our data sample and we also would have to know how many of them decayed to the modes we are interested in.

As already mentioned in Subsection 2.3.2, to be able to find the decay modes we are looking for, we have to apply cuts on the data that help us to separate signal from background by cutting out more background than signal events. The problem is that after we apply the cuts, the number of $D^+ \to \pi^+\pi^0$ events we count in the data sample is no longer equal to the total number of $D^+ \to \pi^+\pi^0$ events N_{total}, the cuts will have removed some of them. To account for this, we can rewrite equation 6.6 as

$$BF(D^+ \to \pi^+\pi^0) = \frac{N_{fit}(D^+ \to \pi^+\pi^0)}{N(D^+)} \times \frac{N_{total}(D^+ \to \pi^+\pi^0)}{N_{fit}(D^+ \to \pi^+\pi^0)} \tag{6.7}$$

where N_{fit} is the number of events found in the data sample after all cuts are applied and the data is fitted to extract event yields. With the ratio $\frac{N_{fit}(D^+ \to \pi^+\pi^0)}{N_{total}(D^+ \to \pi^+\pi^0)}$ defined as reconstruction efficiency $\epsilon_{D^+ \to \pi^+\pi^0}$, we can rewrite equation 6.7

$$BF(D^+ \to \pi^+\pi^0) = \frac{N_{fit}(D^+ \to \pi^+\pi^0)}{\epsilon_{D^+ \to \pi^+\pi^0} \cdot N(D^+)} \tag{6.8}$$

For our analysis we determine the value of $\epsilon_{D^+ \to \pi^+\pi^0}$ from a sample of simulated events on which the same cuts as on data are applied.

To complete the branching fraction calculation as shown in equation 6.8, we need to know the total number of D^+ mesons in our data sample. This number can in principle be calculated using luminosity and cross section measurements, but it would suffer from large systematic errors due to uncertainties in the D^+ production mechanism. Instead, the branching fractions are measured relative to the high statistics, well measured, $D^+ \to K^-\pi^+\pi^+$ reference decay mode. By applying equation 6.8 to both $D^+ \to \pi^+\pi^0$ and $D^+ \to K^-\pi^+\pi^+$ and combining the two resulting equations, we get the final equation we use to extract our signal mode branching fractions from data

$$BF(D^+ \to \pi^+\pi^0) = \frac{N_{fit}(D^+ \to \pi^+\pi^0) \cdot \epsilon_{D^+ \to K^-\pi^+\pi^+}}{N_{fit}(D^+ \to K^-\pi^+\pi^+) \cdot \epsilon_{D^+ \to \pi^+\pi^0}} \times BF(D^+ \to K^-\pi^+\pi^+) \tag{6.9}$$

with $BF(D^+ \rightarrow K^-\pi^+\pi^+)$ being the well measured branching fraction for mode $D^+ \rightarrow K^-\pi^+\pi^+$ as listed in [6]. Using this approach means we don't need to know the total number of D^+ in our data sample since that number cancels out. The downside to this approach is that we have to do two analyses looking for two separate decay modes $D^+ \rightarrow \pi^+\pi^0$ and $D^+ \rightarrow K^-\pi^+\pi^+$.

6.6 Data and MC Samples used for Analysis

The data in this analysis was collected between 1999 and 2003 with the BaBar detector at the PEP-II asymmetric e^+e^- storage ring. The total integrated luminosity of the data sample is about 124.3 fb^{-1} (corresponding to about 162 Million $c\bar{c}$ events). Most of the data was collected on the the $\Upsilon(4S)$ resonance at the center-of-mass energy $\sqrt{s} = 10.58$ GeV, but a small subset of the data was collected approximately 40 MeV below the resonance.

Table 6.1 shows the size of the Monte Carlo samples used for this analysis. All candidate selection efficiencies are extracted from the high statistic signal Monte Carlo samples. The background samples were only used for fit development and validation, but not for the extraction of the event yields from data.

Mode	# of events	$\mathcal{L}$ (fb^{-1})
$D^{*+} \to D^+\pi^0_{Soft}$ $\quad ,D^+ \to K^+\pi^0$	120000	-
$D^{*+} \to D^+\pi^0_{Soft}$ $\quad ,D^+ \to \pi^+\pi^0$	120000	-
$D^{*+} \to D^+\pi^0_{Soft}$ $\quad ,D^+ \to K^-\pi^+\pi^+$	700000	-
$e^+e^- \to c\bar{c}$	$128 \cdot 10^6$	94
$e^+e^- \to u\bar{u}, d\bar{d}, s\bar{s}$	$144 \cdot 10^6$	68
$e^+e^- \to B^+\bar{B}^-$	$52 \cdot 10^6$	95
$e^+e^- \to B^0\bar{B}^0$	$41 \cdot 10^6$	75
Run 1 Data On-Peak(1999-2000)	$286.2 \cdot 10^6$	19.4
Run 2 Data On-Peak (2001-2002)	$891.4 \cdot 10^6$	60.2
Run 3 Data On-Peak (2003)	$446.3 \cdot 10^6$	31.1
Run 1 Data Off-Peak(1999-2000)	$27.4 \cdot 10^6$	2.3
Run 2 Data Off-Peak (2001-2002)	$80.4 \cdot 10^6$	6.9
Run 3 Data Off-Peak (2003)	$23.6 \cdot 10^6$	2.4

Table 6.1: Monte Carlo and Data samples used in the analysis. The second column shows the number of events entering the reconstruction, the third the luminosity of each sample.

CHAPTER 7

Event Reconstruction

The huge data sample BaBar has accumulated over years of running allows us to measure even rare decay modes with relatively low statistical uncertainties. But due to the sheer number of events that need to be processed, this data sample also provides a challenge. For a data analysis we want to process every event to minimize the statistical uncertainties of our results.

We need to find selection criteria that select events that contain the decay modes we are interested in while rejecting events that don't. In practice, most selection criteria will reject some fraction of both types of events.

7.1 Event Selection

The first requirement in our event selection was that an event had to have at least three charged tracks. While the reference mode $D^+ \to K^-\pi^+\pi^+$ contains three charged tracks, the signal modes $D^+ \to \pi^+\pi^0$ and $D^+ \to K^+\pi^0$ only contain one charged track. But D^+ are only produced in hadronic events, where the e^+e^- collision initially produced a quark anti-quark pair. There is a high probability that these hadronic events will at least have two more charged tracks. Table 7.1 shows the result of applying this selection criteria to various Monte Carlo samples and to

Type	event accepted
$D^+ \to K^+\pi^0$	91.6 %
$D^+ \to \pi^+\pi^0$	91.4 %
$D^+ \to K^-\pi^+\pi^+$	93.5 %
$c\bar{c}$	93.5 %
uds	90.2 %
B^0B^0	99.1 %
B^+B^-	99.2 %
$Data$	42.3 %

Table 7.1: Effect of requiring three charged tracks. No further cuts are applied on the event level of the analysis. The cut was necessary to limit the amount of data which is processed even if it is not completely optimal for the signal.

data. As you can see, even though close to 10 % of the signal and reference mode events are rejected, more then half the data sample is rejected.

Let me just say at the beginning that unless explicitly stated, charge conjugation is implied. For instance, if I talk about $D^+ \to \pi^+\pi^0$, the charge conjugated mode $D^- \to \pi^-\pi^0$ is always included unless stated otherwise.

For the measurement of the $D^+ \to \pi^+\pi^0$ and $D^+ \to K^+\pi^0$ branching fractions, D^+ candidates were reconstructed by combining a charged track with a π^0 candidate. The charged track was assigned a pion hypothesis in the $D^+ \to \pi^+\pi^0$ case and a kaon hypothesis in the $D^+ \to K^+\pi^0$ case. As stated in the previous chapter, the branching fractions are measured relative to the high statistics, well measured, $D^+ \to K^-\pi^+\pi^+$ reference decay mode.

In order to reduce the large amount of combinatoric background in the D^+ signal modes, the decay chain is extended to reconstruct only D^+ decays that originate from D^{*+} mesons in the mode $D^{*+} \to D^+\pi^0$. This is done for both the signal and reference channels to minimize systematic contributions from the π^0 (they cancel out in the branching fraction ratio).

The following subsections provide detailed descriptions of the charged track and neutral particle definitions, the event selection, the reconstruction of the signal and reference D^+ modes and the reconstruction of the $D^{*+} \to D^+\pi^0$.

7.1.1 Charged track and π^0 selection

After the reconstruction, there are lists available that are filled with particle candidates 4-vectors. We now use these lists for the data analysis, but to suppress background events in favor of signal events, we apply certain selection criteria to these lists.

Before I go into the details of the charged track and π^0 selection, I want to mention a detail about the momentum of a particle. Since BaBar is an asymmetric detector, the momentum of a particle in the lab frame (the frame the detector is in) and the CMS frame (the center-of-mass frame of the collision) are not identical. Unless otherwise specified, all momenta I mention are in the lab frame. Exception to this are normalized momenta (defined below) which are by definition only valid in the CMS frame.

Charged tracks have to meet certain requirement in order to be included in the candidate reconstruction to insure that only well measured tracks are used. These requirements are :

- Minimal transverse momentum of 0.1 GeV.
- Maximum momentum of 10 GeV.
- A minimum of 12 hits in the drift chamber.

- The Kalman track fit has to be successful.
- The distance of closest approach to the beamspot in the x-y plane (DOCAXY) has to be smaller than 1.5 cm.
- The DOCA in z-direction has to be smaller than 10 cm.

Separate π^0 lists were used for the two types of π^0 candidates from the D^+ and D^{*+} to take into account the difference in their momentum distribution. The π^0_{soft} from the D^{*+} decay has a much smaller maximum momentum due to the relativly small mass difference Δm between the D^{*+} and D^+.

A list of soft π^0_{soft} candidates is formed from two photon combinations that satisfy these requirements :

- The minimum photon energy is 30 MeV and the lateral moment of the EMC cluster is between 0.0 and 0.8.
- The π^0 candidate mass has to be between 0.115 GeV and 0.15 GeV.
- The 2 photons are combined to a π^0 candidate using a mass constrained fit.
- The π^0 candidate CMS momentum has to be less than 0.45 GeV.

Another list of π^0 candidates is defined as the combined list of π^0's reconstructed from merged π^0 candidates derived from a single EMC cluster and two photon combinations with the following criteria :

- The minimum photon energy is 30 MeV and the lateral moment of the EMC cluster is between 0.0 and 0.8.
- The π^0 candidate mass has to be between 0.115 GeV and 0.15 GeV.

- The 2 photons are combined to a π^0 candidate using a mass constrained fit.
- The π^0 candidate momentum has to be greater than 0.2 GeV.

7.1.2 $D^+ \to K^+\pi^0$ and $D^+ \to \pi^+\pi^0$ reconstruction

The D^+ signal modes are reconstructed by combining a charged track with a π^0 candidate. A pion hypothesis is assumed for the charged track in the $D^+ \to \pi^+\pi^0$ case and a kaon hypothesis in the $D^+ \to K^+\pi^0$ case. The mass of the π^0 candidate is constraint to it's nominal value [6]. A successfully reconstructed D^+ candidate satisfies the following criteria :

- The invariant mass of the D^+ candidate is between 1.7 GeV and 2.0 GeV.
- The D^+ vertex fit is successful.
- The absolute of the cosine of the pion or kaon helicity $\Theta_{Helicity}$ (definition follows below) has to be less than 0.9. This is done to reduce combinatorial background, which peaks at ± 1, while the signal is expected to be flat. The pion helicity in the decay chain $D^{*+} \to D^+\pi^0_{soft}$, $D^+ \to \pi^+\pi^0$ is defined as the angle between the flight direction of the D^{*+} and the π^+ in the rest frame of the D^+. The kaon helicity is defined in the same way for the other signal decay mode.

7.1.3 $D^+ \to K^-\pi^+\pi^+$ reconstruction

The reconstruction of the reference mode is very similar to the signal modes, with the biggest difference that there is no π^0 in this D^+ decay. A kaon candidate (assuming kaon hypothesis) and two pion candidates (assuming pion hypotheses) are combined to form a $D^+ \to K^-\pi^+\pi^+$ candidate. The following requirements are imposed :

- The invariant mass of the D^+ candidate is between 1.75 GeV and 1.95 GeV.
- The three charged tracks need to form a common vertex and the D^+ vertex fit is successfully.
- The absolute of the cosine of the kaon helicity $\Theta_{Helicity}$ (definition follows below) has to be less than 0.9. This is a three-body decay, so this cut doesn't remove as much background as for the signal modes, but it still is useful.

7.1.4 $D^{*+} \to D^+\pi^0_{soft}$ reconstruction

The reconstruction of the $D^{*+} \to D^+\pi^0_{soft}$ chain is identical for the signal and reference modes. A soft π^0 candidate is combined with a D^+ candidate to form a D^{*+} candidate. A successful reconstructed D^{*+} candidate satisfies the following criteria :

- The mass difference Δm between the D^{*+} and D^+ has to be between 0.12 GeV and 0.155 GeV.
- The vertex fit, which had a beamspot constraint applied to the D^{*+} origin, had to be successfully.
- The normalized momentum $x_{D^{*+}}$ of the D^{*+} candidate has to be greater 0.4. The normalized momentum $x_{D^{*+}}$ is defined as follows

$$x_{D^{*+}} = \frac{|\vec{p}^{\,CMS}_{D^{*+}}|}{\sqrt{s/4 - m^2_{D^{*+}}}} \quad \text{with} \quad s = {E_{collision}}^2 \tag{7.1}$$

Mode	total # of events	# of candidates	fraction (%)
$D^{*+} \to D^+\pi^0_{soft},\ D^+ \to \pi^+\pi^0$	115000	42670	37.1
$D^{*+} \to D^+\pi^0_{soft},\ D^+ \to K^+\pi^0$	119000	43817	38.8
$D^{*+} \to D^+\pi^0_{soft},\ D^+ \to K^-\pi^+\pi^+$	700000	360709	51.5

Table 7.2: The table shows the selection efficiencies after the initial candidate reconstruction for signal events in the individual modes for signal Monte Carlo.

A breakdown of the selection efficiencies for the different D^+ modes after the initial candidate reconstruction is given in table 7.2. The efficiency is defined as the number of reconstructed D^{*+} candidates over the total number of generated events in the sample. The reconstruction is not limited to one candidate per event and it happens quite often that more than one is found due to the huge combinatorics from the soft π^0 list. The mean number of $D^+ \to K^+\pi^0$ candidates relative to the number of events with at least one candidate based on signal Monte Carlo is 1.7 (1.6 for $D^+ \to \pi^+\pi^0$).

7.2 Candidate Selection

In order to reduce the contributions from background a more stringent candidate selection is applied following the initial reconstruction step. These selections are slightly different for the signal $D^+ \to \pi^+\pi^0$ and $D^+ \to K^+\pi^0$ modes and the $D^+ \to K^-\pi^+\pi^+$ reference mode.

The optimal cuts where found by applying the full fit analysis (see Chapter 8) on Monte Carlo samples with signal and background events. The dependence of the signal significance on the discriminating variables $\Theta_{Helicity}$ and $x_{D^{*+}}$ is relative weak. The cuts on $D^+ \to K^-\pi^+\pi^+$ are chosen to resemble the signal mode cuts as close

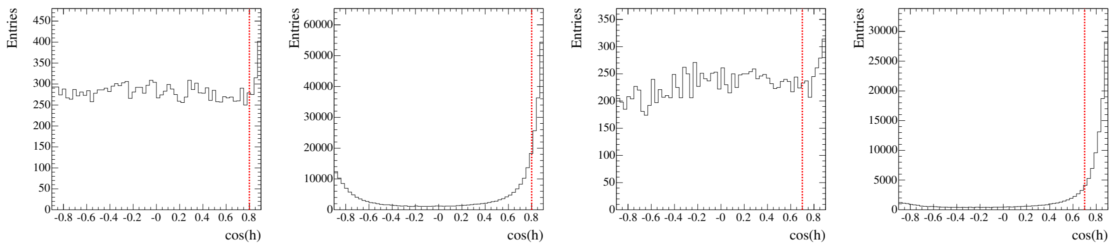

Figure 7.1: The cosine of the helicity distributions for the $D^+ \to \pi^+\pi^0$ mode (two left plots) and $D^+ \to K^+\pi^0$ mode (two right plots). In each case the left of the two plots is for signal Monte Carlo while the right is for a subset of the data.

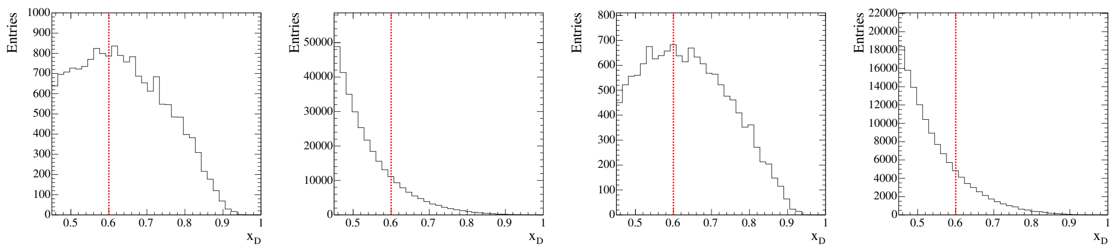

Figure 7.2: The normalized momentum distributions for the $D^+ \to \pi^+\pi^0$ mode (two left plots) and $D^+ \to K^+\pi^0$ mode (two right plots). In each case the left of the two plots is for signal Monte Carlo while the right is for a subset of the data.

as possible to minimize systematic contributions. Figure 7.1 and figure 7.2 show the cosine of the helicity distribution and the normalized momentum distribution for $D^+ \to \pi^+\pi^0$ and $D^+ \to K^+\pi^0$ signal Monte Carlo and a subset of the data.

Table 7.3 lists the results of the cut optimization. Derived from these numbers the following selection criteria were chosen for the signal modes :

$\cos(\Theta_{Helicity})$ cut	$x_{D^{*+}}$ cut	event yield	relative error
Cuts for $D^+ \to \pi^+\pi^0$			
< 0.9	> 0.5	1238 ± 100	8.1 %
< 0.9	> 0.6	999 ± 71	7.2 %
< 0.9	> 0.7	605 ± 43	7.2 %
< 0.8	> 0.5	1203 ± 93	7.7 %
< 0.8	> 0.6	934 ± 53	5.6 %
< 0.8	> 0.7	563 ± 36	6.5 %
< 0.7	> 0.5	1163 ± 82	7.1 %
< 0.7	> 0.6	844 ± 60	6.7 %
< 0.7	> 0.7	543 ± 34	6.3 %
Cuts for $D^+ \to K^+\pi^0$			
< 0.9	> 0.5	243 ± 71	29 %
< 0.9	> 0.6	150 ± 47	31 %
< 0.9	> 0.7	90 ± 20	29 %
< 0.8	> 0.5	218 ± 53	24 %
< 0.8	> 0.6	163 ± 36	22 %
< 0.8	> 0.7	95 ± 21	22 %
< 0.7	> 0.5	197 ± 45	23 %
< 0.7	> 0.6	160 ± 31	19 %
< 0.7	> 0.7	98 ± 19	19 %
< 0.6	> 0.5	192 ± 42	21 %
< 0.6	> 0.6	159 ± 31	20 %
< 0.6	> 0.7	91 ± 18	20 %

Table 7.3: Results of the cut optimization derived from the Maximum Likelihood fit described in detail later in this note.

- The invariant mass of the D^+ candidate is between 1.7 GeV and 2.0 GeV. The mass window is relatively wide as the invariant mass is later used in the Maximum Likelihood fit.
- The normalized momentum $x_{D^{*+}}$ of the D^{*+} candidate has to be greater than 0.6.

- The cosine of the helicity $\Theta_{Helicity}$ has to be less than 0.8 in the $D^+ \to \pi^+\pi^0$ mode and less than 0.7 in the $D^+ \to K^+\pi^0$ mode.

- Particle identification is applied to the kaon candidate in $D^+ \to K^+\pi^0$ and the pion candidate in $D^+ \to \pi^+\pi^0$. See Subsection 7.2.1 for details.

The reference mode has the following selection criteria applied :

- The invariant mass of the D^+ candidate is between 1.78 GeV and 1.95 GeV. The mass window is chosen narrower because of the slightly better D^+ mass resolution in the reference mode.

- The normalized momentum $x_{D^{*+}}$ of the D^{*+} candidate is greater than 0.6.

- The cosine of the helicity $\Theta_{Helicity}$ has to be less than 0.8 (if we wanted to measure the branching fraction ratio for $D^+ \to \pi^+\pi^0$) or less than 0.7 (to measure the branching fraction ratio for $D^+ \to K^+\pi^0$).

- Particle identification is applied to the kaon candidate. See Subsection 7.2.1 for details.

- No particle identification is applied to the pion candidates.

Figure 7.3 shows the momentum spectrum for signal and background Monte Carlo. A separation between the signal momentum spectrum and the background is visible. A cut on the slow π^0_{soft} momentum was required in order to reduce combinatoric background.

The D^{*+} has to satisfy the following criteria for signal and reference modes :

- The mass difference Δm is between 0.132 GeV and 0.155 GeV.

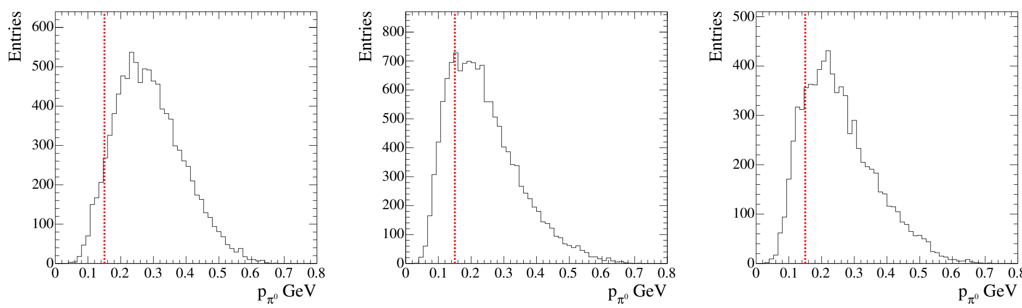

Figure 7.3: The three plots illustrate the momentum distribution of the π^0_{soft}. The left plot shows $D^+ \to \pi^+\pi^0$ signal , center plot shows uds generic and right plot shows $c\bar{c}$ generic Monte Carlo.

Sample	$\epsilon(D^+ \to \pi^+\pi^0)$	$\epsilon(D^+ \to K^+\pi^0)$	$\epsilon(D^+ \to K^-\pi^+\pi^+)$
$D^+ \to \pi^+\pi^0$	0.0777 ± 0.0008	-	-
$D^+ \to K^+\pi^0$	-	0.0593 ± 0.0007	-
$D^+ \to K^-\pi^+\pi^+$	-	-	$(0.0778/0.0739 \pm 0.0003$

Table 7.4: The table shows the selection efficiencies for the $D^+ \to \pi^+\pi^0$ and $D^+ \to K^+\pi^0$ signal and $D^+ \to K^-\pi^+\pi^+$ reference modes. The two different numbers for the $D^+ \to K^-\pi^+\pi^+$ mode result from the different $cos(\Theta_{Helicity})$ cuts used. The given errors are statistical only from the limited Monte Carlo statistics.

- The soft π^0_{soft} candidate mass has to be between 0.12 GeV and 0.148 GeV.
- The soft π^0_{soft} momentum has to be greater than 150 MeV.

In the case of multiple candidates in an event the candidate with the highest D^{*+} momentum in the CMS frame is chosen, the other candidates are discarded. The resulting efficiencies of the candidate selection is shown in Table 7.4.

Figure 7.4 shows the D^+ and Δm distributions for signal Monte Carlo in the individual modes after the candidate selection.

7.2.1 PID Optimizations

Additional particle identification criteria are applied to the kaon in $D^+ \to K^-\pi^+\pi^+$ and $D^+ \to K^+\pi^0$ and the pion in $D^+ \to \pi^+\pi^0$. We used a cut based analysis based on Monte Carlo events to evaluate and select the most optimal PID selection criteria. As a result of these studies, a decision was made to use maximum likelihood based selectors.. The idea behind these selectors is that for each particle hypothesis separate likelihoods are calculated for the Silicon Vertex Tracker, the Drift Chamber and the Cherenkov Detector and then combined into a global likelihood

$$\mathcal{L}_i = \mathcal{L}_i^{Silicon} \times \mathcal{L}_i^{Drift} \times \mathcal{L}_i^{Cherenkov} \tag{7.2}$$

with $i = K, \pi, p$ (kaon, pion, proton).

The Silicon Vertex and Drift Chamber likelihoods are calculated from how well the measured rate of energy loss $\frac{dE}{dx}$ matches the expected $\frac{dE}{dx}$. The Cherenkov likelihood comes from a lookup table binned in Cherenkov angle, number of photons and track quality. For a more detailed description see [23].

The pion in $D^+ \to \pi^+\pi^0$ has to satisfy :

- $\frac{\mathcal{L}_K}{\mathcal{L}_K+\mathcal{L}_\pi} < 0.98$
- $\frac{\mathcal{L}_p}{\mathcal{L}_p+\mathcal{L}_\pi} < 0.98$

The kaon in $D^+ \to K^+\pi^0$ has to satisfy :

- $\frac{\mathcal{L}_K}{\mathcal{L}_K+\mathcal{L}_\pi} > 0.9$
- $\frac{\mathcal{L}_K}{\mathcal{L}_K+\mathcal{L}_p} > 0.2$

- Doesn't meet *eLHTight* requirements, which are defined in [24]. This prevents us from identifying a track as kaon if it also satisfies electron particle identification criteria.

- Doesn't meet *μMicroTight* requirements, which are defined in [25] [26]. This prevents us from identifying a track as kaon if it also satisfies muon particle identification criteria.

In order to minimize systematic effects the same kaon particle identification criteria were also used in the reference mode $D^+ \to K^-\pi^+\pi^+$. No particle identification was applied to the pion candidates in the reference mode.

7.3 Event Weight Functions

The following section describes necessary weight functions to accommodate the dependency of the reconstruction efficiency on the candidate momentum or the Dalitz structure in the $D^+ \to K^-\pi^+\pi^+$ case.

7.3.1 Momentum Weight Function

The D^{*+} reconstruction efficiency has a slight dependence on the momentum of the candidate, which has to be taken into account as the D^{*+} momentum spectrum in data could be different from the one generated in Monte Carlo. To correct for this, we calculate the ratio, binned in $x_{D^{*+}}$, of selected reconstructed candidates over all generated candidates. Then we perform a first order polynomial fit to this distribution of ratios. The results of the fit are shown in Figure 7.5 for the reference mode and the two signal modes. The fact that the efficiency drops for higher values of $x_{D^{*+}}$ in the cases with a π^0 in the final state of the D^+ decay is due to a lower

Variable	fit parameter		
p_0	0.9834	$\pm$	0.0070
p_1	0.0048	$\pm$	0.0187
p_2	-0.010	$\pm$	0.0061
p_3	0.1062	$\pm$	0.0446

Table 7.5: Coefficients of the $D^+ \to K^-\pi^+\pi^+$ Dalitz weight function fit following equation 7.6.

reconstruction efficiency for high momentum π^0 in the calorimeter as they have a higher likelihood to produce merged π^0's where the two photons cannot be separated well enough. The fit functions are taken into account in the maximum likelihood fit of all three decay modes with the systematic contributions of the order of 0.5 % discussed in Chapter 9.

7.3.2 $D^+ \to K^-\pi^+\pi^+$ Dalitz Weight Function

For the $D^+ \to K^-\pi^+\pi^+$ mode, the reconstruction efficiency depends on the candidates position in the $m_{12}^2 - m_{13}^2$ plane (or Dalitz plane), where m_{12}^2 (m_{13}^2) denotes the squared invariant mass combining the K^- with the first (second) π^+ of the $D^+ \to K^-\pi^+\pi^+$ decay.

To account for possible differences between data and MC distribution of events in the Dalitz plane, a weight function was extracted based on 700k $D^+ \to K^-\pi^+\pi^+$ Monte Carlo events. The initial structure in the Dalitz plane was generated according to a phase space distribution. Plots for the initial Monte Carlo Truth (properties of particles in events as they were simulated) distribution and the reconstructed distribution after all selection steps were done in the $m_{12}^2 - m_{13}^2$ plane which was divided into 45×45 cells. The reconstructed sample was weighted with the momentum dependent weight function to take this effect properly into account. The Monte Carlo truth distribution was smeared out to accommodate effects of the finite D^+ mass resolution. All cells with less than 100 entries in the truth distribution were discarded to avoid any edge effects. The top left plot in figure 7.3.2 shows the Dalitz distribution of all reconstructed events accepted after all cuts. The top right plot shows the ratio of the reconstructed events over the generated distribution weighted with the selection efficiency to obtain an average value of one. For the extraction of a weighting function a polynomial function is fitted to the Dalitz ratio distribution. In order to minimize the correlations between the individual fit parameters of the function a variable transformation is performed beforehand. The following function was used :

$$
\begin{aligned}
m^2_{12',13'} &= m^2_{12,13} - \frac{1}{2}((m_K + m_\pi)^2 + (m_D - m_\pi)^2) && (7.3)\\
x &= \frac{1}{\sqrt{2}} m^2_{12'} + \frac{1}{\sqrt{2}} m^2_{13'} && (7.4)\\
y &= -\frac{1}{\sqrt{2}} m^2_{12'} + \frac{1}{\sqrt{2}} m^2_{13'} && (7.5)\\
C &= p_0(1 + p_1 x^2 + p_2 y^2 + p_3 x^2 y^2) && (7.6)
\end{aligned}
$$

Equation 7.6 describes this transformation which consists of a shift of the coordinate origin to the center of the distribution followed by a clockwise turn of the coordinate system of 45 degrees. The weighting function itself has four free parameters, one used for normalization and the remaining being even in x and y to utilize the symmetry of the distribution.

Shown in the bottom left of Figure 7.3.2 is the resulting weight function. One can see from the plot the deviation from one is relatively small at a maximum level of ± 3 %. The effect of this weight function on the systematical uncertainties is discussed later in Chapter 9.

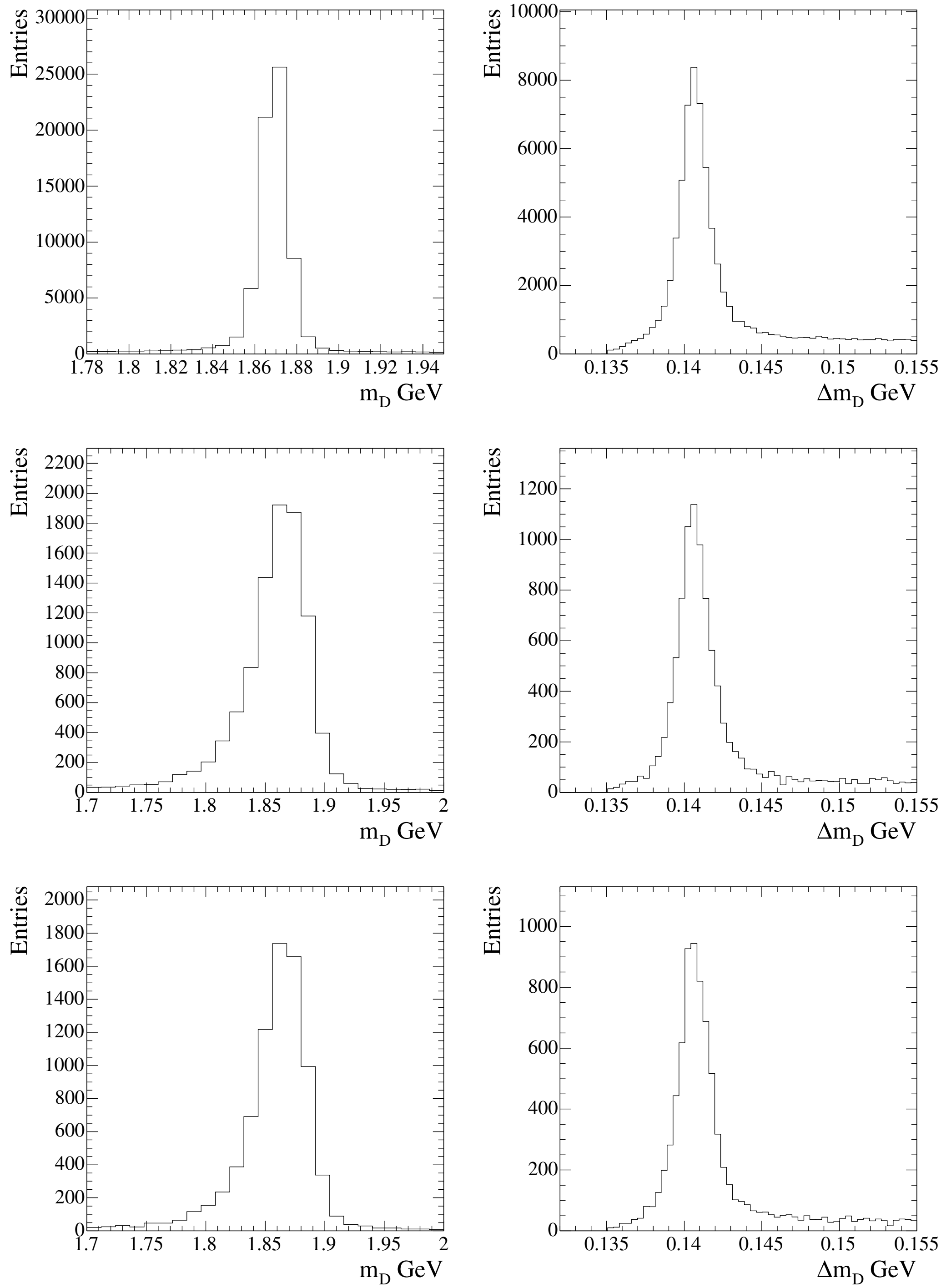

Figure 7.4: The left column shows the reconstructed D^+ mass, while the right shows the Δm mass difference for signal Monte Carlo in the $D^+ \to K^-\pi^+\pi^+$ (top), $D^+ \to \pi^+\pi^0$ (center) and $D^+ \to K^+\pi^0$ (bottom) modes.

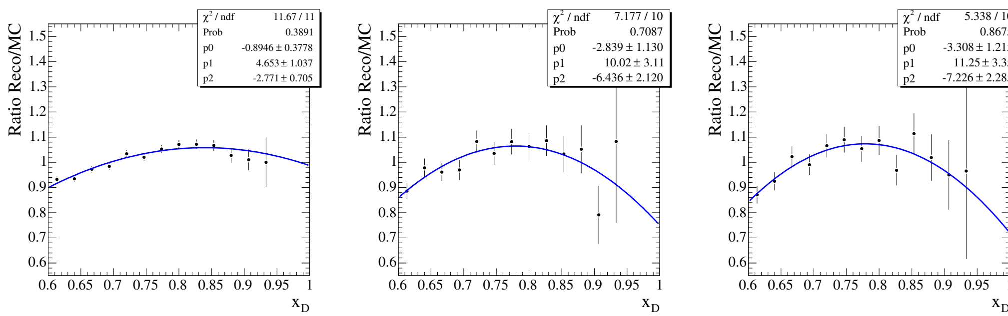

Figure 7.5: The three plots illustrate the dependence of the reconstruction efficiency from the normalized momentum $x_{D^{*+}}$. On the left it shows $D^+ \to K^-\pi^+\pi^+$, in the center $D^+ \to \pi^+\pi^0$ and on the right $D^+ \to K^+\pi^0$.

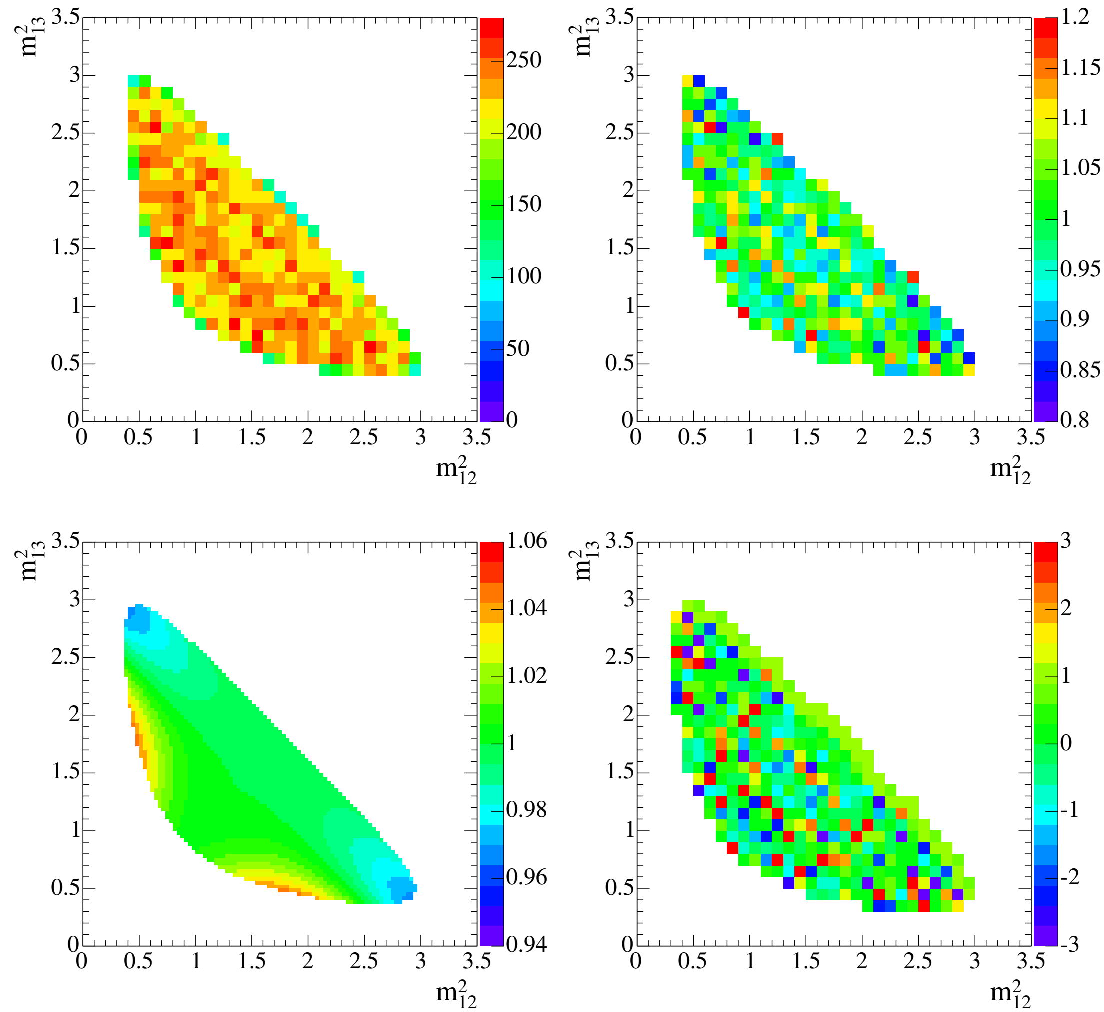

Figure 7.6: The top left plot show the distribution of all accepted reconstructed events in the $D^+ \to K^-\pi^+\pi^+$ Dalitz plane. In the top right the ratio of the reconstructed over generated events is shown corrected for the selection efficiency. The bottom left shows the result of the weight function fit of equation 7.6. The bottom right shows the signed χ^2 distribution of the fit result.

CHAPTER 8

Maximum Likelihood Fit

A maximum likelihood fit to the D^+ mass distribution was performed for both signal and reference modes. The aim of the fits was to extract the event yield for the full decay chain $D^{*+} \to D^+\pi^0_{soft}$ with the D^+ either decaying to the $D^+ \to \pi^+\pi^0$ or $D^+ \to K^+\pi^0$ signal modes or the $D^+ \to K^-\pi^+\pi^+$ reference mode. The event yield should not include D^+'s decaying into any of our final states where the D^+ does not origin from a $D^{*+} \to D^+\pi^0_{soft}$ decay.

This causes a problem since the BaBar dataset contains many D^+ mesons that do not origin from a $D^{*+} \to D^+\pi^0_{soft}$ decay. Some of them will decay into our final states and a certain fraction of those we will reconstruct. The Δm cut will remove most of these events, but some of these D^+ will by pure chance be combined with a random π^0 and satisfy the Δm cut. The result is a component in the D^+ mass distribution that is considered background but peaks just below the signal peak. Naively one could assume that the relative amount of these decays is the same for all D^+ decay modes and should therefore cancel out in the branching fraction ratio. That is not the case, Monte Carlo studies show clearly that after the reconstruction the relative fraction of these D^+ decays is different in the $D^+ \to K^-\pi^+\pi^+$ and the two signal modes.

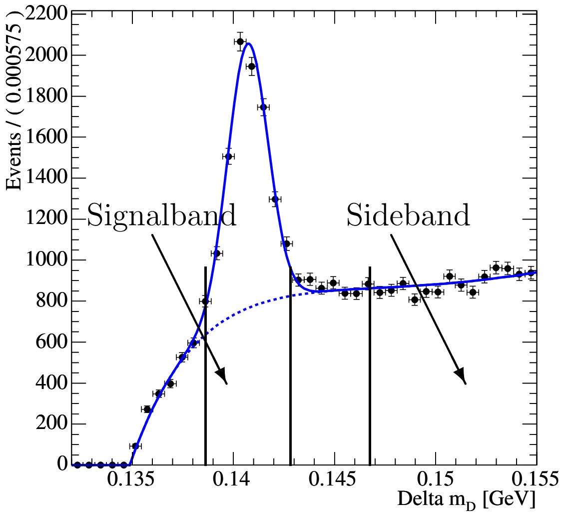

Figure 8.1: The plot on the left shows the Δm signal Monte Carlo distribution for the $D^+ \to K^+\pi^0$ mode. Illustrated by vertical lines is the signalband and sideband regions as defined in the text.

By splitting the Δm mass distribution into a signalband and sideband region, followed by a separate fit of the D^+ mass spectrum for these two categories of events, a corrected event yield can be extracted.

Illustrated in Figure 8.1 is the Δm signal Monte Carlo distribution for the $D^+ \to K^+\pi^0$ mode with an arbitrary large signal cross section. Based on a single Gaussian fit to the mass peak the signalband is defined as a two sigma region while the sideband region starts five sigma above the nominal $D^{*+} - D^+$ mass difference and ends at $0.155\,\mathrm{GeV}/c^2$. The fit to the D^+ mass spectrum in the signalband yields the total number of $D^+ \to K^+\pi^0$ events from all sources, while the same fit for the sideband yields only $D^+ \to K^+\pi^0$ events which do not come from a $D^{*+} \to D^+\pi^0_{soft}$ decay. To extract the number of $D^+ \to K^+\pi^0$ events which do come from a $D^{*+} \to D^+\pi^0_{soft}$ decay, we take the signalband event yield and subtract from it the sideband event yield scaled with the signalband-to-sideband background area ratio in the Δm distribution. A detailed discussion on the signalband-to-sideband ratio extraction is provided in Section 9.7. There is a small systematic error associated to this method from events which are genuine $D^{*+} \to D^+\pi^0_{soft}$ decays not successfully reconstructed in the signalband ending up in the sideband.

8.1 The Fit

The individual components of the fit to the D^+ mass spectrum are slightly different for the $D^+ \to K^-\pi^+\pi^+$ reference mode and $D^+ \to \pi^+\pi^0$ and $D^+ \to K^+\pi^0$ signal modes. The high statistics reference mode is modeled by a double Gaussian for the signal and a first order polynomial for the background. The fit is constructed in a way that a simultaneous fit to the signalband and sideband distribution uses the same fit parameters to describe the shape of the signal Gaussian as it is independent of the origin of the D^+. The parameters of the polynomial used for the background are constrained for the signalband and sideband to be the same. Figure 8.2 illustrates a fit to $D^+ \to K^-\pi^+\pi^+$ Monte Carlo including the contributions from simulated background. The red component shown in Figure 8.2 is the contribution from peaking background which is extracted from the fit to the Δm sideband.

For the $D^+ \to \pi^+\pi^0$ and $D^+ \to K^+\pi^0$ signal modes a bifurcated Gaussian is chooses for the signal. For the background we also use a first order polynomial, but there is an additional background contribution from specific three-body decays which has to be modeled. Decays such as $D^+ \to K_s\pi^+$ with $K_s \to \pi^0\pi^0$ and $D^0 \to K_s\pi^0$ with $K_s \to \pi^+\pi^-$ can be incorrectly reconstructed as a $D^+ \to \pi^+\pi^0$ decay by picking up a π^0 and a π^+ from the original three-body decay. In a similar way the decay

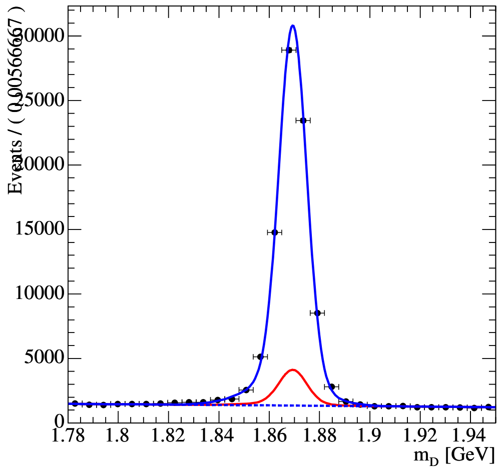

Figure 8.2: Result of a $D^+ \to K^-\pi^+\pi^+$ reference mode Monte Carlo fit. The red curve illustrates the peaking background component from D^+ decays which do not origin from D^{*+} extracted from the Δm sideband.

$D^+ \to K_s K^+$ is contributing to the $D^+ \to K^+\pi^0$ signal mode. When reconstructed as a candidate in one of the signal modes, the invariant mass spectrum for these background decays peaks at relatively low values but with tails toward higher masses close to the D^+ mass. Figure 8.3 illustrates this behavior by separating out two such three-body D^+ decays which are reconstructed as $D^+ \to \pi^+\pi^0$ and displaying them on top of the remaining background. There are other modes, like for instance $D^0 \to \rho^+\pi^-$, contributing to the same effect. This extra contribution is modeled by an additional exponential added to the background description. Fraction and slope are allowed to be different in the D^+ mass spectrum fits to signalband and sideband.

8.2 Validation

To validate the background model used in the analysis for the $D^+ \to \pi^+\pi^0$ and $D^+ \to K^+\pi^0$ signal modes, we fitted a data sample of simulated background Monte Carlo events only (removing the signal and reference mode events before the fit).

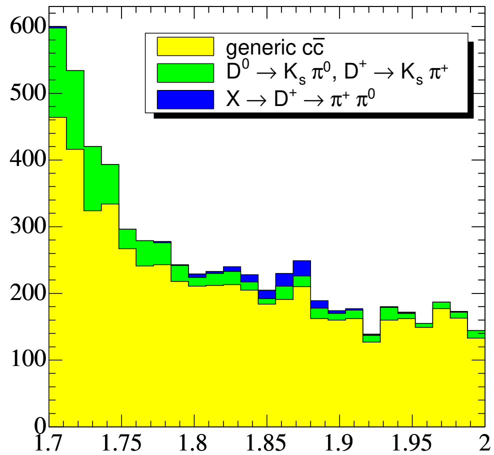

Figure 8.3: The plot on the left illustrates the additional component at low mass contributing to the background which origins from specific three-body decays where one of the decay products is not included in the $D^+ \to \pi^+\pi^0$ candidate. The fit accounts for this effect by fitting the extra component with an Exponential.

The results were compatible with zero in all cases within the statistical uncertainties, validating the background model and background subtraction method. Figure 8.4 illustrates examples of these fits for $D^+ \to \pi^+\pi^0$ on the left and $D^+ \to K^+\pi^0$ on the right. The D^+ signal event yields extracted from these two fits were $N(D^+ \to \pi^+\pi^0) = -14.9 \pm 46.5$ and $N(D^+ \to K^+\pi^0) = 19.3 \pm 28.4$. Different to our normal fit procedure, in these two cases the mean and sigma of the signal Gaussian was fixed to the values extracted from signal Monte Carlo.

For validation of the complete procedure MC sample containing both background and signal MC events for both $D^+ \to \pi^+\pi^0$ and $D^+ \to K^-\pi^+\pi^+$ modes were used. The Monte Carlo statistic was equivalent to $95 fb^{-1}$ of data.

The $D^+ \to \pi^+\pi^0$ branching fraction was extracted by using equation 6.9 with $BF(D^+ \to K^-\pi^+\pi^+) = 0.09$ as this is the value used in the Monte Carlo simulation. The Monte Carlo input signal branching fraction was set to $BF(D^+ \to \pi^+\pi^0) = 2.6 \cdot 10^{-3}$. The numbers extracted from the fit were $N_{fit}(D^+ \to \pi^+\pi^0) = 1893.8 \pm 81.4$

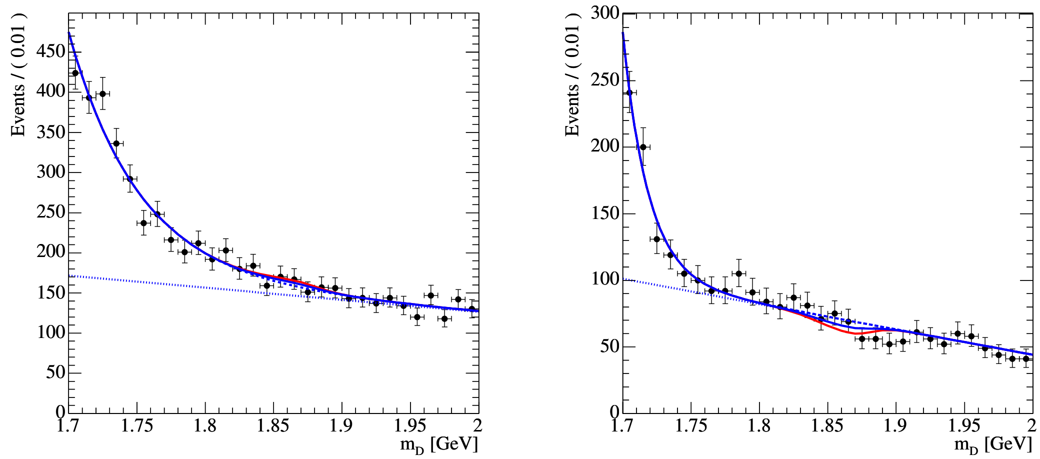

Figure 8.4: Fits to the simulated background Monte Carlo for $D^+ \to \pi^+\pi^0$ and $D^+ \to K^+\pi^0$ signal modes. The exponential component origins from certain three-boy decays where only two of the three decay products are picked up to form a D^+ candidate.

and $N_{fit}(D^+ \to K^-\pi^+\pi^+) = 70990.7 \pm 343.2$. The reconstruction efficiencies are $\epsilon_{D^+\to K^-\pi^+\pi^+} = 0.092$ and $\epsilon_{D^+\to\pi^+\pi^0} = 0.079$ (see Table 7.4). Based on equation 6.9 a branching fraction of $BF(D^+ \to \pi^+\pi^0) = (2.49 \pm 0.11) \cdot 10^{-3}$ is calculated where the error given is statistical only. The result is in agreement with the input value. Table 8.1 lists the different fit results and also provides numbers for the intermediate steps before the peaking background component is subtracted.

Figures 8.5 and 8.6 show the D^+ mass for the signalband and sideband and the Δm distributions in the $D^+ \to K^-\pi^+\pi^+$ reference and $D^+ \to \pi^+\pi^0$ signal mode.

The same test with a full Monte Carlo simulation was made in the $D^+ \to K^+\pi^0$ case. A branching ratio ten times smaller than in the $D^+ \to \pi^+\pi^0$ mode of

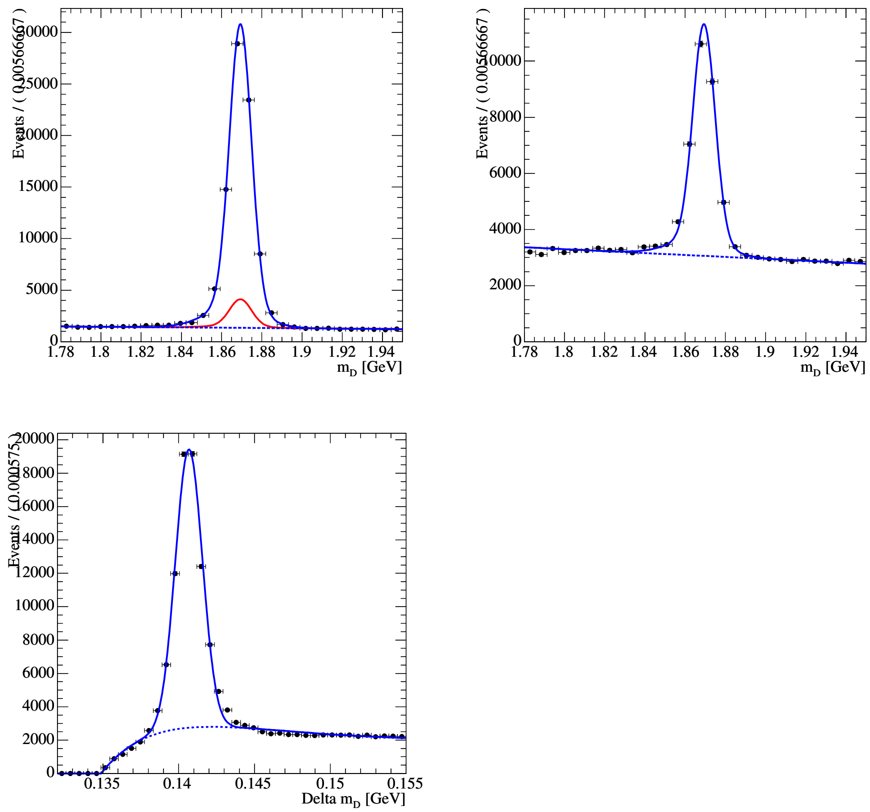

Figure 8.5: The plots show a Monte Carlo fit in the $D^+ \to K^-\pi^+\pi^+$ reference mode. In the top left plot the signalband fit with the peaking background drawn in red extracted from the fit to the sideband plotted on the right is shown. The bottom plot shows the Δm distribution enhanced by a two sigma D^+ mass cut.

$BF(D^+ \to K^+\pi^0) = 2.6 \cdot 10^{-4}$ was used as input to the Monte Carlo simulation. The fitting strategy for the $D^+ \to K^+\pi^0$ mode is slightly different in that no significant signal is expected and therefore the signal shape parameters are fixed and derived from the $D^+ \to \pi^+\pi^0$ mode with the mean fixed to the same value as in the $D^+ \to \pi^+\pi^0$ mode and the width to be 5 % narrower as determined by Monte Carlo. A detailed discussion can be found in the systematic Section 9.5.

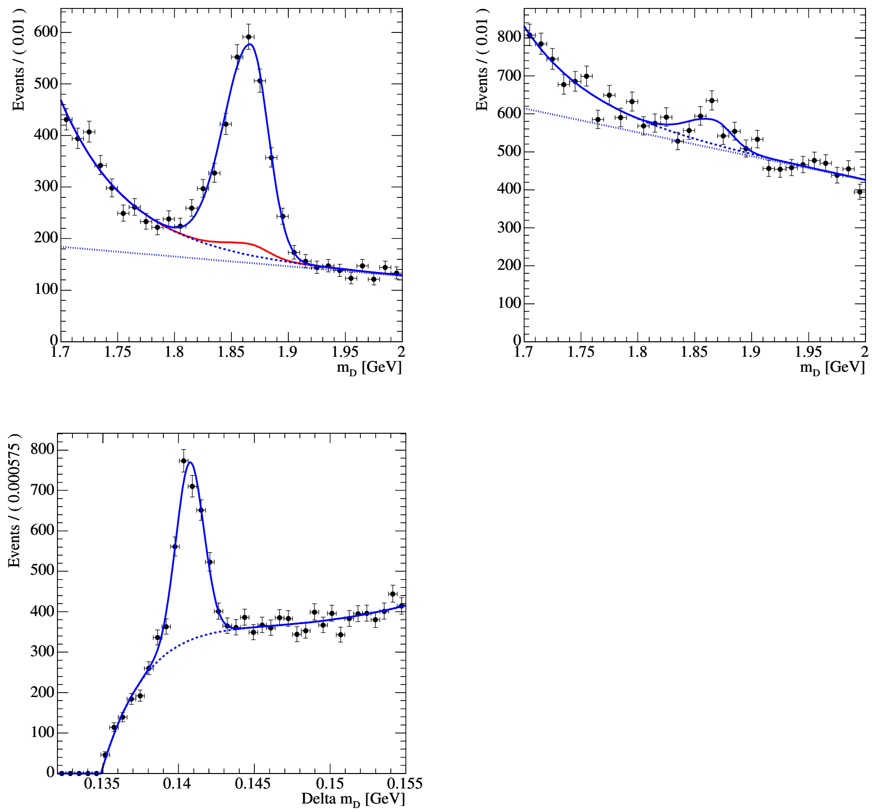

Figure 8.6: The plots show a Monte Carlo fit in the $D^+ \to \pi^+\pi^0$ signal mode. In the top left plot the signalband fit with the peaking background drawn in red extracted from the fit to the sideband plotted on the right is shown. The bottom plot shows the Δm distribution enhanced by a two sigma D^+ mass cut.

The fitted number for $D^+ \to K^-\pi^+\pi^+$ mode is $N_{fit}(D^+ \to K^-\pi^+\pi^+) = 67428.7 \pm 354.4$. The number of events for $D^+ \to K^+\pi^0$ are $N_{fit}(D^+ \to K^+\pi^0) = 164.5 \pm 32.1$ when the peaking D^+ background component is left free in the fit. As this peaking background fluctuates to a negative value the fit is repeated and the peaking D^+ background is constrained to zero. The numbers extracted from the constrained fit are $N_{fit}(D^+ \to K^+\pi^0) = 125.5 \pm 29.4$. The reconstruction efficiency is $\epsilon_{D^+ \to K^+\pi^0} = 0.060$. Based on equation 6.9 a branching fraction of $BF(D^+ \to K^+\pi^0) = (0.21 \pm 0.05) \cdot 10^{-3}$ is derived where the given error is statistical only. The result is in agreement with the input value. See Table 8.1 for the individual fit numbers.

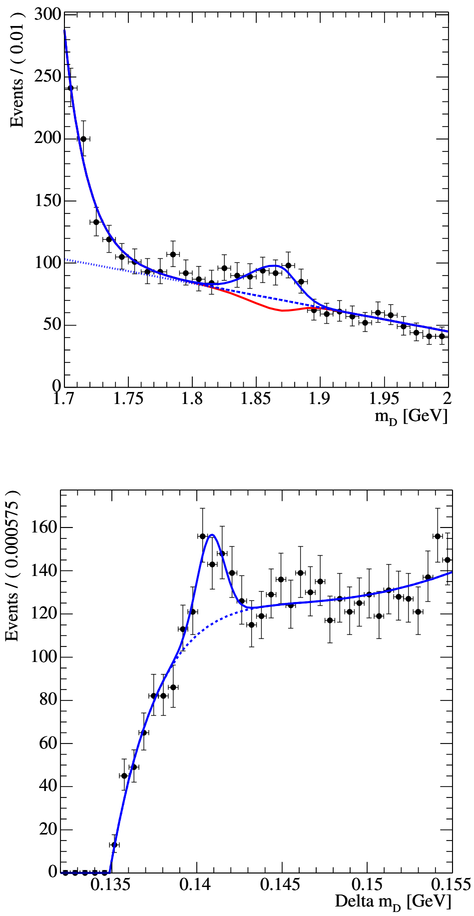

Figure 8.7: Monte Carlo fit results in the $D^+ \to K^+\pi^0$ mode for the signalband on the left and the sideband on the right. The branching fraction put into the simulation is $BF(D^+ \to K^+\pi^0) = 2.6 \cdot 10^{-4}$. The bottom plot shows the Δm distribution enhanced by a two sigma D^+ mass cut.

Figure 8.7 shows the D^+ mass distributions of the fit for the signalband and sideband in the $D^+ \to K^+\pi^0$ signal mode

8.3 Data Fit Results

The data was fitted in the same way as the Monte Carlo sample described above. The yields for the $D^+ \to K^-\pi^+\pi^+$, $D^+ \to \pi^+\pi^0$ and $D^+ \to K^+\pi^0$ were extracted separately. Monte Carlo showed that the signal shapes in the D^+ mass distribution are very similar in the $D^+ \to K^+\pi^0$ and $D^+ \to \pi^+\pi^0$ case. No significant signal was expected for the $D^+ \to K^+\pi^0$ mode, which meant that leaving the signal shape parameters (mean and width of the signal Gaussian) free in the $D^+ \to K^+\pi^0$ fit was not a good option. Instead, these signal shape parameters were extracted from the $D^+ \to \pi^+\pi^0$ fit result. A small correction of 0.95 was applied to the expected width based on Monte Carlo studies. A more detailed discussion including the systematic impact of this procedure can be found in Section 9.5.

The fit results for the $D^+ \to K^-\pi^+\pi^+$ mode are shown in Figure 8.8. The extracted yield is $N^{fit}_{D^+\to K^-\pi^+\pi^+} = 93519.7 \pm 416.7$ where the given error is statistical only. Figure 8.9 and 8.10 show the fits for the $D^+ \to \pi^+\pi^0$ and $D^+ \to K^+\pi^0$ mode. The extracted signal yields are $N^{fit}_{D^+\to\pi^+\pi^0} = 1229.2 \pm 97.6$.

Similar to the $D^+ \to \pi^+\pi^0$ mode a fit is made to the $D^+ \to K^+\pi^0$ mode. The analysis cuts are the same except a tighter cut on the $cos(\Theta_{Helicity} < 0.7$ is applied when fitting for the kaon signal mode. This leads to a slightly lower fitted yield in the reference mode (to be consistent and avoid systematic effects the cut is also applied to that sample) of $N^{fit}_{D^+\to K^-\pi^+\pi^+} = 89029.2 \pm 396.7$. The strategy for the $D^+ \to K^+\pi^0$ is two-folded as follows: The peaking background yield is expected to be very low and therefore could fluctuate below zero. In order to avoid utilizing this effect it was decided beforehand that if such a case happens the peaking background component is fixed to zero and the fit is redone. Shown in the two top plots of figure 8.10 is the fit result for the fit with floating peaking background with a visible negative component of peaking D^+ background. The center plot shows the same fit with the peaking component fixed to zero, which yields $N^{fit}_{D^+ \to K^+\pi^0} = 162.4 \pm 33.4$. This yield number is to be used to calculate the final branching fraction. Table 8.1 lists all individual fit numbers for the different modes and also provides numbers for the intermediate steps before the peaking background component is subtracted.

Ignoring systematic errors and corrections discussed in the next chapter and using equation 6.9 and the selection efficiencies from Table 7.4, the following branching fraction ratios are extracted

$$\frac{\mathcal{B}(D^+ \to \pi^+\pi^0)}{\mathcal{B}(D^+ \to K^-\pi^+\pi^+)} = (1.32 \pm 0.11\ (\text{stat.})) \cdot 10^{-2} \tag{8.1}$$

for the $D^+ \to \pi^+\pi^0$ mode and

$$\frac{\mathcal{B}(D^+ \to K^+\pi^0)}{\mathcal{B}(D^+ \to K^-\pi^+\pi^+)} = (2.27 \pm 0.47\ (\text{stat.})) \cdot 10^{-3} \tag{8.2}$$

for the $D^+ \to K^+\pi^0$ mode.

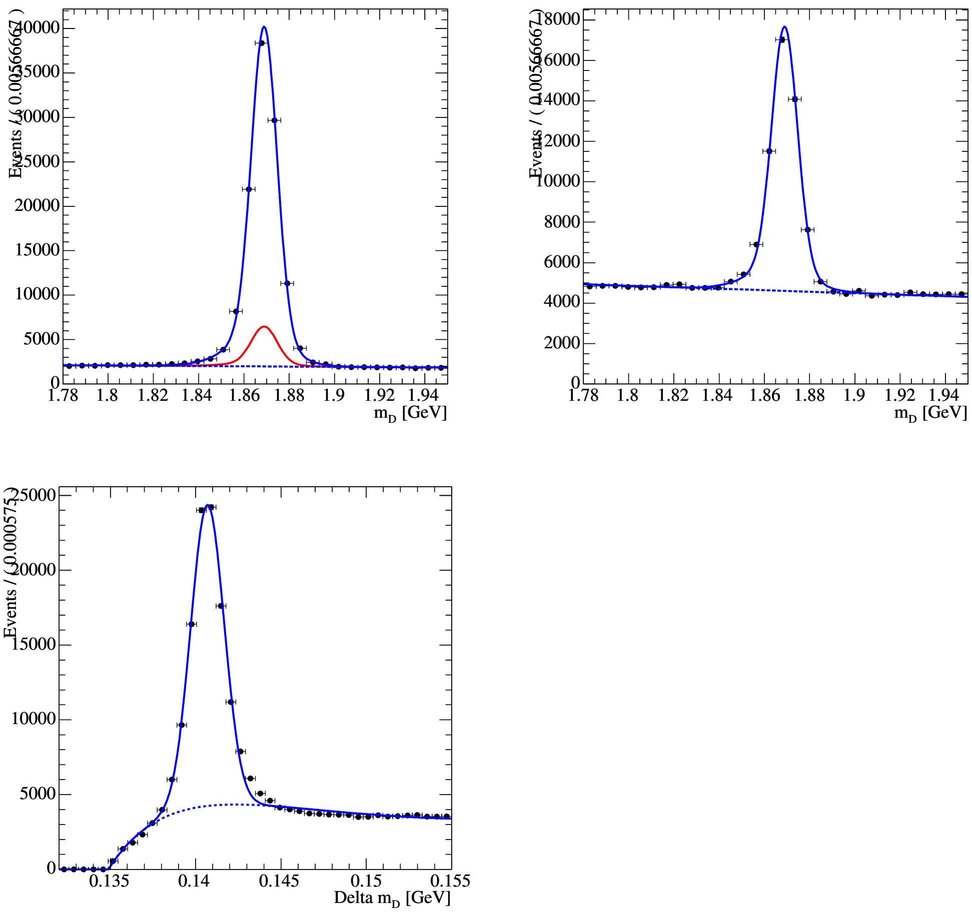

Figure 8.8: $D^+ \to K^-\pi^+\pi^+$ reference mode fit. The top left(right) plot shows the Δm signalband(sideband) fit to the D^+ mass spectrum. The bottom left illustrates the Δm distribution enhanced by a two sigma D^+ mass cut.

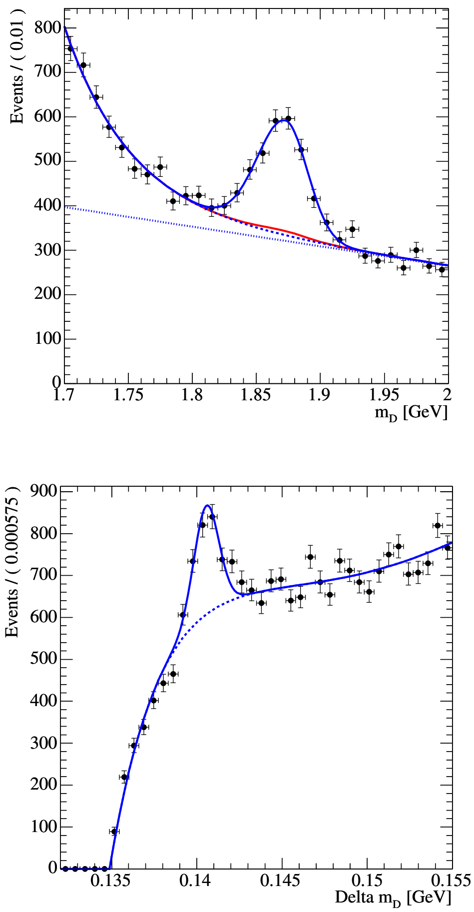

Figure 8.9: $D^+ \to \pi^+\pi^0$ signal mode data fit. The top left(right) plot shows the Δm signalband(sideband) fit to the D^+ mass spectrum. The bottom left illustrates the Δm distribution enhanced by a two sigma D^+ mass cut.

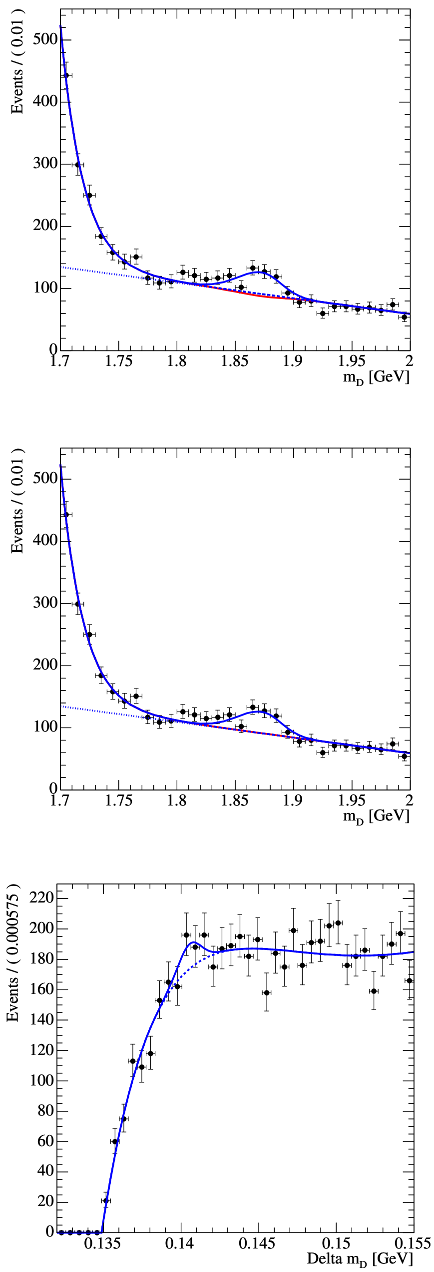

Figure 8.10: $D^+ \to K^+\pi^0$ signal mode data fit. The top left(right) plot shows the D^+ mass distribution (zoomed view) with floating peaking background contribution. The center plots show the same with the peaking component fixed to zero. The bottom left illustrates the Δm distribution enhanced by a two sigma D^+ mass cut and the bottom right D^+ mass distribution from the Δm sideband.

Fit Sample	D^+ yield Δm Signalband	D^+ yield Δm Sideband	Signal-to-Sideband Ratio	Final D^+ yield
$D^+ \to \pi^+\pi^0$ Monte Carlo uncons.	1998.7	313.3 ± 81.6	0.335 ± 0.017	1893.8 ± 81.4
$D^+ \to K^-\pi^+\pi^+$ Monte Carlo	78347.1	21970.2 ± 208.1	0.335 ± 0.017	70990.7 ± 343.2
$D^+ \to K^+\pi^0$ Monte Carlo uncons.	124.6	-118.2 ± 39.9	0.337 ± 0.017	164.5 ± 32.1
$D^+ \to K^+\pi^0$ Monte Carlo cons.	125.5	0	0.337 ± 0.017	125.5 ± 29.4
$D^+ \to K^-\pi^+\pi^+$ Monte Carlo	74444.3	20825.8 ± 207.7	0.337 ± 0.017	67428.7 ± 354.4
$D^+ \to \pi^+\pi^0$ Data uncons.	1274.5	131.8 ± 116.2	0.343 ± 0.016	1229.2 ± 97.6
$D^+ \to K^-\pi^+\pi^+$ Data	105951.0	36197.3 ± 268.1	0.343 ± 0.016	93519.7 ± 416.7
$D^+ \to K^+\pi^0$ Data uncons.	162.7	-50.2 ± 47.4	0.344 ± 0.016	179.9 ± 37.0
$D^+ \to K^+\pi^0$ Data cons.	162.4	0	0.344 ± 0.016	162.4 ± 33.4
$D^+ \to K^-\pi^+\pi^+$ Data	100861.0	34376.8 ± 256.9	0.344 ± 0.016	89029.2 ± 396.7

Table 8.1: The table shows the individual contributions to the final D^+ yield extracted from the fit for Monte Carlo and Data. The $D^+ \to K^+\pi^0$ mode fits were made in two different configurations with the peaking D^+ background floating in the fit or constrained to zero. The second column (a) list the raw D^+ yield of events from the Δm signalband and the third column (b) the D^+ yield from the Δm sideband. Column four (c) lists the signalband-to-sideband ratio of the Δm distribution. The final column (d) provides the final D^+ yield used in the branching fraction calculation which is derived as (d) = (a) - (b)(c).

CHAPTER 9

Systematic Errors

The systematic uncertainties in the analysis can be split into two different classes. The first class consists of all error sources that effect the precise knowledge of the reconstruction efficiency derived from the signal Monte Carlo. Error of this type are listed in Table 9.1 at the end of this section. The second class of systematics includes all contributions which can be associated with the fitted event yield in the $D^+ \to \pi^+\pi^0$, $D^+ \to K^+\pi^0$ and $D^+ \to K^-\pi^+\pi^+$ mode listed in Table 9.2.

9.1 Track Reconstruction and Vertexing

Following the recipe of the BaBar tracking efficiency group [28] we apply a flat correction of -0.5 % added linearly for every track with a systematic uncertainty of 0.8 % for each track. This number is derived from the weighted average uncertainty of 1.3 % for low momentum tracks below 200 MeV and 0.5 % for high momentum tracks. This leads to a correction factor of 0.985 for the $D^+ \to K^-\pi^+\pi^+$ mode and 0.995 for the $D^+ \to \pi^+\pi^0$ and $D^+ \to K^+\pi^0$ signal modes. As the final branching fraction calculation includes the ratios of the reconstruction efficiencies (see equation 6.9), part of the errors cancel out. Therefore the relative systematic error contribution from tracking is 1.6 %. A possible influence from the D^+ candidate vertexing can only occur by means of data and Monte Carlo differences effecting the reconstruction efficiencies taken from signal Monte Carlo. The only cut applied on the vertexing level is the 10^{-3} requirement on the χ^2 probability. The data and Monte Carlo agreement of this cut was studied in different analysis [31, 33], all quoting a systematic error of less than 1 %. Therefore we also use a systematic error of 1 % for the vertexing. Combined with the 1.6 % quoted above this leads to a total track related error of 1.9 %.

9.2 Particle Identification

The BaBar particle identification group provides correction tables for the PID selectors to account for differences between data and MC [29]. When calculating the reconstruction efficiency in signal MC, these correction tables are applied to insure that the PID selectors work the same way as on data.

Because the same kaon PID selector is used in the $D^+ \to K^+\pi^0$ and $D^+ \to K^-\pi^+\pi^+$ mode any systematic effects cancel out to first order in the ratio. Any remaining differences are due to the difference in the kaon momentum spectrum for the two decays and it's modeling by the PID corrections. Adding these contributions in quadrature yields a systematic PID error of 0.4 % for the $D^+ \to K^+\pi^0$ mode.

In the $D^+ \to \pi^+\pi^0$ case two different PID selectors are used and both PID selectors contribute to the systematic error. The per track uncertainty is based on the statistical uncertainty in the correction tables used for the PID correction, which is 0.7 % for the kaon and 0.6 % for the pion case. This yields to a total systematic PID error of 0.9 % for the $D^+ \to \pi^+\pi^0$ mode.

9.3 π^0 Reconstruction

Systematic uncertainties in the reconstruction of the slow π^0 which forms the D^{*+} candidates can be neglected as they are identical for the signal and reference mode and therefore cancel out in the branching fraction calculation. Following the recipe of the neutral working group [32], we apply a 0.984 correction factor to the $D^+ \to \pi^+\pi^0$ and $D^+ \to K^+\pi^0$ signal mode efficiencies with a systematic uncertainty of 3.2 %.

9.4 Fit Weight Function

The systematic contribution of the fit weight function comes from several sources. The weight function is normalized in a way that the signal Monte Carlo returns a weight equal to the input number of events and the resulting efficiency does not change for these samples. As the weight function is applied to the full data sample the total sample weight changes slightly and therefore affect the yield fit error. This relative change of the sample weight is 2.8 % for the $D^+ \to \pi^+\pi^0$, 2.7 % for the $D^+ \to K^+\pi^0$ and 0.4 % for the $D^+ \to K^-\pi^+\pi^+$ data sample. This changes are taken into account as uncertainty on the fit error.

The momentum weight functions are extracted from fits to $D^+ \to \pi^+\pi^0$ and $D^+ \to K^+\pi^0$ Monte Carlo. The Dalitz plane weight function is extracted from phase space $D^+ \to K^-\pi^+\pi^+$ Monte Carlo. In order to account for the uncertainties of these weight function fits, the fit parameters were varied within their error, new weights were calculated and the variation on the fitted event yield was extracted. Test were also done to check the size of the yield variation in the case of no momentum weighting. The results are very small variations in the yield as the momentum weight function is rather flat. This was done individually for the different modes and the following systematic uncertainties on the fitted D^+ event yield were calculated : 0.8 % for the $D^+ \to \pi^+\pi^0$, 0.8 % for the $D^+ \to K^+\pi^0$ and 1.2 % for the $D^+ \to K^-\pi^+\pi^+$ mode. Column six of Table 9.2 lists the systematic contribution of this source to the final D^+ yield.

9.5 Signal Parametrization

The signal shape for the $D^+ \to K^-\pi^+\pi^+$ reference mode is a double Gaussian with floating mean and sigma and relative fraction in the fit. Monte Carlo studies have shown that fits using a double Gaussian yield the correct number of events quite nicely. Fitting pure reference mode Monte Carlo with a double Gaussian signal shape and with first and second order polynomial background parameterizations lead to yields which are between 2 % to 1 % lower than the input numbers.

Monte Carlo studies showed for both $D^+ \to \pi^+\pi^0$ and $D^+ \to K^+\pi^0$ signal modes a tail in the Gaussian toward lower masses. For this reason a bifurcated Gaussian parametrization for the signal shape was chosen. In the $D^+ \to \pi^+\pi^0$ mode the mean, left and right sigma were left floating in the fit. Fitting signal Monte Carlo with a bifurcated Gaussian signal shape leads to lowered yields of around 3 %. In the final branching fraction ratio calculation only the ratio of the fitted yields enters the calculation which is why most effects of the lower yields cancel out. A systematic uncertainty of 1.5 % is derived on the ratio of fitted yields which is incorporated in the final number.

The approach in the $D^+ \to K^+\pi^0$ case is very similar to the $D^+ \to \pi^+\pi^0$ case, but as a sizable signal is not expected one needs to fix the mean and sigma of the signal Gaussian in the fit. By comparing the Gaussian fits of Monte Carlo between the $D^+ \to \pi^+\pi^0$ and $D^+ \to K^+\pi^0$ mode, it was determined that the mean value is the same, but the width is around 5 % narrower in the $D^+ \to K^+\pi^0$ case. The fitted values were $m_{D^+\to\pi^+\pi^0} = 1.872$, $\sigma^{left}_{D^+\to\pi^+\pi^0} = 0.0311$ and $\sigma^{right}_{D^+\to\pi^+\pi^0} = 0.0146$ and in the $D^+ \to K^+\pi^0$ mode $m_{D^+\to K^+\pi^0} = 1.872$, $\sigma^{left}_{D^+\to K^+\pi^0} = 0.0282$ and $\sigma^{right}_{D^+\to K^+\pi^0} = 0.0138$. Therefore the data $D^+ \to \pi^+\pi^0$ fit result for the signal Gaussian is taken as input for the $D^+ \to K^+\pi^0$ fit with the sigma scaled by 0.95. The systematic effects were determined by varying the Gaussian sigma's of the $D^+ \to K^+\pi^0$ Monte Carlo by ± 5.0 %, fixing the sigma in the fit and extraction of the fitted yield. A relative yield variation of 2.2 % was found and is added in quadrature to the 1.5 % described above leading to a total systematic error of 2.7 % for the $D^+ \to K^+\pi^0$ mode.

9.6 Limited Monte Carlo Statistics

The reconstruction efficiencies are extracted from Monte Carlo samples with limited statistics. Therefore the statistical errors of the reconstruction efficiencies are included as systematic errors. The relative uncertainties are 1.0 % for $D^+ \to \pi^+\pi^0$, 1.1 % for $D^+ \to K^+\pi^0$ and 0.4 % for $D^+ \to K^-\pi^+\pi^+$.

9.7 Direct D^+ Background Subtraction

The background subtraction method doesn't have any extra systematic errors associated with it as any uncertainties are already included in the statistical error of the fitted yield. However, required as input to the fit are the ratio of the number of candidates in the signalband and sideband regions that is extracted from a fit to Δm. This ratio is derived from the ratio of the integral of the signalband and

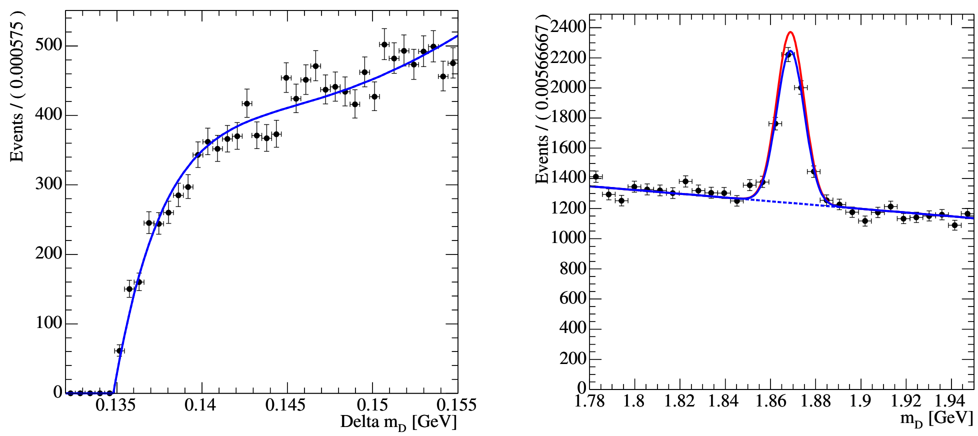

Figure 9.1: The left plots shows the Δm distribution from which the signalband-to-sideband ratio is extracted, while the right shows the fit result for a full Monte Carlo background sample with no signal $D^{*+} \to D^+\pi^0_{soft}\, D^+ \to K^-\pi^+\pi^+$ decays in the sample.

sideband areas under the fit and has a statistical uncertainty due to the limited number of events in the fit. The following fit function is used

$$F_{comb}(\Delta m) = \frac{1}{N}\left[1 - \exp\left(-\frac{\Delta m - \Delta m_0}{c_1}\right)\right]\left(\frac{\Delta m}{\Delta m_0}\right)^{c_2} + c_3\left(\frac{\Delta m}{\Delta m_0} - 1\right), \qquad (9.1)$$

where N is a normalization constant, c_1, c_2, c_3 are free parameters and Δm_0 is the kinematic threshold equal to m_π [34].

The only problem with this approach is that a Δm distribution free of any $D^{*+} \to D^+\pi^0_{soft}$ decays needs to be fitted. This was achieved by selecting events in the D^+ mass sideband and also requiring the soft π^0 mass to be in the sideband below 0.12 GeV or above 0.148 GeV. In addition to the statistical uncertainty of this procedure an extra systematic contribution was found in Monte Carlo studies due to some remaining D^{*+} contamination. The size of this contribution is estimated to be an absolute 1.5 % on the ratio , which is added in quadrature to the statistical error. The signal to sideband ratio extracted in the data derived from the $D^+ \rightarrow K^-\pi^+\pi^+$ mode is 34.3 ± 1.6 %. The same scale factor was used in all modes. This leads to a total relative uncertainty of around 3.5 % for the signal and reference modes which is taken into account as systematic error on the yield. Column five of Table 9.2 lists the systematic uncertainty on the final D^+ yield derived from this source.

As an example a fit to $D^+ \rightarrow K^-\pi^+\pi^+$ mode Monte Carlo is shown in Figure 9.7 for background events only with all $D^{*+} \rightarrow D^+\pi^0_{soft}$, $D^+ \rightarrow K^-\pi^+\pi^+$ removed from the sample. The fitted D^+ yield is $-335.8 \pm 104.8 \pm 157.5$ were the first number denotes the statistical error and the second one the systematic from the Δm signalband-to-sideband ratio error described above.

9.8 Δm in Signal and Reference Mode

The shape of the Δm distribution is dominated by the reconstruction of the slow π^0_{soft}. In order to avoid any direct dependency on the absolute slow π^0_{soft} reconstruction efficiency the fit assumes the Δm_D signal shapes to be identical for the individual modes.

This assumption is not completely correct. The mass resolution of the D^+ candidates has a small effect on the width of the Gaussian peak in the Δm distribution, resulting in slightly different widths in signal and reference modes. In addition, the number of events with a $D^{*+} \rightarrow D^+\pi^0$ decay where we correctly reconstructed the D^+ but then combine it with the wrong slow π^0_{soft} is also different between signal and reference modes. These events cause a certain amount of real signal to be subtracted as peaking background contribution and the differences between signal and

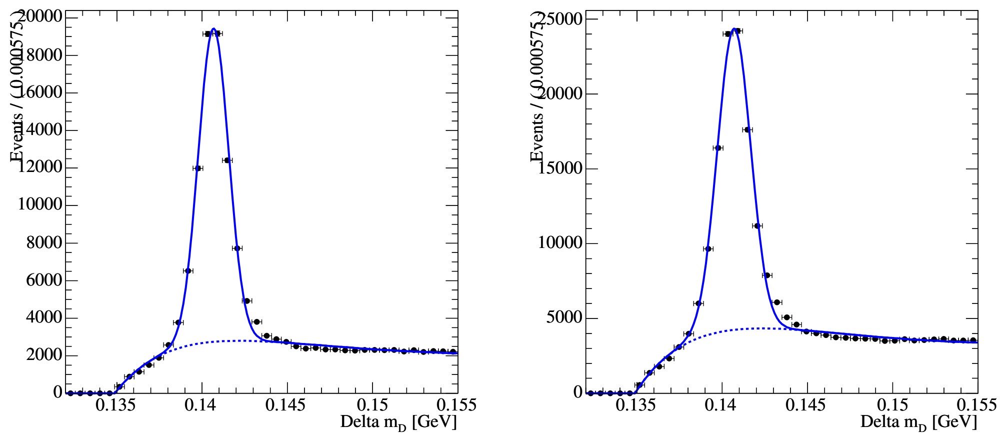

Figure 9.2: The two plots show Monte Carlo (left) and data (right) Δm distributions for the $D^+ \to K^-\pi^+\pi^+$ reference mode. The width is slightly wider for the data which accounts for an additional 1.0 % systematic uncertainty.

reference mode mean that the effect doesn't completely cancel out in the branching fraction ratio.

By comparing the number of events found in the signalband and sideband of the Δm distributions for the $D^+ \to \pi^+\pi^0$, $D^+ \to K^+\pi^0$ and $D^+ \to K^-\pi^+\pi^+$ Monte Carlo samples, we derive a total systematic error of 5 %, which is included into the efficiency ratio calculation.

9.9 Δm in Data and Monte Carlo

Besides the differences of the Δm shape between signal and reference modes discussed in the previous section there is also a difference between data and Monte Carlo which has to be taken into account. Fits to the Δm distribution were made for the $D^+ \to K^-\pi^+\pi^+$ reference mode in data and Monte Carlo (see Figure 9.9).

The fits were made for events passing the standard event and candidate cuts, followed by a two sigma signal cut in the D^+ mass to enhance the signal in Δm. The width of the Gaussian in the Δm fit are $9.67 \cdot 10^{-4} \pm 4.95 \cdot 10^{-6}$ for data and $8.9 \cdot 10^{-4} \pm 5.5 \cdot 10^{-6}$ for Monte Carlo. The relative difference in efficiency for the same Δm mass cuts for this fit results in a 1.0 % systematic error. A test on a limited amount of $D^+ \rightarrow \pi^+\pi^0$ data statistics leads to a similar result and a combined uncertainty of 1.4 % for the efficiency ratio is derived as the change in width is of opposite sign in the signal and reference modes.

9.10 Total Systematic Error

Listed in Table 9.1 are the individual contributions to the systematic error as discussed above for all sources which contribute to the signal reconstruction efficiencies. Table 9.2 lists the systematics which need to be incorporated into the individual event yields for the separate modes. The only two systematic contributions which require a correction of the efficiency ratio are the tracking corrections with 1.01 and the π^0 reconstruction efficiency with 0.984 leading to a final correction factor of 0.994 which is applied to the final branching fraction result.

Efficiency Ratio Systematics			
Description	$\sigma_\epsilon(K^-\pi^+\pi^+)$	$\sigma_\epsilon(\pi^+\pi^0(K^+\pi^0))$	$\sigma_{\epsilon-Ratio}$
Tracking and Vertexing	2.4 %	0.8 %	1.9 %
Particle Identification	0.7 %(–)	0.6 %(0.4 %)	0.9 %(0.4 %)
π^0 reconstruction	–	3.2 %	3.2 %
Monte Carlo Statistics	0.4 %	1.0 %(1.1 %)	1.1 %(1.2 %)
Δm Shape	–	–	5.0 %
Δm Data / MC	1.0 %	1.0 %	1.4 %
Signal Parametrization	1.5 %	3.0 %(+ 2.2 %)	1.5 %(2.7 %)
Total	–	–	**6.6 % (7.0 %)**

Table 9.1: The above table list the different systematic contributions for the individual modes. Some of the contributions cancel out as the final branching fraction is derived from a ratio. The numbers in parenthesis list the values for the $D^+ \to K^+\pi^0$ mode if they differ from the $D^+ \to \pi^+\pi^0$ mode. In all other cases they are considered to be the same.

Fit Sample	ΔM Signalb. D^+ yield	ΔM Sideb. D^+ yield $\pm$ stat.	Signal-to-Sideband Ratio	Peaking D^+ Bknd. Error	Weight Fun. Sys. Error	Final D^+ yield $\pm$ stat.	Total Sys. Error
$\pi\pi^0$ (UC)	1274.5	131.8 ± 116.2	0.343 ± 0.016	± 2.1	± 9.8	1229.2 ± 97.6	± 10.0
$K^-\pi^+\pi^+$	105951.0	36197.3 ± 268.1	0.343 ± 0.016	± 587.5	± 1122.2	93519.7 ± 416.7	± 1266.7
$K^+\pi 0$ (C)	162.4	0	0.344 ± 0.016	0	± 1.3	162.4 ± 33.4	± 1.3
$K^-\pi^+\pi^+$	100861.0	34376.8 ± 256.9	0.344 ± 0.016	± 560.7	± 1068.4	89029.2 ± 396.7	± 1205.9

Table 9.2: The table shows the systematic error contributions to the D^+ yield numbers extracted from the individual fits of the Data. The (C) and (UC) in the first column denotes if the fit was constrained/unconstrained wrst the peaking D^+ background. There are two contributions, one from the signal-to-sideband ratio uncertainty listed in column five and from the weight function uncertainty listed in column six. The last column shows the total systematic uncertainty on the final D^+ yield used in the branching fraction calculation.

CHAPTER 10

Results

The final results are extracted from the event yields of the D^+ mass fits as described in Chapter 8. Following the discussion on systematics in Chapter 9, the following numbers are extracted from equation 6.9 (see Chapter 8). The efficiencies entering the equation are the raw efficiencies listed in Table 7.4 with their systematic uncertainties listed in Table 9.1 taken into account through proper error propagation.

The number of events in the $D^+ \to K^-\pi^+\pi^+$ reference mode for the $D^+ \to \pi^+\pi^0$-fit is $N_{D^+\to K^-\pi^+\pi^+} = 93519.7 \pm 416.7(stat.) \pm 1266.7(sys.)$ where the second error denotes the systematic contribution derived from the peaking D^+ background and fit weight function uncertainties (see Table 9.2). The combined total error is 1333.5 or about 1.4% relative. Due to the slightly harder cut for $cos(\Theta_{Helicity})$ in the $D^+ \to K^+\pi^0$-mode the number of events for $D^+ \to K^-\pi^+\pi^+$ is $N_{D^+\to K^-\pi^+\pi^+} = 89029.2 \pm 396.7(stat.) \pm 1205.9(sys.)$. The total error is 1270.1 or 1.4 % relative.

In the signal modes an event yield of $N_{D^+\to\pi^+\pi^0} = 1229.2 \pm 97.6(stat.) \pm 10.0(sys.)$ is found and $N_{D^+\to K^+\pi^0} = 162.4 \pm 33.4(stat.) \pm 1.3(sys.)$. The systematic error contributions are the same as in the $D^+ \to K^-\pi^+\pi^+$ reference mode.

Following equation 6.9 the following branching fraction ratios are extracted

$$\frac{\mathcal{B}(D^+ \to \pi^+\pi^0)}{\mathcal{B}(D^+ \to K^-\pi^+\pi^+)} = (1.32 \pm 0.11 \text{ (stat.) } \pm 0.09 \text{ (sys.)}) \cdot 10^{-2} \tag{10.1}$$

for the $D^+ \to \pi^+\pi^0$ mode and

$$\frac{\mathcal{B}(D^+ \to K^+\pi^0)}{\mathcal{B}(D^+ \to K^-\pi^+\pi^+)} = (2.29 \pm 0.47 \text{ (stat.) } \pm 0.16 \text{ (sys.)}) \cdot 10^{-3} \tag{10.2}$$

for the $D^+ \to K^+\pi^0$ mode. The systematic error is derived from the systematic uncertainties on the efficiency ratio of 6.6 % for $D^+ \to \pi^+\pi^0$ and 7.0 % for $D^+ \to K^+\pi^0$ mode (see Table 9.1). The statistical error quoted for the ratios combines the statistical fit error and the systematic errors affecting the D^+ yields to a total error on the yield (see Table 9.2). The result in the $D^+ \to K^+\pi^0$ mode has a significance of 4.4 σ based on a scan of the likelihood fit function.

Using the experimentally measured branching fraction $\mathcal{B}(D^+ \to K^-\pi^+\pi^+) = 0.092 \pm 0.006$[6] the following branching fractions are extracted,

$$\mathcal{B}(D^+ \to \pi^+\pi^0) = (1.21 \pm 0.10 \text{ (stat.) } \pm 0.08 \text{ (sys.) } \pm 0.08 \text{ (pdg)}) \cdot 10^{-3} \tag{10.3}$$

and

$$\mathcal{B}(D^+ \to K^+\pi^0) = (2.11 \pm 0.43 \text{ (stat.) } \pm 0.15 \text{ (sys.) } \pm 0.16 \text{ (pdg)}) \cdot 10^{-4} \tag{10.4}$$

where the last error is due to the experimental uncertainty in the $D^+ \to K^-\pi^+\pi^+$ branching fraction.

Both results are in good agreement with the branching fraction ($D^+ \to \pi^+\pi^0$) and upper limit ($D^+ \to K^+\pi^0$) published by CLEO in [27].

The $D^+ \to K^+\pi^0$ mode is especially interesting since our result is the first observation of this decay mode. In the limit of SU(3)$_F$ symmetry, the following equation is fulfilled [35]

$$R_1 = 2 \times \left|\frac{V_{cs}}{V_{cd}}\right|^2 \frac{\Gamma(D^+ \to K^+\pi^0)}{\Gamma(D^+ \to \bar{K}^0 K^+)} = 1 \tag{10.5}$$

Using the world average for $|V_{cs}|$, $|V_{cd}|$ and $BF(D^+ \to \bar{K}^0 K^+)$, we extract a prediction for $BF(D^+ \to K^+\pi^0) = (1.56 \pm 0.16) \times 10^{-4}$, where the listed error is only based on the known errors for the CKM matrix elements and the $D^+ \to \bar{K}^0 K^+$ branching fraction. Predictions based on $\mathrm{SU}(3)_F$ symmetry are only accurate to about 30 % and within these limits this prediction agrees with our result.

To obtain another rough estimate, we may also compare $D^+ \to K^+\pi^0$ with its corresponding neutral decay $D^0 \to K^+\pi^-$. Assuming no $D^0 - \bar{D}^0$ mixing, ignoring differences between these two decays due to the different spectator quark and also ignoring contributions from the second decay diagram in the D^+ decay, we expect $\Gamma_{D^+ \to K^+\pi^0} = \Gamma_{D^0 \to K^+\pi^-}$; therefore, applying

$$BF(i) = \Gamma(i)\tau. \tag{10.6}$$

with τ being the lifetime, we obtain the following relation:

$$BF(D^+ \to K^+\pi^0) = BF(D^0 \to K^+\pi^-)\frac{\tau_{D^+}}{\tau_{D^0}} \tag{10.7}$$

which gives an estimated value of $(3.5 \pm 0.28) \times 10^{-4}$. The errors listed are based only on the errors for the lifetimes and the $D^0 \to K^+\pi^-$ branching fraction, uncertainties due to the assumptions I had to make are not included.

APPENDIX A

Glossary of Terms

amplitude: A term which corresponds to probability of a particle or system being an a particular state. E.g. the square of a "decay amplitude" gives the probability that a particle will *decay* into the particular state.

baryon: A bound state of three quarks. A bound state of three anti-quarks is an anti-baryon.

hadron: Any particle interacting by the strong force. Usually, when we talk about hadrons, we talk about bound states of quarks, in particular mesons and baryons.

meson: A bound state of a quark and an anti-quark.

spin: An inherent quantum meachanical property of a particle, which corresponds to an intrinsic value of angular momentum.

APPENDIX B

CORBA

CORBA - *Common Object Request Broker Architecture* - is a object oriented *communication layer* defined by the Object Management Group (OMG) [17]. Multiple commercial and open-source implementations are available, avoiding vendor lock-in. The newer CORBA 2.0 standard even provides the means for interoperability between different implementations.

CORBA provides the means to send requests and data in a hardware/platform independent way. The communication endpoints are *objects* implemented in any of the supported OOPL (Object Oriented Programming Language), like for instance C++ and Java (both used for CLEO3 DAQ). CORBA interfaces are defined in the Interface Definition Language (IDL), which is standardized by the ISO. The IDL interface definition is then precompiled into C++ or Java. IDL is a strongly-typed language which together with the type-checking of modern C++ compiler allows us to locate many problems at *compile-time* instead of *run-time*. Like with object-oriented languages in general, there is a high degree of encapsulation in interfaces, meaning that the server can hide the implementation of the interface. A C++ analogue would be to say that the IDL is to the interface implementation as the header is to the C++ class implementation. The header only defines the methods provided by the class, the actual implementation of these methods is invisible and can thus be completely changed without having any effect on any users of this class. The IDL works in a similar way, it only defines what data and requests an interface provides. The actual implementation is hidden to the client connecting to the interface.

The data communication itself is handled in a client-server model where the clients dynamically find the servers at run time via an Object Request Broker (ORB). The server registers it's interfaces with the ORB by name and the clients locate these interfaces also by name at run-time. This makes setting up such a system very easy, and debugging much simpler. This system of dynamically configuring the system also allows testing to start with a very small scale setup and more components can be added gradually.

APPENDIX C

BaBar SP Production cycles

Following is a list of the three latest SP cycles followed by a more detailed description of the procedures used for SP8, the current SP cycle.

Strictly speaking, SP5 and SP6 are not really separate cycles since the old data corresponding to the SP5 cycle was not reprocessed. We consider them as separate cycles because the data storage format changed between SP5 and SP6 and old data and MC was converted, but not reprocessed, to the new format. It's easier to treat them as separate cycles since the MC production procedures are so different between them.

C.1 SP5 cycle

This SP cycle was started together with the data taking cycle that began in December of 2002. That data taking cycle continued until June of 2003. SP5 MC was produced for all months for which data was collected between February of 2000 (the first BaBar data ever collected) and June of 2003.

Up until this point, the events collected at BaBar during data taking were written to an Objectivity database. The SP5 MC events also were written to an Objectivity database. Between the end of this data taking cycle and the beginning of the next one, the storage format was changed from using Objectivity as the eventstore to using ROOT [22] files.

The reconstruction code didn't undergo any changes that would have made it necessary to reprocess the old data or redo all the MC. Instead a procedure was developed to convert all the data and SP5 MC to the new ROOT storage format.

C.2 SP6 cycle

This SP cycle was started together with the data taking cycle that began in September of 2003. That data taking cycle continued until July of 2004. SP6 MC was only produced for the months in this data taking cycle.

Data analyses used (and still use) a combination of the converted SP5 MC and the directly produced SP6 MC. Since most new data analyses will need at least some new signal MC, this means that production of SP6 and SP5 signal MC is continuing to this day and will continue as long as there are data analyses that use the data sample processed with the equivalent version of the reconstruction code.

C.3 SP8 cycle

If you are surprised about the missing SP7, there was an SP7 planned, but it was canceled. By the time it was canceled, the name for the SP8 cycle was already assigned.

This SP cycle is being started right now (as of June 2005). The new data taking cycle has already been started in April of 2005. SP8 MC events will be produced for all months for which we have BaBar data, that means we have to produce MC events for all the months that we already have data for and we also have to keep up with data taking. It will take quite a while to accumulate enough reprocessed data and SP8 MC events before data analyses can switch from using the old SP5 and SP6 MC events and the equivalent data to the new SP8 MC events and the reprocessed data.

C.4 SP8 production procedure

The MC production procedure works as follows. We have a certain pool of events we have to produce. These can either be generic MC events or user requests signal MC events, for the production this doesn't make any difference. If a SP site is idle, some number of events will be taken from the pool and assigned to the site for production. We call this assignment an allocation. The number of events in an allocation can vary, it depends mostly on the resources available at the site. We try to give a site enough events to keep them busy for one to two weeks. Usual sizes are in the few Million events range.

The allocations are split further into runs of 1000 or 2000 events. 1000 event runs are only used for signal MC allocations. Since we have to produce a mix of MC events over all months and the number of events needed for signal MC is usually pretty small. Having the ability to produce multiples of 1000 events instead of 2000 events for any given month makes it easier to get the mix just right. A run will always contain only one type of event to simulate, but an allocation can contain multiple types.

At the sites each of these runs is submitted as an individual job to local batch system and when it is finished, we have a collection of 1000 or 2000 events in a set of ROOT files.

All MC has to be returned to SLAC eventually to be put into a common framework and to make it accessible for analysis. But we don't transfer these output collections from the run jobs back to SLAC. They are small and it would be inefficient to manage the MC events on this level. What is exported instead are merge collections, which, as the name already suggests, consists of a number of run collections merged together. Only run collections for the same type of MC event can be merged together into a merge collection. For instance, if a site gets an allocation with runs for the simulation of $e^+e^- \to \tau^+\tau^-$ runs for the simulation of the $e^+e^- \to \mu^+\mu^-$, then there will only be merge collections containing one type of runs or the other, no merge collection that contains both types of runs. These merge collections are then exported to SLAC and can be used directly by an analysis.

BIBLIOGRAPHY

[1] J. J. Aubert *et al.* [E598 Collaboration], Phys. Rev. Lett. **33**, 1404 (1974).

[2] S. W. Herb *et al.*, Phys. Rev. Lett. **39**, 252 (1977).

[3] F. Abe *et al.* [CDF Collaboration], Phys. Rev. Lett. **74**, 2626 (1995) [arXiv:hep-ex/9503002].

[4] Contemporary Physics Education Project, `http://www.cpepweb.org/`

[5] D. Griffiths, *Introduction to Elementary Particles* (John Wiley & Sons, Inc., New York, 1987).

[6] S. Eidelman *et al.* [Particle Data Group], Phys. Lett. B **592**, 1 (2004).

[7] LEPP public website, `http://www.lns.cornell.edu/public/`

[8] E. Rice *et al.*, Phys. Rev. Lett. **48**, 906 (1982).

[9] R. Giles *et al.* [CLEO Collaboration], Phys. Rev. D **29**, 1285 (1984).

[10] D. Besson *et al.* [CLEO Collaboration], Phys. Rev. Lett. **54**, 381 (1985).

[11] E. von Torne *et al.*, Nucl. Instrum. Meth. A **473**, 17 (2001).

[12] R. Sia and t. C. R. group, arXiv:physics/0503080.

[13] CLEO Collaboration, *CLEO III Data Acquisition System Technical Design Report*, CBX 95-104, (Internal Report).

[14] Fastbus Introduction, `http://www-esd.fnal.gov/esd/catalog/intro/introfb.htm`

[15] VMEbus FAQ, `http://www.vita.com/vmefaq/`

[16] C. Strohman, R. Wanke and K. Honscheid, *Talk given at Computing in High-energy Physics (CHEP 97), Berlin, Germany, 7-11 Apr 1997*

[17] Object Management Group, http://www.omg.org/

[18] Object Oriented Database Solutions, http://www.objectivity.com/

[19] J. F. Donoghue, E. Golowich and B. R. Holstein, Camb. Monogr. Part. Phys. Nucl. Phys. Cosmol. **2**, 1 (1992).

[20] A. F. Falk, Y. Grossman, Z. Ligeti and A. A. Petrov, Phys. Rev. D **65**, 054034 (2002) [arXiv:hep-ph/0110317].

[21] B. Aubert *et al.* [BABAR Collaboration], Nucl. Instrum. Meth. A **479**, 1 (2002) [arXiv:hep-ex/0105044].

[22] The ROOT system home page, http://root.cern.ch/

[23] Description of the LH selectors, http://www.slac.stanford.edu/BFROOT/www/Physics/Tools/Pid/Hadrons/Description_of_the_LH_selectors.html

[24] U. Langenegger, *Cut-based Electron Identification*, BAD #90, Version 5 (*BABAR* internal analysis document), 2001

[25] F. Fabozzi and L. Lista, *Muon Identification in the BaBar Experiment*, BAD #60, Version 1 (*BABAR* internal analysis document), 2000

[26] J. Stelzer, *Kalman based reconstruction of IFR tracks*, BAD #799, Version 1 (*BABAR* internal analysis document), 2004

[27] K. Arms *et al.* [CLEO Collaboration], Phys. Rev. D **69**, 071102 (2004) [arXiv:hep-ex/0309065].

[28] T. Allmendinger et al., *Tracking Efficiency Studies in Release 12 and 14*, BAD #867 Version 2 (*BABAR* internal analysis document), 2004

[29] S. Mclachlin, *PID control samples at BABAR*, BAD #1056, Version 1 (*BABAR* internal analysis document), 2004

[30] A. Palano and D. Williams, *Study of dsj radiative decays*, BAD #790, Version 5 (*BABAR* internal analysis document), 2004

[31] F. C. Porter and A. Samuel, *Measurement of branching fractions and mass spectra of* $B \rightarrow K$ *pi pi gamma*, BAD #1155, Version 8 (*BABAR* internal analysis document), 2005

[32] M. T. Allen et al.,*A Study of Pi-zero Efficiency*, BAD #870, Version 3 (*BABAR* internal analysis document), 2004

[33] W. D. Hulsbergen et al.,*Measurement of the branching ratio and the time-dependent CP asymmetries for B0→Ks pi0 decays on run 1-4 data*, BAD #904, Version 11 (*BABAR* internal analysis document), 2005

[34] D. Kirkby et al.,*Semileptonic B Sample for Lifetime and Mixing Analyses*, BAD #147, Version 6 (*BABAR* internal analysis document), 2002

[35] L. L. Chau and H. Y. Cheng, Phys. Rev. D **36**, 137 (1987).